Rendezvous and Docking of Two Lighter-than-air Cubic Blimps

Patrick Abouzakhm

Master of Engineering

Department of Mechanical Engineering

McGill University

Montreal,Quebec

2016-11-05

A thesis submitted to McGill University in partial fulfilment of the requirements of the degree of Master of Engineering

ACKNOWLEDGEMENTS

I would like to thank my supervisor Professor Sharf for her guidance and support, and everything she has done for me throughout my Master's thesis and my time in the Aerospace Mechatronics Lab. I am also thankful to my colleagues at the lab, notably Pierre-Yves Brèches and Thomas Fuehrer, who have been extremely helpful at many Tryphon residencies, along with Florent Lefebvre. I would also like to thank David St-Onge for his great support and sharing his expertise with the Tryphon project.

ABSTRACT

The Tryphon is a helium filled, large cubic blimp with mounted propellers and various sensing for fully controlled indoor flight. The Tryphon project is a collaboration between engineers and artists, with the purpose of both research and artistic performances. Previous research concentrated solely on one Tryphon, where an accurate model has been developed, and a reasonable level of state estimation and feedback control have been achieved. This research focuses on the development of guidance, navigation and control for the rendezvous and docking of two Tryphons. The rendezvous stage consists of bringing the chaser Tryphon to a specified distance from the target Tryphon, where the docking stage then begins and more accurate sensing and control are used to dock. The combination of a discrete proportional integral derivative (PID) controller with waypoint guidance, and vision-based absolute pose feedback are used for the rendezvous stage. The docking stage uses ARtag fiducial markers for position based visual servoing control with a glideslope guidance algorithm for soft docking. Both stages use a kinematics-based Kalman filter for state and output estimation, which has a modular design for use with the varying sensor suites normally found on Tryphon. Docking is achieved through contact of the protruder and receiver ends of the custom-design electromagnetic docking mechanism. Mid-fidelity and high-fidelity simulators have been developed in Simulink/SimMechanics and Gazebo, respectively, with simulations of the full rendezvous and docking process carried out in Gazebo using ROS and virtual sensors. Experiments are conducted

for regulation of the chaser Tryphon in front of the target, and for the docking of the chaser to a fixed target Tryphon.

RÉSUMÉ

Le Tryphon est un grand dirigeable cubique rempli d'hélium, sur lequel sont montés de nombreux capteurs et hélices permettant un vol intérieur complètement contrôlé. Le projet Tryphon est une collaboration entre des ingénieurs et des artistes qui a pour but la recherche autant que la performance artistique. Les recherches précédentes, portant sur un seul Tryphon, ont permis de développer un modèle précis et d'atteindre un niveau raisonnable d'estimation d'état et de contrôle rétroactif. Cette recherche porte sur le développement du système de guidage, de navigation et de contrôle servant au rendez-vous et à l'amarrage de deux Tryphons. L'étape du rendez-vous consiste à amener le Tryphon « poursuiveur » à une distance spécifique du Tryphon « cible ». L'étape de l'amarrage est ensuite amorcée, où un système de contrôle et des capteurs plus précis sont utilisés. Un contrôleur PID discret combinant un système de guidage à repères et une rétroaction de la position absolue basée sur la vision est utilisé pour l'étape du rendez-vous. Dans l'étape de l'amarrage, des marqueurs de références ARtag sont utilisés avec un système de contrôle d'asservissement visuel basé sur la position combiné avec un système de trajectoire de descente, ce qui permet un amarrage en douceur. Pour l'estimation d'état et de sortie, les deux étapes nécessitent un filtre Kalman basé sur la cinématique, qui a un design modulaire permettant l'utilisation de plusieurs combinaisons de capteurs normalement trouvées sur les Tryphons. L'amarrage est atteint lorsque deux parties du mécanisme d'amarrage électromagnétique fait sur mesure, le « protruder » et le « receveur » entrent en contact. Des simulateurs de fidélité moyenne et élevée

ont été développés respectivement avec les programmes Simulink/SimMechanics et Gazebo. La simulation complète du rendez-vous et de l'amarrage est effectuée dans le programme Gazebo en utilisant ROS et des capteurs virtuels. Des expériences portant sur la régulation du Tryphon « poursuiveur » sont conduites devant la cible alors que d'autres portants sur l'amarrage du « poursuiveur » sont effectués sur un Tryphon fixe.

TABLE OF CONTENTS

LIST OF TABLES

LIST OF FIGURES

LIST OF SYMBOLS

$\underset{\rightarrow}{\mathbf{r}}_C$	Position of center of mass of chaser Tryphon
$\underset{\rightarrow}{\mathbf{r}}_1$	Position of camera 1 of chaser Tryphon w.r.t corresponding ARtag markers
$\underset{\rightarrow}{\mathbf{r}}_2$	Position of camera 2 of chaser Tryphon w.r.t corresponding ARtag markers
$\boldsymbol{\varphi}$	Orientation of the chaser Tryphon relative to inertial frame (Z-Y-X Tait-Bryan)
$\underset{\rightarrow}{\mathbf{v}}_C$	Linear velocity of the chaser Tryphon
$\boldsymbol{\omega}$	Angular velocity of the chaser Tryphon in body-fixed frame
$\underset{\rightarrow}{\mathbf{e}}_i$	Unit vector corresponding to axis i
$\underset{\rightarrow}{\mathbf{p}}_{ci}$	Camera positions from center of mass of chaser, i=1,2
$\underset{\rightarrow}{\mathbf{p}}_{ti}$	ARtag marker positions from center of mass of target, i=1,2
$\underset{\rightarrow}{\mathbf{p}}_{BC}$	Position of center of mass of chaser from its centroid
$(\ )^B$	Resolved in body-fixed frame
$(\ )^\times$	Cross product matrix
$(\ )^\dagger$	Moore-Penrose pseudoinverse
$m, \mathbf{J}$	Mass and inertia matrix of Tryphon
$\mathbf{A}_m, \mathbf{A}_J$	Added mass and added inertia of Tryphon
L	Side length of Tryphon
$\mathbf{F}_D, \mathbf{M}_D$	Drag force and moment of Tryphon, resolved in inertial frame and body-fixed frame respectively

$\mathbf{F}_C, \mathbf{M}_C$	Control force and moment, resolved in body-fixed frame
$\mathbf{F}_B, \mathbf{F}_G$	Buoyancy and gravity force, resolved in inertial frame
F_X, F_Y, M	Forces applied in X and Y inertial frame, and moment applied in θ for planar case
C	Center of mass of Tryphon
B	Center of buoyancy (Centroid) of Tryphon
O	Origin of inertial reference frame
$\mathbf{R}$	Rotation matrix between the body-fixed frame and inertial frame
$\mathbf{S}$	Matrix linking $\vec{\boldsymbol{\omega}}$ and $\dot{\vec{\boldsymbol{\varphi}}}$
$\mathbf{P}$	Controllability matrix
$\mathbf{Q}$	Observability matrix
$\mathbf{I}_{x\times y}, \mathbf{0}_{x\times y}$	Identity and zero matrices of size x by y
$\mathbf{x}, \mathbf{x}_\delta$	State vector of Tryphon for planar and 3-D case
$\mathbf{u}, \mathbf{u}_\delta$	Input vector for planar and 3-D case
$\mathbf{y}$	Output feedback vector
$\mathbf{z}$	Measurement vector
$\mathbf{A}, \mathbf{A}_0$	State matrix, for planar and 3-D case
$\mathbf{B}, \mathbf{B}_0$	Input matrix, for planar and 3-D case
$\mathbf{C}, \mathbf{C}_0$	Measurement matrix, for planar and 3-D case
$\hat{\mathbf{C}}, \hat{\mathbf{C}}_0$	State estimation matrix, for planar and 3-D case
$\mathbf{K}$	Controller gain matrix
k	Size of inputs
p	Size of outputs

n	Size of state matrix
ρ_{air}	Density of air
C_d	Drag coefficient
A	Projected area of Tryphon
T_{max}, T_{min}	$\pm$ Saturation thrusts of motors
F_{ji}	Individual motors mapping, j=x,y,z and i=1,2,3,4
α	Fractional difference between buoyancy force and gravity force
ζ	Difference in heights of chaser and target, Z_c-Z_t
K_P, K_D, K_p, K_d	PID gains, for 1 DOF analysis and discrete controller
$\hat{\mathbf{x}}, \hat{\mathbf{y}}$	Estimate of state and output feedback vectors
$\mathbf{w}_k^i, \mathbf{v}_k^i$	Process and measurement noise
$\mathbf{Q}^i, \mathbf{R}^i$	Process and measurement covariance matrices
$\mathbf{F}^i, \mathbf{H}^i$	Process and observation matrix
$\mathbf{P}^i$	Error covariance matrix
$\rho(t)$	Distance-to-go of glideslope
$\dot{\rho}(t)$	Approach velocity of glideslope
a	Glideslope parameter
$\vec{\boldsymbol{\rho}}_0$	Initial position of glideslope
$\dot{\rho}_T$	Commanded arrival velocity of glideslope
T	Manoeuvre period of glideslope
$\hat{\mathbf{u}}^B$	Direction cosines unit vector
ξ	Integral action term

CHAPTER 1
Introduction

1.1 Cubic Flying Robot: Tryphon

Autonomous blimps are very effective aerial vehicles when used for low-speed flight applications because of the payload and extended flight times they provide. The indoor cubic airships presented in this thesis, seen in figure 1–1 and referred to as Tryphons, are intended to be a research platform with development spread across teams at McGill University, UQAM and University of Laval, and to serve as an artistic project to captivate audiences during performances around the world.

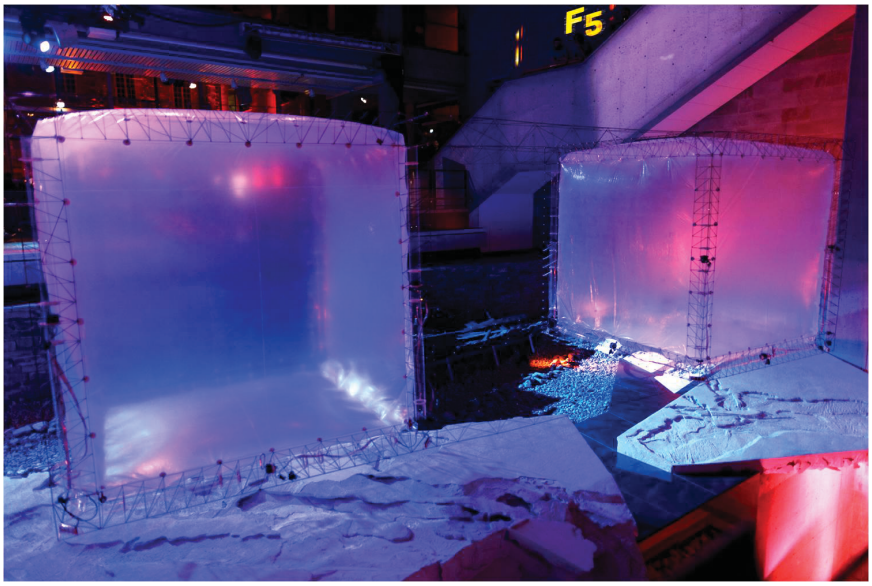

Figure 1–1: Tryphons on display at Musée de Civilisation, Quebec 2016

In order to transport the Tryphon internationally and have performances in various environments and conditions, several constraints have been imposed on its design and development. The structure of the Tryphon must be easily assembled and disassembled, and its size is limited by the restrictions of cargo on planes, effecting the maximum volume and thus payload the airship can have. Furthermore, the navigation and sensing methods applied to Tryphon must be robust to the various conditions found in the performance environments, and are normally preferred to be on-board solutions to maintain the sense of autonomy of the platform.

1.1.1 Background and Motivation

The Tryphon project was initially developed with the vision of constructing floating structures in space using the basic building block, the brick; it has undergone several iterations and modifications throughout the years [4][5], the most recent of which is presented in this research. To produce artistic performances using these large robotic blimps requires the collaboration between engineering and arts, and the project therefore also addresses a number of engineering research topics, such as human-robot interaction [6][7], state estimation for unmanned aerial vehicles (UAVs) [8], aerobot behaviour development, and assembly of multiple blimps, which is the focus of this thesis: assembling multiple Tryphons through autonomous rendezvous and docking with the goal of constructing floating structures. In this work, the entire assembly manoeuvre is defined by two stages: the rendezvous stage, where both the chaser and target Tryphons approach to a closer position and align with each other from any starting point, and the docking stage, where the Tryphons then close the

distance between each other completely and dock through contact of the docking mechanisms.

The autonomous, independent control of a single Tryphon has been achieved in [1], using a vision based global localization system. This ground-breaking accomplishment with regards to the Tryphon project provides the capability of trajectory tracking and waypoint guidance at any position in a room, introducing many different possibilities during artistic performances. The accurate control of a single Tryphon was indeed a major stepping stone towards the rendezvous and docking of two Tryphons, and has laid the groundwork for the work presented here.

1.1.2 Structure and General Hardware

Tryphon consists of a cubic bladder with side length of 2.15 m which is inflated with helium gas providing approximately 9.6 kg of lift, and an external structure made of twelve 2.25 m trusses composed of carbon fiber rods and 3D printed parts, as seen in figure 1–2.

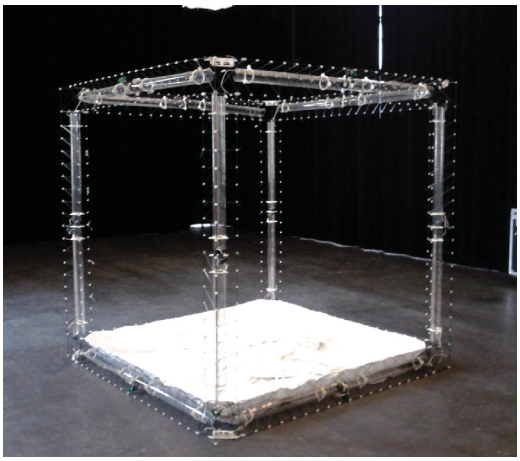

Figure 1–2: Tryphon structure: carbon fiber rods and 3D printed plastic parts [2]

The structure is designed to be lightweight and strong, in order to maintain the cubic shape of the blimp and support all additional equipment such as the embedded micro-computer, sensors, actuators, batteries, and docking mechanism. The mounted electronics used on Tryphons must be energy efficient and lightweight to lengthen flight times and fit within the payload of the blimp. Each Tryphon blimp has an on-board Gumstix Overo Firestorm, which is a Linux-based microprocessor. The boards communicate with a ground station laptop over a 5GHz network, and use Robot Operating System (ROS) and C++ software, allowing computationally intensive algorithms to be executed off-board. The Overo is connected to a Robovero expansion board, which includes an IMU and adds USB ports, allowing the use of the USB cameras and 5Ghz Wi-Fi dongle. Tryphons are actuated using eight MEGA ACn 16/7/5 electromotors driving ducted fans. These propellers are located at the center of each of the four lower horizontal trusses, and four vertical trusses as seen in figure 1–3.

1.1.3 Docking Mechanism and Hardware

Additional equipment, i.e., sensors and the docking mechanism, are needed on the target and chaser Tryphon for rendezvous and docking. The complete docking mechanism consists of four components: two receiver ends and two protruder ends. The components are custom designed using carbon fiber rods and 3D printed plastic parts to keep the mechanism as lightweight as possible while maintaining the overall aesthetics of Tryphons. The protruder end holds the electromagnet and the receiver end holds a cone-shaped plastic part with a metallic plate at the center, both of which protrude outward from the truss by approximately 3 cm. The cone-shape

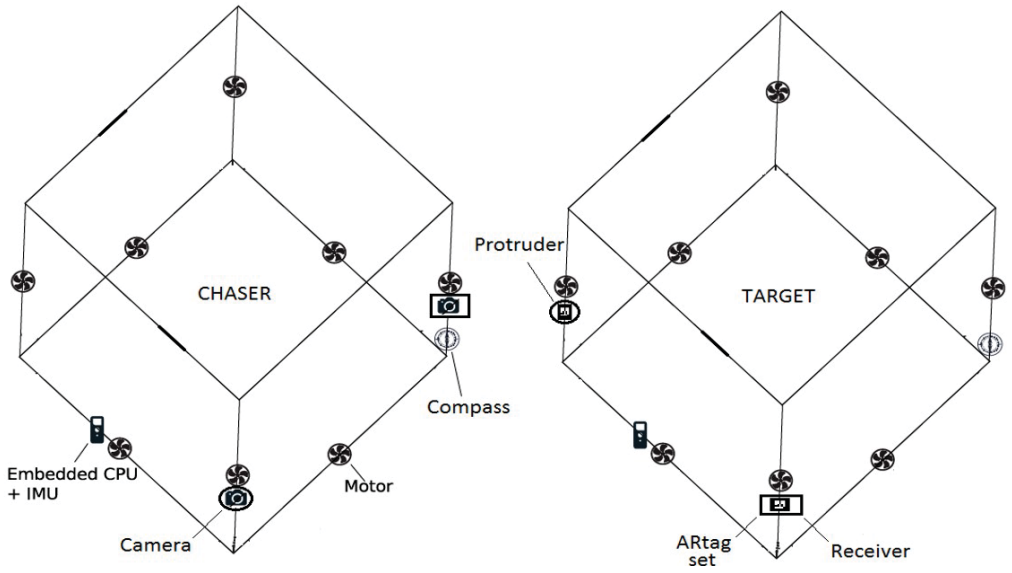

Figure 1–3: Equipment location on chaser and target Tryphon

helps guide the electromagnets of the protruder ends towards the metallic plates located on the receiver ends, and has an outer diameter of 8.5 cm. This dimension ultimately determines the accuracy requirement on the docking controller. Each Tryphon has one receiver and one protruder mounted on the same face of the cube (docking face), near the center of the bordering vertical trusses, visible in figure 1–3.

For rendezvous and docking of Tryphons, two different vision based navigation systems are used and will be explained in detail in Chapter 5. The hardware added for these systems includes one Firefly MV USB camera with a fish-eye lens located on both chaser and target Tryphon, placed on one of the top trusses with a slightly downward angle, as shown in figure 1–4. The chaser Tryphon is also equipped with two mounted Firefly cameras located within the structure of each of the docking mechanisms, attached to the Tryphon trusses. The target Tryphon has counterpart ARtag markers sets located near each of its docking mechanism components. When

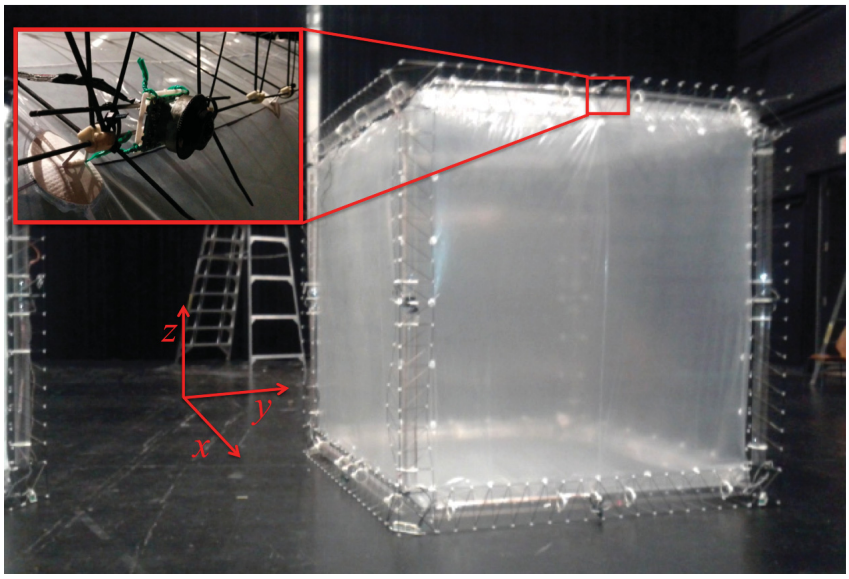

Figure 1–4: Camera placed on top truss of Tryphon [1]

docked, the camera and ARtag marker nearest the docking interface align perfectly. The receiver end located on the target Tryphon with its ARtag marker, and the protruder end of the chaser Tryphon with the mounted camera are shown in figure 1–5. More details of the camera/ARtag navigation system will be given in section 5.3.2.

1.2 Review of Related Work

The main focus of this thesis is the autonomous rendezvous and docking of two lighter-than-air cubic vehicles, the Tryphons. Previous work on Tryphon has been expanded upon and implemented for the rendezvous manoeuvre, and the guidance, navigation and control (GNC) systems have been developed and implemented for the docking task. The rendezvous stage uses a multi-camera parallel tracking and

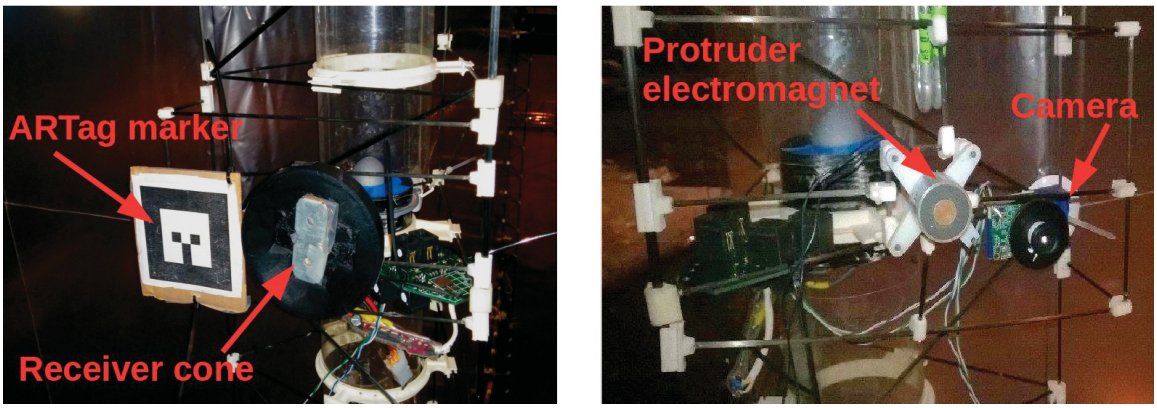

Figure 1–5: Docking mechanism with: receiver end with ARtag marker mounted on target Tryphon and protruder end with camera mounted on chaser Tryphon

mapping navigation system (MCPTAM) [7] with a discrete PID controller and way-point guidance; the docking of Tryphon is accomplished with an output feedback controller, glideslope guidance and an ARtag marker vision-based navigation, which will all be discussed in later chapters. This section reviews work and research relevant to the contributions in the presented topics.

1.2.1 Rendezvous and Docking

Docking of two or more vehicles is a difficult task which requires precision and robustness in the docking mechanism and GNC strategies used. The docking task commonly arises in space satellite missions, autonomous underwater vehicle (AUV) missions, and unmanned surface and aerial vehicle missions.

The neutral buoyancy of the Tryphon resembles the effects of zero gravity on objects in space, and although the physics of the two phenomena are not the same, there are similarities. Lighter-than-air vehicles have been used to simulate the effects of a zero-gravity environment in past research [9], and therefore a closely related field

to the rendezvous and docking of Tryphons would be that for spacecraft missions. In spacecraft missions, the strategies for docking vary immensely, and are dependant on many different assumptions and factors. The specific strategies involved in docking to a cooperative target are different and less challenging than to a non-cooperative one; however, reliable GNC systems are required for successful docking manoeuvres in either case. In [10], the authors treat the separate cases where the target spacecraft is fully cooperative and where it has attitude control only. Navigation relies on both relative state estimates and global state estimates obtained through an Extended Kalman filter, and a glideslope guidance algorithm is used for trajectory generation which provides the ability to choose an arrival velocity to ensure soft docking. The SPHERES testbed [11] used to evaluate the glideslope guidance algorithm was developed at MIT for testing autonomous docking algorithms in both 1-g and microgravity environments. The testbed has been used to perform successful 2-D docking experiments with the developed algorithms. A higher order sliding mode controller is presented in [12], which uses a camera and light based relative navigation system for docking. The navigation system is capable of estimating the relative attitude and position of the chaser, and the controller reduces the relative position error to zero while maintaining a safe arrival velocity. The authors of [13] design an adaptive output feedback control law for rendezvous and docking, where the effects of bounded output errors are analysed, and robustness to measurement uncertainty is ensured.

In terms of dynamics, another analogue platform type to lighter-than-air vehicles are underwater vehicles, as both contain the added mass terms in their equations

of motion. Rendezvous and docking of AUVs to submarines and docking platforms provides the opportunity for autonomous vehicle recovery, the transfer of new mission objectives, battery recharging, and data exchange [14]. Vision-based navigation systems using lights or markers are very effective means to obtain a relative pose underwater; however, they have limitations on the range at which they function. In [15], a visual servoing control approach is introduced for docking to a stationary target, providing simulation results. In [16] and [17], docking experiments to a fixed dock are conducted in the ocean engineering basin using the system with no current disturbances and assuming successful rendezvous. The authors suggest switching from the rendezvous navigation and control method to a docking visual servoing controller once the AUV is close enough to its target. A lighting arrangement is mounted on the docking cone receiver, which is used by the camera on the AUV to provide accurate pose measurements. The authors of [18] present a vision-based navigation system using self-similar three-pattern landmarks for pose and range estimation during the rendezvous stage. The system is capable of target localization, which is then fused with movement measurements coming from the AUV's navigation sensors (accelerometer, compass and depth meter) using a particle filter. Visibility of the landmark proved to be the greatest restriction during experiments, although some enhancements have assisted in improving the performance.

Underwater vehicles are subject to large disturbances caused by waves and currents, which can be difficult for a control system to manage, if not designed to be robust. In [19], a Takagi-Sugeno-Kang fuzzy inference control system is used for the rendezvous and docking of an AUV and is designed to compensate for current

disturbances. The assumption of a fixed dock cone with pre-known orientation and altitude is made, and an error-state Kalman filter is used to fuse ultra-short baseline measurements and inertial sensor measurements. Another application of rendezvous and docking of an AUV is presented in [20], but in this work the role is reversed, and an unmanned surface vehicle is controlled to dock to a target AUV that is floating at the water's surface, using a vision-based navigation system. The vision system uses a processed, segmented image of the target AUV and uses a potential field vehicle control strategy to dock.

The Tryphon itself is categorized as an unmanned aerial vehicle (UAV), and some work has been done in the area of rendezvous and docking of UAVs, in the context of refueling and recharging. In [21], a fixed-wing aircraft is used, where full-state feedback is obtained with a vision-based navigation system, and docking to a tanker with a probe and drogue mechanism using a LQR controller is simulated. In [22] a complete solution to the airborne docking of two fixed-wing aircraft is presented, where a vision-aided unscented Kalman filter is used for relative navigation, resulting in successful experimental demonstrations using a probe and drogue mechanism. In the lighter-than-air vehicle domain, station-keeping and docking of a non-holonomic blimp using image-based visual servoing control has been studied in [23], where the blimp used a PID controller and square marker.

Normally, as observed in all of the previously reviewed literature, the mechanics of the docking process is solved using a mechanism which has only one physical contact point. In the case of Tryphon docking, there are two physical contact points necessary for a successful dock, and these have mechanisms (protruder and receiver as

described earlier) that allow only up to ±4.25 cm of error in the transverse directions. To add to the challenge, these contact points are located approximately 2.25 m apart; therefore, an accurate and effective GNC system is required for Tryphon docking to ensure not one, but both contact points meet simultaneously to ensure a successful dock.

1.2.2 ARtags

As seen in the previous literature, vision-based navigation systems using markers and light patterns are an effective way to approach the docking navigation problem, although each system has its own advantages and disadvantages. Fidicuary marker navigation systems such as ARtag provide accurate relative position measurements which is ideal for the chaser/target scenario, as well as reduced sensitivity to partial occlusions and lighting variations [24]. ARtag uses a robust digital encoding method for the identification/verification stage and quadrilateral outlines with an edge-based approach for the unique features of the detection process [24]. Several markers can be combined together, with each one easily identifiable using their unique bit coded ID, thus opening up a range of possibilties. A sample of ARTag markers is presented in figure 1–6. Fiducial marker systems have been used as the navigation solution

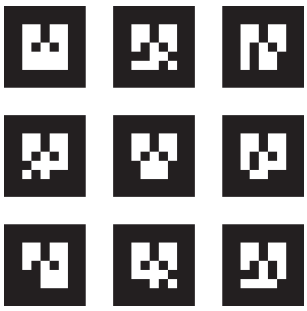

Figure 1–6: ARtag markers [3]

for several different applications, including docking. In [25], the docking of the axel rover to the central module of the DuAxel rover is studied, where a fiducial marker system was used for successful experiments. In [26], an ARtag system is applied to accurately determine the relative pose for vision-based spacecraft docking. In [27], ARtag markers are used as landmarks for simultaneous localization and mapping for the navigation system of an indoor blimp. An ARtag system was chosen for Tryphon docking due to the advantages stated above, considering occlusion and lighting variations are concerns in the indoor environments that Tryphons are flown in, and that a high level of accuracy is required.

1.3 Thesis Organization and Objectives

The goal of this research is the rendezvous and docking of a chaser and target Tryphon using two electromagnetic protruder/receiver docking mechanisms, with the purpose of being used to construct floating structures and to appear in artistic performances. First and foremost, this thesis begins by presenting the formulation of the dynamics model for the chaser/target system assuming a fixed target in Chapter 2, for both a simplified planar case and the complete 6 DOF case. The kinematics involving the docking system are derived, and the equations of motion are presented, based on the previous model of [28]. The system is then linearized for both the ideal case and the case when there is a small center of mass offset in the chaser Tryphon. Afterwards, Chapter 3 presents the two simulation models developed for the rendezvous and docking scenario: one in Simulink/SimMechanics and the other in Gazebo environments. The focus of Chapter 4 is on the regulation of Tryphons, where an output feedback control law which uses relative navigation, or more specifically,

a position-based visual servoing controller utilizing an ARtag fiducial marker system is introduced. Here, a set of regulation experiments is presented, which leads to an investigation into the effects of a center of mass offset on the performance and stability of Tryphon under output feedback control. Next, experimental results for the regulation of Tryphon under closed-loop control are presented to validate the assumption of a fixed/stationary target, followed by a look into the performance of the chaser/target system under different levels of cooperation. In Chapter 5, the results of the level of cooperation analysis are used to determine the docking strategy, and the guidance, navigation and control system for the rendezvous stage and the docking stage are presented. This is then followed by simulation results of the entire manoeuvre. Experimental results are presented in Chapter 6 for successful docking experiments to a fixed target. Finally, conclusions can be found in Chapter 7 with details and recommendations of future work.

CHAPTER 2
Dynamics Modelling and Linearization of Tryphon System

In order to first analyse the docking control problem for two cubic blimps, the case where a fixed, non-moving target is considered. In practice, this is approximately achieved by having the target regulate at a constant desired pose under closed-loop control. It is important to note that for the remainder of this thesis, *fixed* target will refer to the Tryphon being completely immobile, and *stationary* target will refer to the Tryphon regulating at a desired pose. It is assumed that the two are approximately equivalent, therefore the dynamics and control of the chaser can be represented independently of the target. The decision to have a stationary target follows the results presented in section 4.5, where different levels of cooperation between the chaser and target are investigated. By closing the loop with the two camera-ARtag pairs briefly presented in section 1.1.3, the docking control becomes a position-based visual-servo control problem where the goal is to bring the relative poses of the camera/ARtag pairs to zero. First, the dynamics and state-space model of the planar case of the docking problem will be derived and investigated. This is followed by the derivation of the dynamics for the full 6 DOF model of the chaser, where both the ideal state-space model and the model with a center of mass offset are presented.

2.1 Planar Case

In this section the docking problem is simplified to two dimensions by treating the chaser and target cubes as rigid bars, as shown in figure 2–1. The purpose is to determine the feasibility of using an output feedback controller with the 3 DOF system using only two relative position measurements $\underrightarrow{\mathbf{r}}_1$ and $\underrightarrow{\mathbf{r}}_2$, before extending it to the full 6 DOF model of the chaser. Control of orientation and position of the chaser using the two position errors only is explored. Here, the target bar is fixed, with its body-fixed frame aligned with the inertial frame, and hence they are the same frames having the same O-XY origin. The chaser is free to move in the X-Y plane with 3 degrees of freedom; X, Y, and θ. The chaser's body-fixed frame C-xy origin is located at the center of the bar.

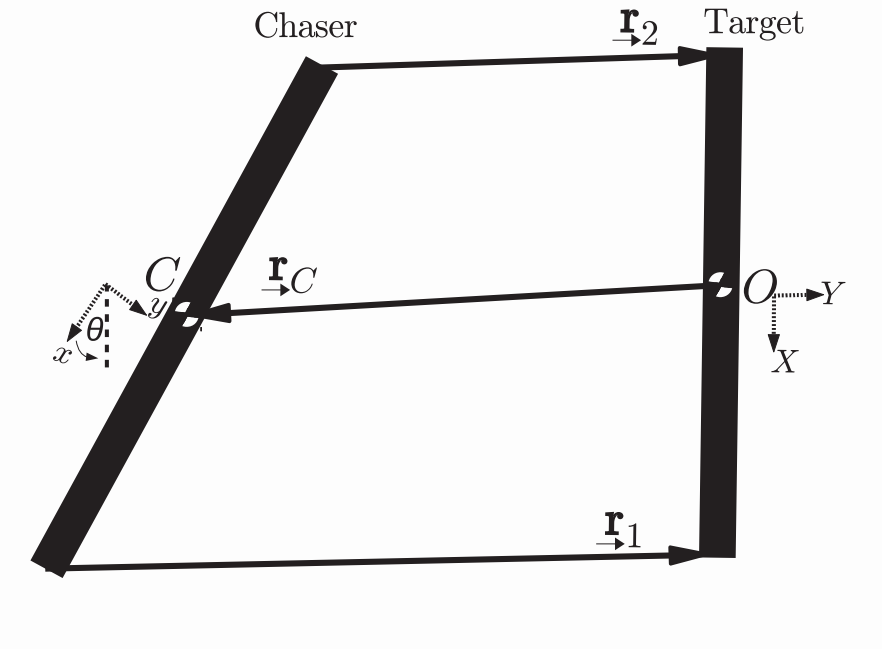

Figure 2–1: 2-D simplification of chaser and target Tryphons as rigid bars

2.1.1 Kinematics

The output given by the camera-ARtag pairs corresponding to vectors $\underrightarrow{\mathbf{r}}_1$ and $\underrightarrow{\mathbf{r}}_2$ must be formulated in order to model and control the system. By vector addition, $\underrightarrow{\mathbf{r}}_1$ and $\underrightarrow{\mathbf{r}}_2$ are defined by the equations:

$$\begin{aligned} \underrightarrow{\mathbf{r}}_1 &= -\underrightarrow{\mathbf{r}}_C + \frac{L}{2}\underrightarrow{\mathbf{e}}_X - \frac{L}{2}\underrightarrow{\mathbf{e}}_x \\ \underrightarrow{\mathbf{r}}_2 &= -\underrightarrow{\mathbf{r}}_C - \frac{L}{2}\underrightarrow{\mathbf{e}}_X + \frac{L}{2}\underrightarrow{\mathbf{e}}_x \end{aligned} \tag{2.1}$$

where, L is the length of both the chaser and target bars, $\underrightarrow{\mathbf{e}}_X$ and $\underrightarrow{\mathbf{e}}_x$ are each one of three basis vectors composing the chaser and target reference frames shown in figure 2–1, respectively, and $\mathbf{r}_i = [X_i, Y_i]^T$ for $i = 1, 2$ when resolved in the inertial frame. Resolving all of equation (2.1) in the inertial frame gives:

$$\begin{aligned} X_1 &= -X + \frac{L}{2} - \frac{L\cos\theta}{2} \\ Y_1 &= -Y + \frac{L\sin\theta}{2} \\ X_2 &= -X - \frac{L}{2} + \frac{L\cos\theta}{2} \\ Y_2 &= -Y - \frac{L\sin\theta}{2} \end{aligned} \tag{2.2}$$

Furthermore, equations (2.2) can be differentiated with respect to time to give the time derivatives of $\mathbf{r}_1$ and $\mathbf{r}_2$ in the inertial frame.

2.1.2 Equations of Motion

Consider the simplified dynamics of the chaser rigid bar expressed in the inertial frame:

$$
\begin{aligned}
m\ddot{X} &= F_X \\
m\ddot{Y} &= F_Y \\
J\ddot{\theta} &= M
\end{aligned}
\tag{2.3}
$$

with m and J equivalent to the mass of a Tryphon and the moment of inertia about the center of mass of the bar, and control forces/moments are taken about the center of mass.

2.1.3 State-space Model

The model, which has been used because of its simplicity and linearity, is now formulated and expressed in state-space form in order to check controllability, observability, and assignability when using only the information obtained from the camera-ARtag pairs to control each of the three degrees of freedom. It is clear that the simplified rigid bar dynamics are already linear, and can be directly written in state-space form:

$$
\dot{\mathbf{x}} = \mathbf{A}\mathbf{x} + \mathbf{B}\mathbf{u} \tag{2.4}
$$

with the state vector $\mathbf{x} = [X, Y, \theta, \dot{X}, \dot{Y}, \dot{\theta}]^T$, input vector $\mathbf{u} = [F_X, F_Y, M]^T$, and $\mathbf{A}$ and $\mathbf{B}$:

$$
\mathbf{A} = \begin{bmatrix} \mathbf{0}_{3\times3} & \mathbf{I}_{3\times3} \\ \mathbf{0}_{3\times3} & \mathbf{0}_{3\times3} \end{bmatrix}, \quad \mathbf{B} = \begin{bmatrix} \mathbf{0}_{3\times2} & \mathbf{0}_{3\times1} \\ \frac{1}{m}\mathbf{I}_{2\times2} & 0_{2\times1} \\ \mathbf{0}_{1\times2} & \frac{1}{J} \end{bmatrix} \tag{2.5}
$$

The measurement and output equations are obtained by defining the measurement vector $\mathbf{z} = [\mathbf{r}_1^T, \mathbf{r}_2^T]^T$ and output feedback vector $\mathbf{y} = [\mathbf{r}_1^T, \mathbf{r}_2^T, \dot{\mathbf{r}}_1^T, \dot{\mathbf{r}}_2^T]^T$, and linearizing the kinematics to give:

$$\begin{aligned} \mathbf{z} &= \mathbf{C}\mathbf{x} \\ \mathbf{y} &= \hat{\mathbf{C}}\mathbf{x} \end{aligned} \tag{2.6}$$

The $\mathbf{C}$ matrix is formed by using the linearized measurement equations relating $\mathbf{r}_1$ and $\mathbf{r}_2$ with $\mathbf{r}_C$ from equations (2.2). The $\hat{\mathbf{C}}$ matrix is formed by augmenting $\mathbf{C}$ with the linearized velocity terms and is referred to as the state estimation matrix. Linearization about $\theta = 0$ results in the following definitions:

$$\mathbf{C} = \begin{bmatrix} \mathbf{C}_1 & \mathbf{0}_{4\times 3} \end{bmatrix} \tag{2.7}$$

and

$$\hat{\mathbf{C}} = \begin{bmatrix} \mathbf{C}_1 & \mathbf{0}_{4\times 3} \\ \mathbf{0}_{4\times 3} & \mathbf{C}_1 \end{bmatrix} \tag{2.8}$$

where

$$\mathbf{C}_1 = \begin{bmatrix} -1 & 0 & 0 \\ 0 & -1 & L/2 \\ -1 & 0 & 0 \\ 0 & -1 & -L/2 \end{bmatrix} \tag{2.9}$$

completing the state space model of the planar system.

Before moving on to the full system, the feasibility of controlling two positions must be determined. To do so, the controllability and observability of the planar case is investigated. Let us call the matrices $\mathbf{P}$ and $\mathbf{Q}$ the controllability and observability

matrices, respectively, which are given as:

$$\mathbf{P} = \begin{bmatrix} \mathbf{B} & \mathbf{AB} & \mathbf{A}^2\mathbf{B} & \dots & \mathbf{A}^5\mathbf{B} \end{bmatrix}, \quad \mathbf{Q} = \begin{bmatrix} \mathbf{C} & \mathbf{CA} & \mathbf{CA}^2 & \dots & \mathbf{CA}^5 \end{bmatrix}^T \tag{2.10}$$

since the state vector is in $\mathbb{R}^6$. To prove controllability and observability, it is sufficient to show that matrices $\mathbf{P}$ and $\mathbf{Q}$ have rank 6. Using the $\mathbf{A}$,$\mathbf{B}$ and $\mathbf{C}$ matrices derived above, the system's controllability and observability matrices are:

$$\mathbf{P} = \begin{bmatrix} \mathbf{0}_{3\times3} & \mathbf{P'} & \mathbf{0}_{3\times12} \\ \mathbf{P'} & \mathbf{0}_{3\times3} & \mathbf{0}_{3\times12} \end{bmatrix}, \quad \mathbf{Q} = \begin{bmatrix} \mathbf{C}_1 & \mathbf{0}_{4\times3} \\ \mathbf{0}_{4\times3} & \mathbf{C}_1 \\ \mathbf{0}_{16\times3} & \mathbf{0}_{16\times3} \end{bmatrix} \tag{2.11}$$

where

$$\mathbf{P'} = \begin{bmatrix} \frac{1}{m}\mathbf{I}_{2x2} & 0 \\ \mathbf{0}_{1x2} & \frac{1}{J} \end{bmatrix} \tag{2.12}$$

which clearly both have rank 6, thus proving controllability and observability of the system. Consequently, this shows the derived state-space model represents a minimal realization. According to [29], a sufficient condition for generic pole assignability of a minimal realization through static output feedback control is:

$$k + p \geq n + 1 \tag{2.13}$$

where k (columns in $\mathbf{B}$) and p (rows in $\hat{\mathbf{C}}$) represent the size of the inputs and outputs respectively, and n is the size of the state matrix $\mathbf{A}$. In the planar system,

this condition is satisfied thus proving the feasibility of output feedback control using two position measurements. This process can now be extended to the full system.

2.2 6 DOF case

The three dimensional, 6 DOF model of the system is now considered. The system consists of two cubes, a chaser and a target, with the target once again fixed and having the inertial frame origin located at its center of mass as seen in figure 2–2. The body-fixed frame origin of the chaser is located at its center of mass. As in the planar case, $\underrightarrow{\mathbf{r}}_1$ and $\underrightarrow{\mathbf{r}}_2$ represent the position vectors between the camera/ARtag pairs, $\underrightarrow{\mathbf{r}}_C$ represents the position of the center of mass of the chaser (relative to O). In addition, $\underrightarrow{\mathbf{p}}_{c1}$ and $\underrightarrow{\mathbf{p}}_{c2}$ represent the position vectors of the cameras on the chaser with respect to its center of mass, $\underrightarrow{\mathbf{p}}_{t1}$ and $\underrightarrow{\mathbf{p}}_{t2}$ are the position vectors of the ARtags on the target with respect to the inertial origin and $(\mathbf{p}_{BC}^{B})^{\times}$ is the cross product matrix associated with the position vector $\underrightarrow{\mathbf{p}}_{BC}$, pointing from the centroid to the center of mass of the chaser Tryphon, resolved in the body-fixed frame as denoted by the superscript B. Vector components in the inertial frame are left without a superscript.

2.2.1 Kinematics

The orientation of the chaser relative to the target is given by Tait-Bryan angles (Z-Y-X Euler angles) with ψ, θ, and ϕ as yaw, pitch and roll respectively. Next, the rotation matrix $\mathbf{R}$ presented in [30], is defined which takes vector components from the inertial frame into the chaser body-fixed frame as:

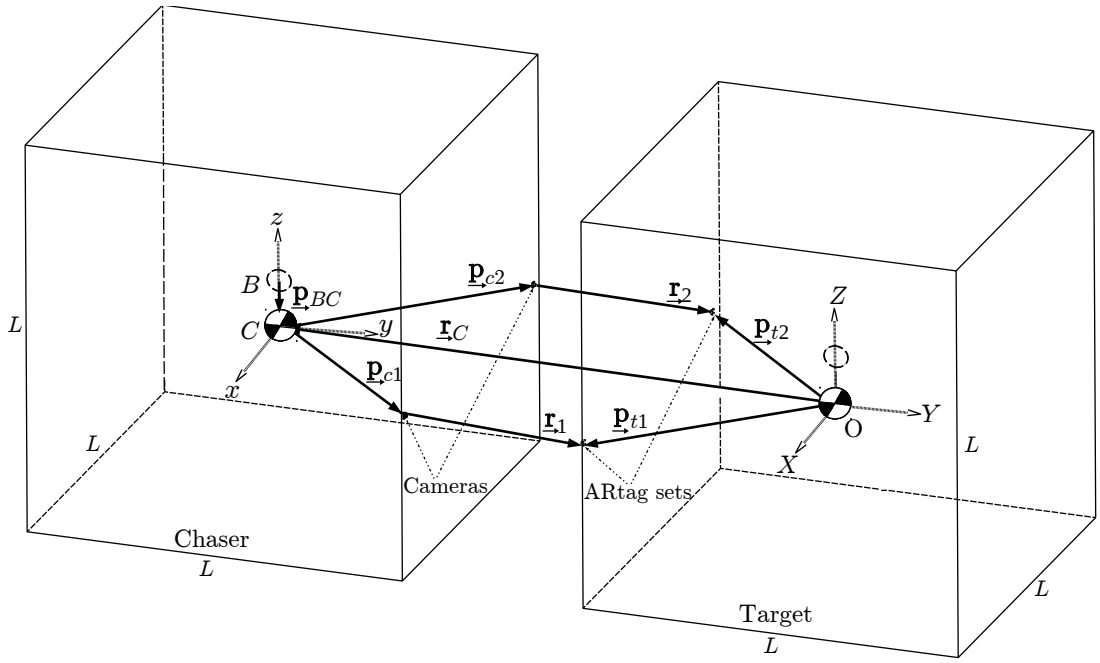

Figure 2–2: Chaser and target cube system

$$\mathbf{R} = \begin{bmatrix} \cos\psi\cos\theta & \cos\theta\sin\psi & -\sin\theta \\ \cos\psi\sin\theta\sin\phi - \cos\phi\sin\psi & \cos\psi\cos\phi + \sin\psi\sin\theta\sin\phi & \cos\theta\sin\phi \\ \sin\psi\sin\phi + \cos\psi\cos\phi\sin\theta & \cos\phi\sin\psi\sin\theta - \cos\psi\sin\phi & \cos\theta\cos\phi \end{bmatrix} \tag{2.14}$$

Defining $\boldsymbol{\omega} = [p, q, r]^T$ as the body-fixed frame angular velocity components of the chaser Tryphon and $\dot{\boldsymbol{\varphi}} = [\dot{\phi}, \dot{\theta}, \dot{\psi}]^T$ as the Euler rates, the relation $\boldsymbol{\omega} = \mathbf{S}\dot{\boldsymbol{\varphi}}$ from [30] exists where:

$$\mathbf{S} = \begin{bmatrix} 1 & 0 & -\sin\theta \\ 0 & \cos\phi & \cos\theta\sin\phi \\ 0 & -\sin\phi & \cos\theta\cos\phi \end{bmatrix} \tag{2.15}$$

leading to the inverse relationship:

$$\begin{aligned} \dot{\phi} &= p + q\sin\phi\tan\theta + r\cos\phi\tan\theta \\ \dot{\theta} &= q\cos\phi - r\sin\phi \\ \dot{\psi} &= q\sin\phi\sec\theta + r\cos\phi\sec\theta \end{aligned} \tag{2.16}$$

Once again, the output given by the camera-ARtag pairs corresponding to position vectors $\underrightarrow{\mathbf{r}}_1$ and $\underrightarrow{\mathbf{r}}_2$ must be formulated in order to model and control the system. With the geometry in figure 2–2 and using vector addition, $\underrightarrow{\mathbf{r}}_1$ and $\underrightarrow{\mathbf{r}}_2$ are defined by the equations:

$$\begin{aligned} \underrightarrow{\mathbf{r}}_1 &= -\underrightarrow{\mathbf{r}}_C - \underrightarrow{\mathbf{p}}_{c1} + \underrightarrow{\mathbf{p}}_{t1} \\ \underrightarrow{\mathbf{r}}_2 &= -\underrightarrow{\mathbf{r}}_C - \underrightarrow{\mathbf{p}}_{c2} + \underrightarrow{\mathbf{p}}_{t2} \end{aligned} \tag{2.17}$$

The measurements given by the camera-ARtag pairs are obtained in the body-fixed frame of the chaser cube; therefore, $\underrightarrow{\mathbf{r}}_1$ and $\underrightarrow{\mathbf{r}}_2$ must be expressed in the body-fixed frame. Here, $\underrightarrow{\mathbf{r}}_C$ is also expressed in the body-fixed frame and the vector components of $\underrightarrow{\mathbf{p}}_{c1}$ and $\underrightarrow{\mathbf{p}}_{c2}$ are constant in the body-fixed frame, leaving position vectors $\underrightarrow{\mathbf{p}}_{t1}$ and $\underrightarrow{\mathbf{p}}_{t2}$ which have constant vector components in the inertial frame, and therefore must be transformed into the body-fixed frame giving equation (2.18):

$$\begin{aligned} \mathbf{r}_1^B &= -\mathbf{r}_C^B - \mathbf{p}_{c1}^B + \mathbf{R}\mathbf{p}_{t1} \\ \mathbf{r}_2^B &= -\mathbf{r}_C^B - \mathbf{p}_{c2}^B + \mathbf{R}\mathbf{p}_{t2} \end{aligned} \tag{2.18}$$

Here, $\mathbf{r}_C^B = [x, y, z]^T$, $\mathbf{p}_{t1} = [\frac{L}{2}, -\frac{L}{2}, 0]^T$, $\mathbf{p}_{t2} = [-\frac{L}{2}, -\frac{L}{2}, 0]^T$, $\mathbf{p}_{c1}^B = [\frac{L}{2}, \frac{L}{2}, 0]^T$, and $\mathbf{p}_{c2}^B = [-\frac{L}{2}, \frac{L}{2}, 0]^T$ resulting in:

$$\mathbf{r}_1^B = \begin{bmatrix} -x - \frac{L}{2} + \frac{L}{2}\cos\psi\cos\theta - \frac{L}{2}\cos\theta\sin\psi \\ -y - \frac{L}{2} + \frac{L}{2}(\cos\psi\sin\theta\sin\phi - \cos\phi\sin\psi) - \frac{L}{2}(\cos\psi\cos\phi + \sin\psi\sin\theta\sin\phi) \\ -z + \frac{L}{2}(\sin\psi\sin\phi + \cos\psi\cos\phi\sin\theta) - \frac{L}{2}(\cos\phi\sin\psi\sin\theta - \cos\psi\sin\phi) \end{bmatrix} \tag{2.19}$$

and

$$\mathbf{r}_2^B = \begin{bmatrix} -x + \frac{L}{2} - \frac{L}{2}\cos\psi\cos\theta - \frac{L}{2}\cos\theta\sin\psi \\ -y - \frac{L}{2} - \frac{L}{2}(\cos\psi\sin\theta\sin\phi - \cos\phi\sin\psi) - \frac{L}{2}(\cos\psi\cos\phi + \sin\psi\sin\theta\sin\phi) \\ -z - \frac{L}{2}(\sin\psi\sin\phi + \cos\psi\cos\phi\sin\theta) - \frac{L}{2}(\cos\phi\sin\psi\sin\theta - \cos\psi\sin\phi) \end{bmatrix} \tag{2.20}$$

Furthermore, $\mathbf{r}_1^B$ and $\mathbf{r}_2^B$ can be differentiated with respect to time to give the relative velocities $\dot{\mathbf{r}}_1^B$ and $\dot{\mathbf{r}}_2^B$:

$$\begin{aligned} \dot{\mathbf{r}}_1^B &= -\mathbf{v}_C^B + \boldsymbol{\omega}^\times \mathbf{r}_C^B + \dot{\mathbf{R}}\mathbf{p}_{t1} \\ \dot{\mathbf{r}}_2^B &= -\mathbf{v}_C^B + \boldsymbol{\omega}^\times \mathbf{r}_C^B + \dot{\mathbf{R}}\mathbf{p}_{t2} \end{aligned} \tag{2.21}$$

where the relationship $\mathbf{v}_C^B = \dot{\mathbf{r}}_C^B + \boldsymbol{\omega}^\times \mathbf{r}_C^B$ has been used, with $\mathbf{v}_C^B = [u, v, w]$ as the body-fixed components of velocity of the center of mass of the chaser Tryphon. Equation (2.16) is then used to substitute the Euler rate terms that appear in $\dot{\mathbf{R}}$

with the angular velocities p, q, and r. These equations will be used to model the output feedback of the system as described in section 2.2.3.

2.2.2 Equations of Motion

The presented dynamics model of Tryphon is based on the model derived in [28], where both translational and rotational equations of motion are expressed in the body-fixed frame, but with the rotational equations taken about the center of mass, rather than the center of buoyancy:

$$\begin{aligned}(m\mathbf{I}_{3\times3} + \mathbf{A}_m)(\dot{\mathbf{v}}_C^B + \boldsymbol{\omega}^\times \mathbf{v}_C^B) &= \mathbf{R}\mathbf{F}_D + \alpha\mathbf{R}\mathbf{F}_G + \mathbf{F}_C \\ (\mathbf{J} + \mathbf{A}_J)\dot{\boldsymbol{\omega}} &= -\boldsymbol{\omega}^\times(\mathbf{J} + \mathbf{A}_J)\boldsymbol{\omega} + \mathbf{M}_D + (\mathbf{p}_{BC}^B)^\times \mathbf{R}\mathbf{F}_D + (\mathbf{p}_{BC}^B)^\times \mathbf{R}\mathbf{F}_B + \mathbf{M}_C\end{aligned} \tag{2.22}$$

In the above, m, $\mathbf{J}$, $\mathbf{A}_m$ and $\mathbf{A}_J$ represent the mass, centroidal matrix of inertia, added mass and added inertia respectively. The added mass and added inertia terms are given by:

$$\mathbf{A}_m = A_m \mathbf{I}_{3\times3} \tag{2.23}$$

$$\mathbf{A}_J{}^1 \ = A_J \mathbf{I}_{3\times3} + A_m(\mathbf{p}_{BC}^B)^\times(\mathbf{p}_{BC}^B)^\times \tag{2.24}$$

which have been studied for Tryphon in detail in [1]. As in [1], certain terms due to expressing the added inertia properties at the center of mass of the Tryphon instead of the centroid have been neglected to simplify the modeling. Moreover, $\boldsymbol{\omega}^\times(\mathbf{J} + \mathbf{A}_J)\boldsymbol{\omega}$ and $\boldsymbol{\omega}^\times \mathbf{v}_C^B$ are the nonlinear inertial effects from expressing the dynamics in the

[1] The added inertia was originally presented incorrectly with a sign error in [1]

body-fixed frame. The drag force $\mathbf{F}_D$ and drag moment $\mathbf{M}_D$ [1] are given by:

$$\mathbf{F}_D = -\frac{1}{2}\rho_{air} C_d A |\mathbf{v}_C| \mathbf{v}_C \tag{2.25}$$

$$\mathbf{M}_D = -\frac{1}{32}\rho_{air} C_d L^5 |\boldsymbol{\omega}| \boldsymbol{\omega} \tag{2.26}$$

where C_d is the drag coefficient, ρ_{air} is the density of air and A is the projected area of Tryphon normal to $\mathbf{v}_C$. Furthermore, $\mathbf{F}_C$ and $\mathbf{M}_C$ are the control forces and torques, which are mapped to the individual motors (with saturation T_{max} and T_{min}) of the Tryphon using the force distribution algorithm developed in [1] corresponding to the propeller placement shown in figure 2–3. Finally, α is the fractional difference

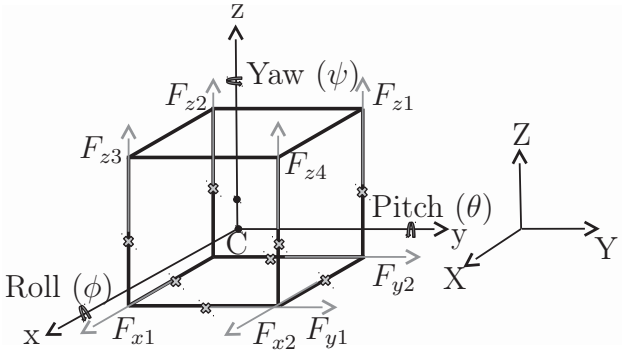

Figure 2–3: Tryphon propeller nominal thrust directions F_i.

between the buoyancy force $\mathbf{F}_B$ and gravity force $\mathbf{F}_G$, i.e.:

$$\mathbf{F}_B = (\alpha - 1)\mathbf{F}_G \text{ and } \mathbf{F}_G = m \begin{bmatrix} 0 \\ 0 \\ -9.81 \end{bmatrix} \tag{2.27}$$

with $\alpha = 0$ implying neutral buoyancy. The control forces and moments and the drag moment are expressed in the body-fixed frame, while $\mathbf{F}_D$, $\mathbf{F}_G$ and $\mathbf{F}_B$ are expressed

in the inertial frame. It is also noted that the superscript B notation to denote the body-fixed frame components is only used for the translational motion variables since rotational equations of motion are traditionally written in the body-fixed frame. In the ideal model, the center of mass is located directly under the center of buoyancy (centroid), i.e., $\mathbf{p}_{BC}^{B} = [0, 0, l_z]^T \mid (l_z < 0)$, although minor variations are expected in the real system. Table 2–1 shows the nominal values of the parameters of the Tryphon system.

Table 2–1: Tryphon system parameters

m (kg)	L (m)	l_z (m)	T_{max} (N)	T_{min} (N)	C_d
11.7	2.25	-0.17	0.63	-0.32	1.74

$\mathbf{J}$ ($\text{kg} \cdot \text{m}^2$)	$\mathbf{A}_m$ (kg)	$\mathbf{A}_J$ ($\text{kg} \cdot \text{m}^2$)
$J_{xx} = 15.2$	$A_{mx} = 11.3$	$A_{Jx} = 0.2$
$J_{yy} = 15.3$	$A_{my} = 11.3$	$A_{Jy} = 0.2$
$J_{zz} = 16$	$A_{mz} = 11.3$	$A_{Jz} = 0.2$

2.2.3 Ideal State-Space Model

The state-space model is now formulated and linearized in order to design a linear output feedback controller using the pole placement technique. As was done in the planar 3 DOF model, the measured variables include the measurements obtained from the camera-ARtag pairs, but in addition, orientation sensing of the chaser and target are included. This was motivated by the fact that in the 6 DOF case, not all angles can be controlled with the two position measurements only. The output feedback consists of the estimated values from the state estimator. It is noted that the linear model derived here assumes zero lateral offset between the center of mass

and center of buoyancy. In first order form, the equations of motion are written as:

$$\dot{\mathbf{x}} = \mathbf{f}(\mathbf{x}, \mathbf{u}) \tag{2.28}$$

where the state is defined as $\mathbf{x} = [(\mathbf{r}_C^B)^T, \boldsymbol{\varphi}^T, (\mathbf{v}_C^B)^T, \boldsymbol{\omega}^T]^T$ and the input vector $\mathbf{u} = [\mathbf{F}_C^T, \mathbf{M}_C^T]^T$, with $\mathbf{f}(\mathbf{x}, \mathbf{u})$ as:

$$\mathbf{f}(\mathbf{x}, \mathbf{u}) = \begin{bmatrix} \mathbf{v}_C^B - \boldsymbol{\omega}^{\times}\mathbf{r}_C^B \\ \mathbf{S}^{-1}\boldsymbol{\omega} \\ \frac{1}{m+A_m}(\mathbf{R}\mathbf{F}_D + \alpha\mathbf{R}\mathbf{F}_G + \mathbf{F}_C) - \boldsymbol{\omega}^{\times}\mathbf{v}_C^B \\ (\mathbf{J} + \mathbf{A}_J)^{-1}(-\boldsymbol{\omega}^{\times}(\mathbf{J} + \mathbf{A}_J)\boldsymbol{\omega} + (\mathbf{p}_{BC}^B)^{\times}\mathbf{R}\mathbf{F}_D + \mathbf{M}_D + (\mathbf{p}_{BC}^B)^{\times}\mathbf{R}\mathbf{F}_B + \mathbf{M}_C) \end{bmatrix} \tag{2.29}$$

The subset $\mathbf{S}_d$ (equation (2.30)) of the kernel of $\mathbf{f}$, i.e., satisfying $\mathbf{f}(\mathbf{x}_0, \mathbf{u}_0) = 0$, is chosen as the operating point for the linearization using Taylor series expansion and it represents the chaser cube in its docked position with the target:

$$\mathbf{S}_d = \mathbf{S}_x \times \mathbf{S}_u \text{ where } \begin{cases} \mathbf{S}_x = \{[0, -L, \mathbf{0}_{1\times 10}]^T\} \\ \mathbf{S}_u = \{[0, 0, -\alpha mg, 0, 0, 0]^T\} \end{cases} \tag{2.30}$$

The rendezvous stage reduces the error and relative orientation of the chaser from the target, thus bringing the system near this operating point for the switch to the docking stage. In order to make the linear model independent of $\mathbf{u}_0$, α is taken as 0 meaning a neutrally buoyant cube. The first order terms of the Taylor series expansion about the operating point $(\mathbf{x}_0, \mathbf{u}_0)$ are:

$$\mathbf{f}(\mathbf{x},\mathbf{u}) \approx \mathbf{f}(\mathbf{x}_0,\mathbf{u}_0) + \left.\frac{\partial \mathbf{f}}{\partial \mathbf{x}}\right|_{\mathbf{x}_0,\mathbf{u}_0} (\mathbf{x}-\mathbf{x}_0) + \left.\frac{\partial \mathbf{f}}{\partial \mathbf{u}}\right|_{\mathbf{x}_0,\mathbf{u}_0} (\mathbf{u}-\mathbf{u}_0) \tag{2.31}$$

or more specifically, by replacing the Jacobian matrices $\left.\frac{\partial \mathbf{f}}{\partial \mathbf{x}}\right|_{\mathbf{x}_0,\mathbf{u}_0}$ and $\left.\frac{\partial \mathbf{f}}{\partial \mathbf{u}}\right|_{\mathbf{x}_0,\mathbf{u}_0}$ with the equivalent state matrices $\mathbf{A}_0$ and $\mathbf{B}_0$ respectively, the following linear state-space equations are obtained:

$$\begin{aligned} \dot{\mathbf{x}}_\delta &= \mathbf{A}_0\mathbf{x}_\delta + \mathbf{B}_0\mathbf{u}_\delta \\ \mathbf{z} &= \mathbf{C}_0\mathbf{x}_\delta \\ \mathbf{y} &= \hat{\mathbf{C}}_0\mathbf{x}_\delta \end{aligned} \tag{2.32}$$

with

$$\mathbf{A}_0 = \begin{bmatrix} \mathbf{0}_{3\times3} & \mathbf{0}_{3\times3} & \mathbf{I}_{3\times3} & \mathbf{A}_L \\ \mathbf{0}_{3\times3} & \mathbf{0}_{3\times3} & \mathbf{0}_{3\times3} & \mathbf{I}_{3\times3} \\ \mathbf{0}_{3\times3} & \mathbf{0}_{3\times3} & \mathbf{0}_{3\times3} & \mathbf{0}_{3\times3} \\ \mathbf{0}_{3\times3} & \mathbf{A}_\varphi & \mathbf{0}_{3\times3} & \mathbf{0}_{3\times3} \end{bmatrix} \tag{2.33}$$

$$\mathbf{A}_L = \begin{bmatrix} 0 & 0 & -L \\ 0 & 0 & 0 \\ L & 0 & 0 \end{bmatrix}, \quad \mathbf{A}_\varphi = \begin{bmatrix} \frac{-mgl_z}{J_{xx}+A_J+A_m l_z^2} & 0 & 0 \\ 0 & \frac{-mgl_z}{J_{yy}+A_J+A_m l_z^2} & 0 \\ 0 & 0 & 0 \end{bmatrix} \tag{2.34}$$

and

$$\mathbf{B}_0 = \begin{bmatrix} \mathbf{0}_{3\times3} & \mathbf{0}_{3\times3} \\ \mathbf{0}_{3\times3} & \mathbf{0}_{3\times3} \\ \frac{1}{m+A_m}\mathbf{I}_{3\times3} & \mathbf{0}_{3\times3} \\ \mathbf{0}_{3\times3} & (\mathbf{J}+\mathbf{A}_J)^{-1} \end{bmatrix} \tag{2.35}$$

Here, $\mathbf{x}_\delta = \mathbf{x} - \mathbf{x}_0$, $\mathbf{u}_\delta = \mathbf{u} - \mathbf{u}_0$, $\mathbf{z} = [(\mathbf{r}_1^B)^T, (\mathbf{r}_2^B)^T, \boldsymbol{\varphi}^T, \boldsymbol{\omega}^T]^T$ is the measurement vector, and $\mathbf{y} = [(\mathbf{r}_1^B)^T, (\mathbf{r}_2^B)^T, \boldsymbol{\varphi}^T, (\dot{\mathbf{r}}_1^B)^T, (\dot{\mathbf{r}}_2^B)^T, \boldsymbol{\omega}^T]^T$ represents the output feedback vector. Also, $\mathbf{r}_i^B = [x_i, y_i, z_i]^T$ and $\dot{\mathbf{r}}_i^B = [\dot{x}_i, \dot{y}_i, \dot{z}_i]^T$ for $i = 1, 2$, matrix $\mathbf{C}_0$ is the Jacobian matrix of the kinematic equations derived in section 2.2.1 representing the measurement matrix, and $\hat{\mathbf{C}}_0$ is a state estimation matrix to account for velocity estimation:

$$\mathbf{C}_0 = \begin{bmatrix} -\mathbf{I}_{3\times3} & \mathbf{C}_{A_{12}} & \mathbf{0}_{3\times3} & \mathbf{0}_{3\times3} \\ -\mathbf{I}_{3\times3} & \mathbf{C}_{A_{22}} & \mathbf{0}_{3\times3} & \mathbf{0}_{3\times3} \\ \mathbf{0}_{3\times3} & \mathbf{I}_{3\times3} & \mathbf{0}_{3\times3} & \mathbf{0}_{3\times3} \\ \mathbf{0}_{3\times3} & \mathbf{0}_{3\times3} & \mathbf{0}_{3\times3} & \mathbf{I}_{3\times3} \end{bmatrix} \tag{2.36}$$

$$\hat{\mathbf{C}}_0 = \begin{bmatrix} -\mathbf{I}_{3\times3} & \mathbf{C}_{A_{12}} & \mathbf{0}_{3\times3} & \mathbf{0}_{3\times3} \\ -\mathbf{I}_{3\times3} & \mathbf{C}_{A_{22}} & \mathbf{0}_{3\times3} & \mathbf{0}_{3\times3} \\ \mathbf{0}_{3\times3} & \mathbf{I}_{3\times3} & \mathbf{0}_{3\times3} & \mathbf{0}_{3\times3} \\ \mathbf{0}_{3\times3} & \mathbf{0}_{3\times3} & -\mathbf{I}_{3\times3} & \mathbf{C}_{B_{12}} \\ \mathbf{0}_{3\times3} & \mathbf{0}_{3\times3} & -\mathbf{I}_{3\times3} & \mathbf{C}_{B_{22}} \\ \mathbf{0}_{3\times3} & \mathbf{0}_{3\times3} & \mathbf{0}_{3\times3} & \mathbf{I}_{3\times3} \end{bmatrix} \tag{2.37}$$

where

$$\mathbf{C}_{A_{i2}} = \frac{1}{2}\begin{bmatrix} 0 & 0 & -L \\ 0 & 0 & (-1)^i L \\ L & (-1)^{i+1}L & 0 \end{bmatrix}, \ \mathbf{C}_{B_{i2}} = \frac{1}{2}\begin{bmatrix} 0 & 0 & L \\ 0 & 0 & (-1)^i L \\ -L & (-1)^{i+1}L & 0 \end{bmatrix}, \ i = 1, 2 \tag{2.38}$$

These equations represent the linear dynamics model for the chaser cube with a fixed target, near the docked position, with the modelled output feedback. It can be shown using the methodology of section 2.1.3, that the model is both controllable and observable. Furthermore, the assignability criteria of equation (2.1.3) is satisfied and therefore generic pole assignability is feasible using an output feedback controller with the pole placement technique, which will be presented in section 4.1.

2.2.4 Model Linearization with Center of Mass Offset

The center of mass of Tryphon is by design lower than the centroid of the cube in order for the buoyancy force to provide a passive stabilization in both roll and pitch. Ideally, the center of mass is directly underneath the center of the cube with no offset in the body-fixed x-y plane, but since equipment and masses are constantly being added and removed from Tryphon, there is uncertainty in its position. An offset in the center of mass in the x-y plane changes the equilibrium state of the cube, more precisely, the equilibrium roll and pitch. This section will focus on developing the linear model of Tryphon under the assumption of an offset in the y-axis only; the y-axis will define the direction of docking for further work. The presence of an offset in the x-axis makes docking not plausible, as contact of both docking mechanism points cannot occur at the equilibrium pitch this offset would induce. There is therefore

no need to treat the case of an offset in the x-axis for the purpose of docking of two Tryphons. This model will later be used in chapter 4 to analyse the effect of an offset on the performance of the system during regulation experiments when the controller used has not been designed with the offset taken into consideration. The relationship between a y-axis offset and the change in equilibrium roll ϕ_0 is found by equating the term $(\mathbf{p}_{BC}^{B})^{\times}\mathbf{R}\mathbf{F}_B$ from equation (2.29) to 0, leading to:

$$\begin{aligned} -l_z \cos\theta_0 \sin\phi_0 + l_y \cos\theta_0 \cos\phi_0 = 0 \\ \text{or } \phi_0 = \gamma = \arctan(\frac{l_y}{l_z}) \end{aligned} \tag{2.39}$$

with the new vector pointing from the centroid to center of mass of the cube as $\mathbf{p}_{BC}^{B} = [0, l_y, l_z]^T$.

Taking the equations of motion once again at the center of mass, the first order form of equation (2.29) is linearized about the new operating point $(\mathbf{x'}_0, \mathbf{u'}_0)$ given by the subset $\mathbf{S'}_d$:

$$\mathbf{S'}_d = \mathbf{S'}_x \times \mathbf{S'}_u \text{ where } \begin{cases} \mathbf{S'}_x = \{[0, -\frac{L}{2}(1+\cos\gamma), \frac{L}{2}\sin\gamma, \gamma, \mathbf{0}_{1\times 8}]^T\} \\ \mathbf{S'}_u = \{[0, 0, -\alpha mg, 0, 0, 0]^T\} \end{cases} \tag{2.40}$$

representing the docked position of the chaser cube with the new equilibrium roll angle. This results in a new matrix $\mathbf{A'}_0$:

$$\mathbf{A'}_0 = \begin{bmatrix} \mathbf{0}_{3\times 3} & \mathbf{0}_{3\times 3} & \mathbf{I}_{3\times 3} & \mathbf{A'}_L \\ \mathbf{0}_{3\times 3} & \mathbf{0}_{3\times 3} & \mathbf{0}_{3\times 3} & \mathbf{I}_{3\times 3} \\ \mathbf{0}_{3\times 3} & \mathbf{0}_{3\times 3} & \mathbf{0}_{3\times 3} & \mathbf{0}_{3\times 3} \\ \mathbf{0}_{3\times 3} & \mathbf{A'}_\varphi & \mathbf{0}_{3\times 3} & \mathbf{0}_{3\times 3} \end{bmatrix} \tag{2.41}$$

similar to $\mathbf{A}_0$ in equation (2.33), but having:

$$\mathbf{A'}_L = \begin{bmatrix} 0 & -\frac{L}{2}\sin\gamma & -\frac{L}{2}(1+\cos\gamma) \\ \frac{L}{2}\sin\gamma & 0 & 0 \\ \frac{L}{2}(1+\cos\gamma) & 0 & 0 \end{bmatrix} \tag{2.42}$$

$$\mathbf{A'}_\varphi = \begin{bmatrix} \frac{-mg(l_z\cos\gamma + l_y\sin\gamma)}{J'_{xx}+A_J+A_m(l_y^2+l_z^2)} & 0 & 0 \\ 0 & \frac{-mgl_z(A_J+J'_{zz})}{A_\varphi^{\text{den}}} & 0 \\ 0 & \frac{mgl_y(A_J+J'_{yy})}{A_\varphi^{\text{den}}} & 0 \end{bmatrix} \tag{2.43}$$

where

$$A_\varphi^{\text{den}} = A_J^2 + A_J J'_{yy} + A_J J'_{zz} + J'_{yy}J'_{zz} + A_J A_m l_y^2 + A_J A_m l_z^2 + A_m J'_{yy} l_y^2 + A_m J'_{zz} l_z^2 \tag{2.44}$$

The force distribution algorithm is designed assuming only a z-axis offset in the center of mass, therefore introducing a y-axis offset causes a new term to appear with the control wrench, since $\mathbf{F}_C$ and $\mathbf{M}_C$ are still assumed to act at the nominal center of mass position in the algorithm. Because of the symmetric nature and format of the force distribution, an additional moment $-2(\mathbf{p}_Y^B)^\times \mathbf{F}_C$ is present in the rotational equations of motion, with $\mathbf{p}_Y^B = [0, l_y, 0]^T$, and a corresponding new term appears in the input matrix $\mathbf{B}_0$, giving:

$$\mathbf{B'}_0 = \begin{bmatrix} \mathbf{0}_{3\times3} & \mathbf{0}_{3\times3} \\ \mathbf{0}_{3\times3} & \mathbf{0}_{3\times3} \\ \frac{\mathbf{I}_{3\times3}}{m+A_m} & \mathbf{0}_{3\times3} \\ (\mathbf{J}+\mathbf{A}_J)^{-1}\mathbf{B'}_A & (\mathbf{J}+\mathbf{A}_J)^{-1} \end{bmatrix}, \quad \mathbf{B'}_A = \begin{bmatrix} 0 & 0 & -2l_y \\ 0 & 0 & 0 \\ -2l_y & 0 & 0 \end{bmatrix} \tag{2.45}$$

Finally, the output feedback equations are linearized about $(\mathbf{x'}_0, \mathbf{u'}_0)$ giving:

$$\mathbf{C'}_0 = \begin{bmatrix} -\mathbf{I}_{3\times3} & \mathbf{C'}_{A_{12}} & \mathbf{0}_{3\times3} & \mathbf{0}_{3\times3} \\ -\mathbf{I}_{3\times3} & \mathbf{C'}_{A_{22}} & \mathbf{0}_{3\times3} & \mathbf{0}_{3\times3} \\ \mathbf{0}_{3\times3} & \mathbf{I}_{3\times3} & \mathbf{0}_{3\times3} & \mathbf{0}_{3\times3} \\ \mathbf{0}_{3\times3} & \mathbf{0}_{3\times3} & \mathbf{0}_{3\times3} & \mathbf{I}_{3\times3} \end{bmatrix} \tag{2.46}$$

$$\hat{\mathbf{C}}'_0 = \begin{bmatrix} -\mathbf{I}_{3\times3} & \mathbf{C'}_{A_{12}} & \mathbf{0}_{3\times3} & \mathbf{0}_{3\times3} \\ -\mathbf{I}_{3\times3} & \mathbf{C'}_{A_{22}} & \mathbf{0}_{3\times3} & \mathbf{0}_{3\times3} \\ \mathbf{0}_{3\times3} & \mathbf{I}_{3\times3} & \mathbf{0}_{3\times3} & \mathbf{0}_{3\times3} \\ \mathbf{0}_{3\times3} & \mathbf{0}_{3\times3} & -\mathbf{I}_{3\times3} & \mathbf{C'}_{B_{12}} \\ \mathbf{0}_{3\times3} & \mathbf{0}_{3\times3} & -\mathbf{I}_{3\times3} & \mathbf{C'}_{B_{22}} \\ \mathbf{0}_{3\times3} & \mathbf{0}_{3\times3} & \mathbf{0}_{3\times3} & \mathbf{I}_{3\times3} \end{bmatrix} \tag{2.47}$$

where

$$\mathbf{C'}_{A_{i2}} = \frac{L}{2} \begin{bmatrix} 0 & 0 & -1 \\ \sin\gamma & (-1)^{i+1}\sin\gamma & (-1)^i\cos\gamma \\ \cos\gamma & (-1)^{i+1}\cos\gamma & (-1)^{i+1}\sin\gamma \end{bmatrix}, \; i = 1, 2 \tag{2.48}$$

$$\mathbf{C'}_{B_{i2}} = \frac{L}{2} \begin{bmatrix} 0 & \sin\gamma & \cos\gamma \\ -\sin\gamma & 0 & (-1)^{i+1} \\ -\cos\gamma & (-1)^i & 0 \end{bmatrix}, \; i = 1, 2 \tag{2.49}$$

This represents the linear state-space model for the chaser cube when the center of mass is offset in the y-axis. While this model is not used to design a closed-loop

controller, its purpose is to investigate the reason for the poor performance of the regulation tests presented in section 4.2.

CHAPTER 3
Simulation Environments and Results

Since Tryphons are very large, experiments can only be carried out at what is referred to as research-creation residencies. These residencies involve renting a large enough space for at least two Tryphons to be put together and flown, for the purposes of both engineering research and artistic performances. This also requires a large supply of helium, and for these reasons, residencies are organized only a few times per year for one or two weeks at a time. As a solution to this challenging limitation, a high fidelity simulation of the blimps has been developed and implemented in a Gazebo environment [31] for residency preparation, and for testing of all developed algorithms. A mid-fidelity simulator has also been developed in Simulink/SimMechanics, which is less detailed and is used to first develop and validate algorithms. This chapter will present the two simulation models and environments in detail.

3.1 Perfect Feedback Simulink Model

Simulink was the first simulation environment chosen, because of its advantages with regards to the simplicity of implementation of algorithms, its organized and modular graphical user interface, its direct data observation and plotting capabilities, and its integration with SimMechanics for visual feedback of the simulation. For the initial development of guidance, estimation and control algorithms, this simulation serves as a quick and accurate means of validation. The dynamics model implemented in simulation is based on the non-linear system of equations of section 2.2.2 but

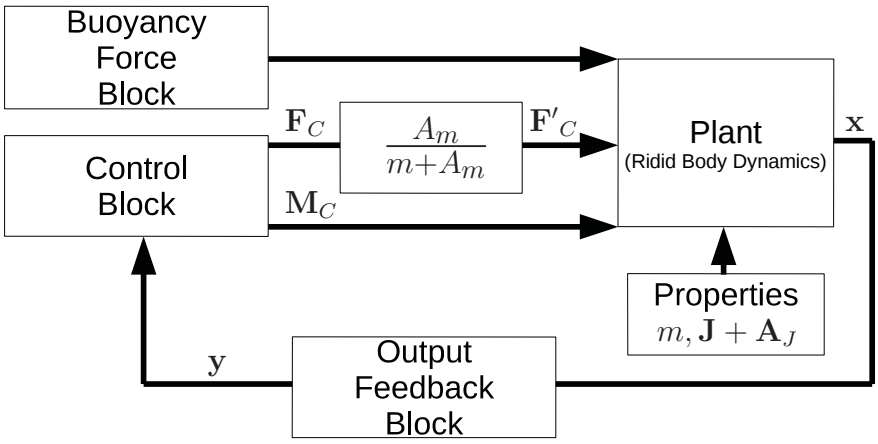

Figure 3–1: Block diagram giving overview of Simulink/SimMechanics model

neglecting the drag terms, and the target Tryphon is fixed with only the chaser being controlled. The controller implementation is under ideal conditions, that is: perfect measurements are available for output feedback, no actuator saturation is present, and control forces and moments are applied directly at the nominal center of mass of the Tryphon.

The dynamics model is implemented in SimMechanics and integrated with the Simulink component, where applied forces and state outputs are all expressed in the body-fixed frame of the chaser. There are no special inputs for added mass and inertia in the dynamics model of SimMechanics, nor a buoyancy force term; therefore, they must be implemented appropriately. Figure 3–1 represents an overview of the Simulink/SimMechanics model. The buoyancy force in the model is implemented through an external Simulink force block which applies the force at the centroid. The added inertia can be added directly into the inertia tensor of the dynamics model to correctly capture this effect as per equations (2.22). However, since the weight of the Tryphon is computed directly by SimMechanics from the specified mass of the body,

the added mass cannot be simply added to the mass input of the Tryphon because this would produce an incorrect weight for the blimp. This would then require an incorrect buoyancy force for neutral buoyancy. Therefore, the Tryphon is modelled in SimMechanics using the following equations of motion:

$$\begin{aligned} m\mathbf{I}_{3\times3}(\dot{\mathbf{v}}_C^B + \boldsymbol{\omega}^\times \mathbf{v}_C^B) &= \mathbf{R}\mathbf{F}_G + \mathbf{R}\mathbf{F}_B + \mathbf{F}'_C \\ (\mathbf{J} + \mathbf{A}_J)\dot{\boldsymbol{\omega}} &= -\boldsymbol{\omega}^\times(\mathbf{J} + \mathbf{A}_J)\boldsymbol{\omega} + (\mathbf{p}_{BC}^B)^\times \mathbf{R}\mathbf{F}_B + \mathbf{M}_C \end{aligned} \tag{3.1}$$

where the drag terms have been omitted, and the buoyancy force is exactly equal in magnitude to the weight and therefore they cancel each other out. To overcome the missing added mass terms, the applied translational control input $\mathbf{F'}_C$ is redefined as:

$$\mathbf{F'}_C = \frac{A_m}{(A_m + m)}\mathbf{F}_C \tag{3.2}$$

where $\mathbf{F}_C$ is the nominal translational control input, which is applied to the SimMechanics dynamics block. Equations (3.1) and (3.2) thus correctly include the added mass for a neutrally buoyant Tryphon. A Simulink block based on the kinematics found in section 2.2.1 is used to obtain the output feedback, which is used by the control and guidance blocks. The parameters appearing in this model match those given in Table 2–1. This simulation model has been used for the initial development of the output feedback controller and to perform the analysis conducted in Chapter 4, as well as to develop the glideslope guidance algorithm of section 5.3.1. While this model suffices for preliminary development, it is not an accurate enough representation of the real system to allow its sole use for algorithm tuning in lieu of directly with Tryphon.

3.2 High Fidelity Gazebo Model

The non-linear and more detailed system dynamics have been implemented in the high-fidelity Gazebo model using the parameters listed in Table 2–1. Gazebo is an open source software which uses the OGRE engine [32] and has several advantages including: its 3D rendering abilities, giving great visualization of the emulated Tryphon, its compatibility with ROS, which allows all algorithms used in simulation to be directly ported to the physical Tryphon, and the ability to add virtual sensors with noise profiles similar to those of their real counterparts, which will be discussed in more detail in section 3.2.1. The model of the chaser and target system presented in this section is an extension of the model developed in [1], where only a single Tryphon was modelled in the simulated environment. The Gazebo simulation environment with two Tryphons can be seen in figure 3–2, where the target Tryphon is not fixed, and is controlled to emulate a stationary target. In this simulation, all known aspects of the dynamics of Tryphon have been modelled. The drag, actuator saturation and noise profiles of each sensor are included unlike the previously described Simulink model. Furthermore the propellers are placed at their respective locations and the developed force distribution algorithm is used to map all control wrenches to the individual motor commands.

In order to execute the main algorithms in ROS for each Tryphon, each loaded Tryphon model is assigned an IP address. The developed algorithms communicate through ROS using topic names and messages, which use the IP addresses to ensure proper communication, identically to how it is done on the physical platforms. On occasion, code must differ for simulation compared to the real system because of

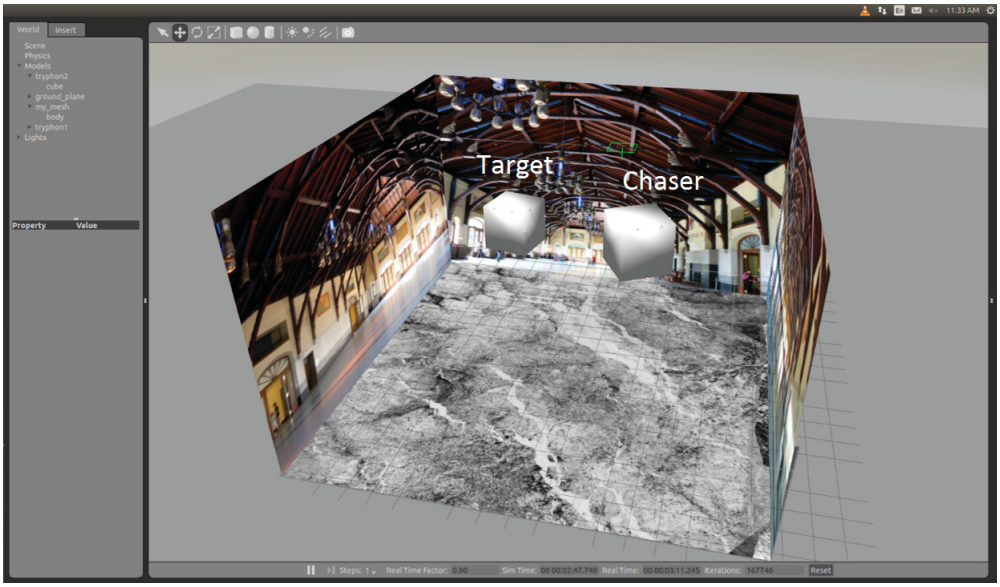

Figure 3–2: Gazebo simulation environment with two Tryphons

extra features that must be added for algorithms to work virtually, such as camera based algorithms. To maintain the portability of the algorithms, from simulation to the real system, the ROS architecture is organized to be modular by creating programs specifically designed as intermediate links to take care of these additional virtual requirements. This allows the code of the main algorithms used for Tryphon to remain unaltered, yet still work in both simulation and on the real system.

3.2.1 Environment and Virtual Sensors

The ability to render environments and implement virtual sensors is an attractive feature of Gazebo. In figure 3–2, the background image of the rendered environment comes from the Chalet Mont-Royal in Montreal, Canada: a space that was used in May 2014 for a Tryphon residency and where an artistic performance was held. By creating walls to simulate a room, and adding textures of an actual field trial location,

this not only adds depth and a sense of realism to the simulation, but also provides more fidelity in the implemented vision-based algorithms used for rendezvous (to be presented in section 5.2.1). Ideally, the environment rendering would consist of all of the 3D elements of the room and not only textures on the walls, but this would require a significant amount of computational power and would take away from the performance of the simulation. Nevertheless, the current set-up meets the needs of this research.

Since the environment in which the physical Tryphon is flown varies based on the type of performance, an array of sensors is available for use and the specific equipment for any given performance is contingent on the environmental conditions such as lightning, wall proximity, and presence of windows. The ability to emulate sensors in Gazebo provides a simulation environment which allows for testing of many of Tryphon's different navigation systems. Figure 3–3 shows the multiple sensors that have been added to the virtual Tryphon in Gazebo.

Gazebo offers several plug-ins for sensors, which integrate with ROS and send messages which can directly be used by ROS programs. For rendezvous and docking of Tryphon, IMU, compass and camera plug-ins are used. An IMU and compass are placed on each Tryphon, in the exact positions and orientations found on the physical platform, with added noise profiles obtained from experiments. Cameras have been placed in several different locations to match the navigation systems that will be discussed in sections 5.2.1 and 5.3.2. Cameras located on the top of Tryphon are for rendezvous and use fish-eye lenses on the real platform. Since fish-eye lenses cannot be simulated in Gazebo, two cameras are placed in close proximity to emulate

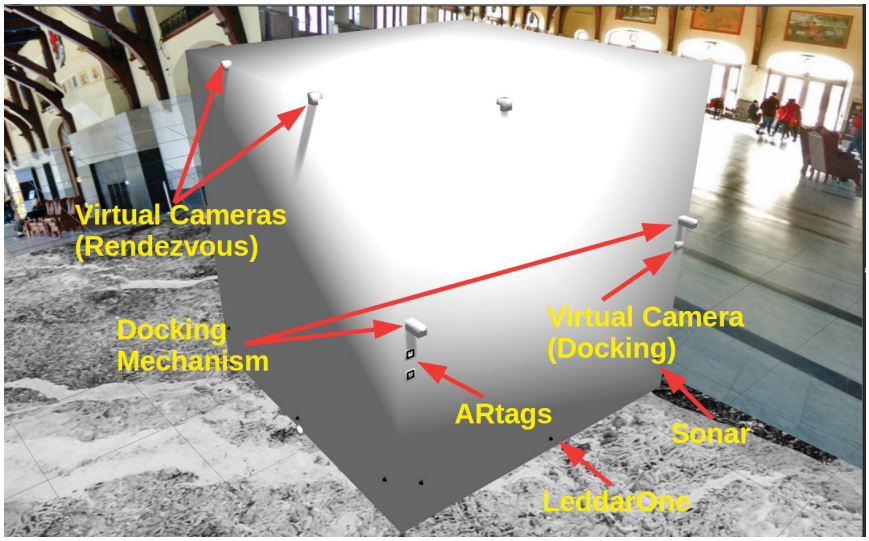

Figure 3–3: Location of sensors on Tryphon in Gazebo

the same field of view as one fish-eye lens. The cameras located in the middle of the vertical sides are employed for localization during docking and are aligned vertically with the top ARtag of the opposing Tryphon when docked. In simulation, one docking camera is placed on each of the Tryphons (chaser and target) because of the convenience of loading symmetric models in Gazebo, although on the physical Tryphon two docking cameras are placed on the chaser only. Unfortunately due to lighting effects of Gazebo, the implemented camera/ARtag system's noise and performance do not accurately represent those of the real system; therefore, perfect corresponding measurements are used which are corrupted with Gaussian noise. The docking cameras' vision feedback during simulations is still useful for tuning and analysis, and the camera view of the MCPTAM and ARtag systems during the rendezvous and docking scenario can be seen in the bottom frame of figure 3–4. In addition to these systems, the Gazebo model also includes sonar and LeddarOne time

Figure 3–4: Camera vision of rendezvous and docking in Gazebo with the first panel showing the Tryphons in the gazebo environment, the second panel showing the camera vision used for MCPTAM and the third panel showing the camera vision used for docking

of flight sensor systems, which use custom plug-ins. The Gazebo model includes each of the above sensors at all times, although on the physical platform this is not the case, due to weight, computational and power consumption limitations. To this end, the weight of each sensor is set to zero and assumed to be included in the assigned payload weight of the simulation, leading the the proper total mass but slightly incorrect weight distribution.

CHAPTER 4
Regulation of Tryphon using State and Output Feedback Control

Before pursuing the rendezvous and docking of two Tryphons, the regulation of Tryphon at a constant desired pose is a necessary first step. Here, two methodologies for regulation are presented: regulation under PID control to demonstrate the ability of the target Tryphon to remain at a desired pose and thus validating the assumption of a fixed target, and similarly the regulation of the chaser Tryphon in front of a wall with an ARtag set-up using an output feedback controller. The objective of the latter is to observe the performance of controlling the chaser with the camera/ARtag system. In this chapter, the output feedback controller used for regulation and docking is presented, with experimental results. Next, an investigation into the effects of a center of mass offset is presented to determine the reasons for the unexpected behaviour of the system observed in the experiments. Results are then presented of regulation experiments conducted using PID control and the global localization solution of section 5.2.1. Finally, an analysis on the relative regulation of a controlled chaser and target is presented, combining concepts of the previously described methodologies to determine the strategy and approach for the next chapter.

4.1 Output Feedback Controller

Using the state-space model derived in section 2.2.3, the closed-loop output feedback controller:

$$\mathbf{u}_\delta = -\mathbf{K}\mathbf{y} \tag{4.1}$$

is designed using the pole placement technique and generalised matrix inverse approach [33]. Using the pole placement technique to choose the closed-loop poles of the system under state-feedback control leads to an intermediate gain matrix $\mathbf{K}'$. The output feedback gain matrix $\mathbf{K}$ is then found from:

$$\mathbf{K} = \mathbf{K}'\hat{\mathbf{C}}_0^\dagger \tag{4.2}$$

where $\hat{\mathbf{C}}_0^\dagger$ represents the Moore-Penrose pseudoinverse of the state estimation matrix $\hat{\mathbf{C}}_0$. The block diagram of the system is included in figure 4–1. The system has the closed-loop state equation:

$$\dot{\mathbf{x}}_\delta = (\mathbf{A}_0 - \mathbf{B}_0\mathbf{K}\hat{\mathbf{C}}_0)\mathbf{x}_\delta + \mathbf{B}_0\mathbf{r}(t) \tag{4.3}$$

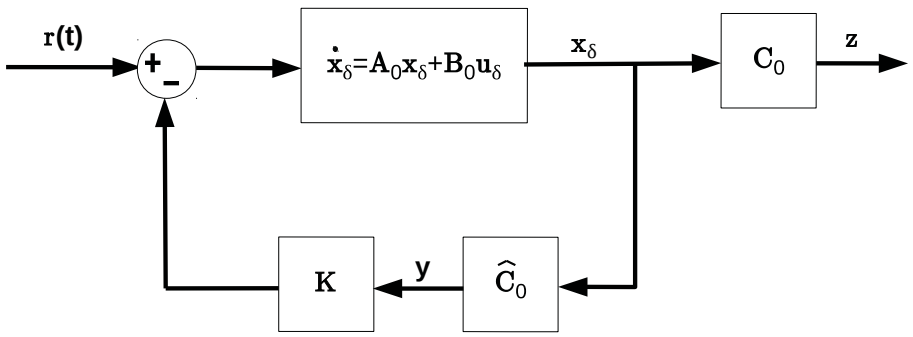

Figure 4–1: Block diagram of output feedback control

whose characteristic polynomial and thus poles can be chosen with the gain matrix **K** due to the assignability criteria of the system as discussed in section 2.2.3.

Since the objective of this controller is to essentially be used for the docking scenario, it is tuned in this regard and then used for regulation tests. For docking purposes, a controller with gain matrix **K** which docks the chaser Tryphon with the target with as little overshoot as possible is desired. For this reason, all closed-loop poles of the system are chosen to be critically damped. Furthermore, the Tryphon's propellers have a relatively low maximum thrust (T_{max}), and therefore gains which do not demand control inputs exceeding these values while tracking trajectories are ideal.

The closed-loop, output feedback controller formulated above has been designed with the assumption of neutral buoyancy, since the actual difference between the buoyancy and gravity forces is expected to be small, however, unknown and time-varying. The system, state and output feedback gain matrix are augmented by adding an integral action term in z to compensate for the difference between the weight and buoyancy forces.

4.2 Experimental Results

The output feedback controller presented in the previous section is used to perform preliminary chaser regulation experiments in front of a wall with ARtags mounted on it, as seen in figure 4–2. These experiments were conducted as part of a residency at the University of Laval, in Quebec City. The controller was designed to place the poles of the system at: $-\{\lambda_{1-6} = 0.2,\ 0.3,\ 0.4,\ 0.29,\ 1.1,\ 0.1,\ 0.23\}$. No state estimation was developed for this experiment because the low noise of

Figure 4–2: Set-up for regulation experiments using output feedback controller

the camera/ARtag system was considered acceptable, and a simple finite difference method of the measurements from five previous time steps was used to compute the time derivatives of $\mathbf{r}_1^B$ and $\mathbf{r}_2^B$. After initial tuning, it was also determined that roll and pitch control was not performing as expected and hence, the experiment was switched to having control of only the other four DOFs. The control of roll and pitch is normally unnecessary on Tryphon for simple regulation tasks, but is important for docking to ensure the alignment of the docking mechanisms. The omission of these two control inputs has been consistent throughout past work with Tryphons, because of their passive stabilisation combined with the damping from drag, and the lack of reliable roll and pitch measurements from the IMU as it is generally placed near a motor, thus effecting its performance. While a simple solution would be to place the IMU elsewhere, this was not possible for these experiments as the IMU is located on the microPC which cannot be moved because of the electronic scheme of the platform. This problem was resolved for subsequent experiments discussed in

Chapter 6 with the addition of another IMU placed far from motors, allowing roll and pitch to be measured accurately and controlled effectively.

The closed-loop poles of the linear system after removing the roll and pitch control are: $-\{\lambda_{1-4} = 0.2,\ 0.3,\ 0.4,\ \pm 1.11i,\ 0.23,\ \pm 1.11i,\ 1.1\}$, where the imaginary poles correspond to the uncontrolled roll and pitch dynamics. When considering the damping induced by drag, the closed-loop system is expected to be asymptotically stable in all six degrees of freedom. However, several experiments conducted showed an instability in the system, contrary to what is expected from the closed-loop pole analysis. Figure 4–3 shows the results of one of the regulation experiments with no roll or pitch control. It is obvious from the results that roll and z-components of the relative positions are unstable, with the control input in z increasing to large values. The coupling between roll and z causes the oscillations in roll to directly destabilize the system in z. Of course the addition of roll and pitch control with satisfactory measurements would stabilize the system, which is accomplished in future experiments; however, an understanding of the causes of the observed unexpected instability is important in optimizing the performance of the controller.

4.3 Center of Mass Offset's Effect on Stability

In this section, the case where the center of mass is slightly offset along the y-axis of the chaser cube is further investigated and Simulink/SimMechanics simulation results will be compared to those obtained in the regulation experiments of section 4.2. Using the model developed in section 2.2.4, the effects of this offset on the stability of the system under closed-loop control can be observed. Similarly to the experiments, x, y, z and yaw are controlled for this investigation, while roll and pitch

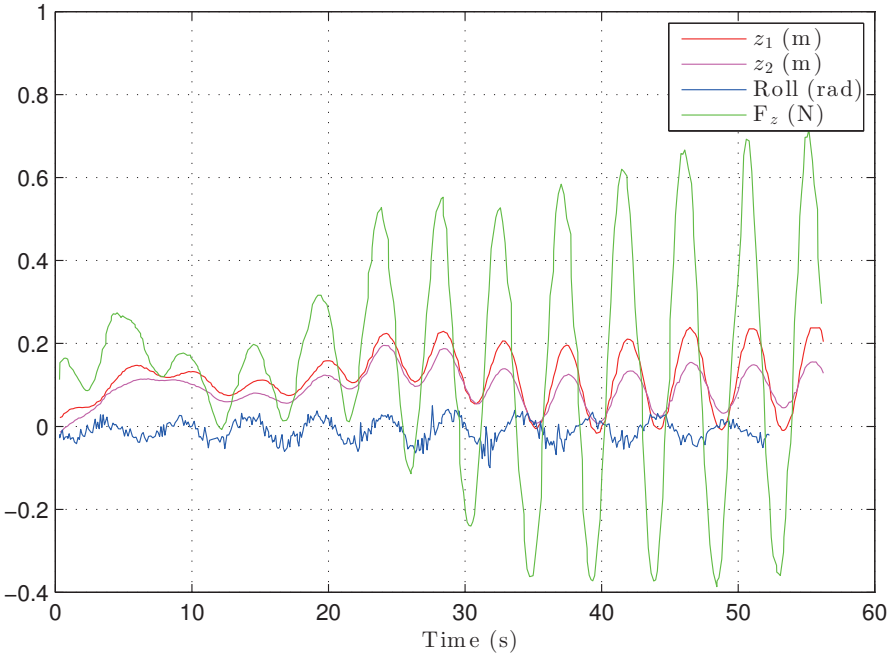

Figure 4–3: Chaser regulation experimental response (positive y-axis center of mass offset)

are left uncontrolled. Intuitively, changes in orientation of the chaser directly affect the measurements $\mathbf{r}_1^B$ and $\mathbf{r}_2^B$; however. since these vectors are expressed in the body-fixed frame, how these components vary is not so obvious. For example, a roll rotation not only affects the z components of $\mathbf{r}_1^B$ and $\mathbf{r}_2^B$ because of the actual displacement of the camera in the inertial frame, but also because these vectors are being resolved in the body-fixed frame which has rotated. This coupling can cause an instability in z if roll becomes unstable. At the same time, with the passive stabilization of the buoyancy force and with damping from the drag, roll can only be destabilized with control inputs; yet this was not the case in the experiments of section 4.2, where no roll control was present but an instability still occurred. This

reasoning suggests a coupling between the control in the z direction and the roll angle, or more specifically a roll moment induced by thrust control, which is not present in the ideal model. Considering the symmetric force distribution of the cube for thrust in the z direction seen in figure 2–3, it is clear that an offset in the center of mass must be present for the thrusts in z to induce a roll moment.

To validate the earlier hypothesis, in simulation, the center of mass of the chaser cube is shifted in the y-axis, in alternately the positive and negative directions. A specified offset of 0.03 m is used, which is exaggerated compared to a realistic offset as it suggests a roll at equilibrium of over 0.1745 rad. Such a large offset is used to make the effects more apparent in the figures, which is justified since similar results can be seen in offsets as small as 0.005 m, but at a smaller scale. Here, the chaser Tryphon attempts to regulate at a desired position from the target, using the x, y, z and yaw control of the output feedback controller presented earlier.

Figure 4–4 displays the results from the non-linear simulation presented in section 3.1, with all initial conditions at zero except a roll angle of 0.08 rad. From this figure it is clear that a negative offset improves the performance of the system. When an offset exists in the positive y-axis, the performance of the system degrades and becomes unstable. These tests were carried out for numerous different initial conditions, all producing qualitatively similar results. This trend is apparent in the linear model of section 2.2.4 as well, and an analysis of the closed-loop poles of the system verifies these results.

With closer examination, the three curves in figure 4–4 are periodic and have the same frequency. An important detail is the force applied in the z-axis is always

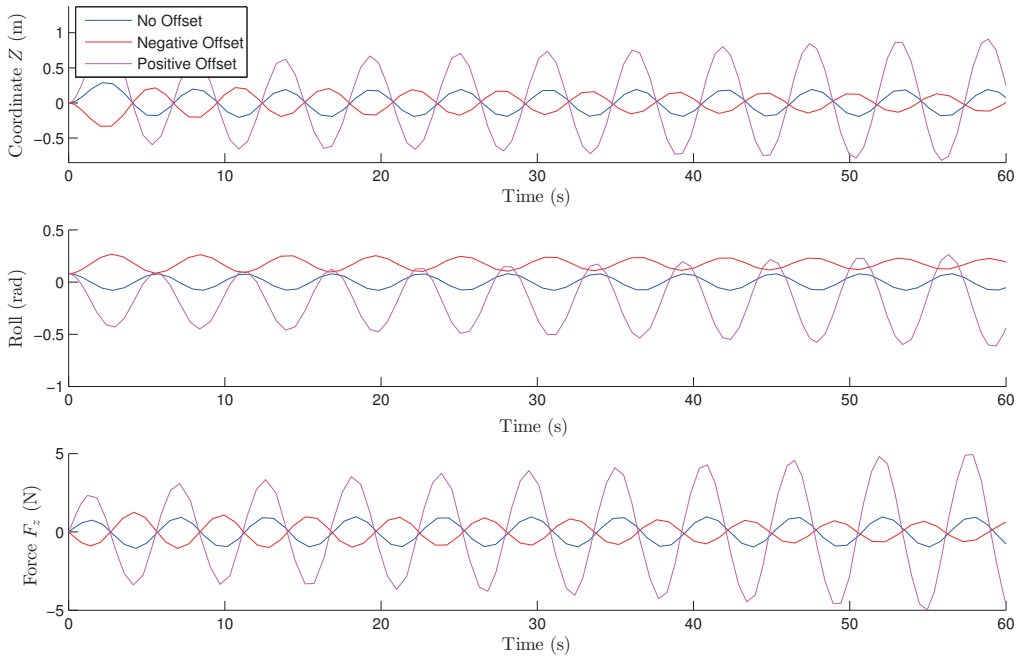

Figure 4–4: Comparison of closed-loop response with and without center of mass offset (simulation)

positive when roll is decreasing, and thus angular velocity p is negative. A positive thrust in z combined with an offset in the center of mass would induce a positive moment for a negative offset, and a negative moment for a positive offset, and the opposite for a negative thrust, as illustrated in figure 4–5. The result is a controller which is inadvertently adding to the rolling motion of the cube when a positive offset in the y-axis is present, and negating it when a negative offset is present.

Following these results, it is clear that the location of the center of mass is very important for the stability of the system, when no roll or pitch control is present. Since the position of the center of mass is continuously varying and is difficult to

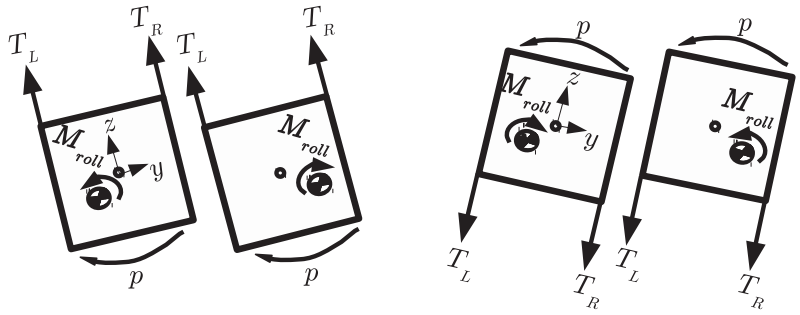

Figure 4–5: Induced roll moment from symmetric force distribution with (a) $+z$ thrust and (b) $-z$ thrust, having $\pm y$-axis center of mass offsets

determine accurately, it is not feasible to include center of mass offsets in the controller design. Based on this analysis, ensuring that the center of mass of the chaser is placed with a negative y-offset (by adding appropriate weight distribution), can ensure the stability of the system, and this has been done in the docking experiments to be presented in Chapter 6.

4.4 Regulation under PID Control for Stationary Target

The output feedback controller designed in section 4.1 uses the linear model of section 2.2.3, which assumes a fixed target Tryphon. The basis for this assumption comes from the ability to accurately control the target to remain stationary at a desired location under closed-loop control. From [1], accurate control of a single Tryphon has been achieved, and figure 4–6 shows the results of a regulation experiment under closed-loop control, using the discrete PID controller and MCPTAM navigation system as described in Chapter 5. From the results, the error observed in the X and Y-axes are always below approximately 8 cm, with errors of approximately

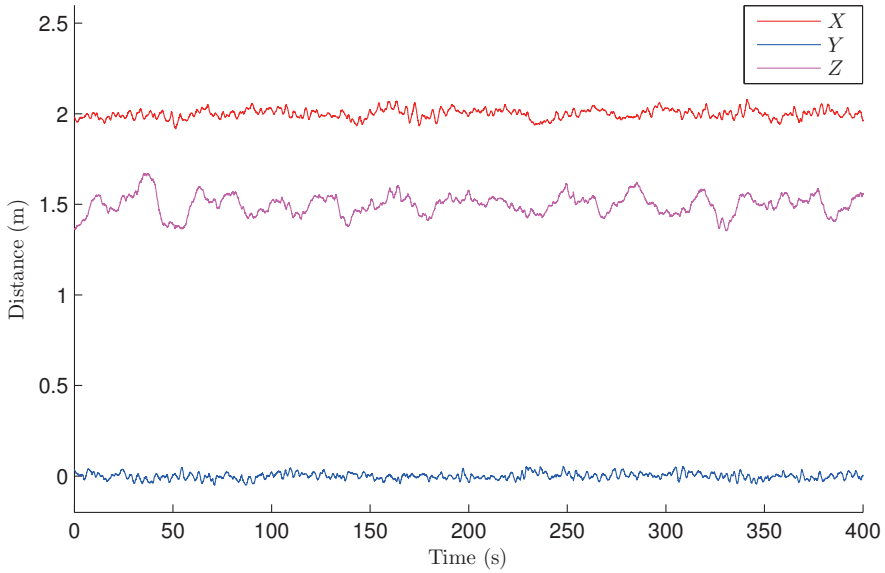

Figure 4–6: Regulation experimental results using PID control and global position feedback

20 cm along the Z-axis. Regulation of Tryphon in height (Z) is the most difficult because of the presence of the buoyancy force, and thus it is normal to see better performance in the other two directions. It is important to note that the error values just cited are found from the estimated position values obtained in experiments, which are themselves subject to error. This performance is deemed acceptable for the assumption of a stationary target when under closed-loop control.

4.5 Level of Cooperation

Thus far in this chapter, the output feedback control for regulating the chaser Tryphon with the ARtag pairs mounted on a wall have been considered, as well as sample regulation results of the target Tryphon achieved in previous work. The focus of this section is to observe the regulation performance of the Tryphon chaser/target

system under different levels of cooperation, and these results are used to define the docking strategy discussed in the next chapter. It is from this analysis that the choice was made to keep the target Tryphon stationary, under its own absolute position feedback for docking the two Tryphons.

Having accurate control and localization of both Tryphon blimps allows for full cooperation during a docking task, and of course intermediate levels of cooperation. As the Tryphons move closer together, slight errors in their estimated state or offsets from their desired states can cause the entire docking manoeuvre to fail. For this reason, it is important to decide what level of information and interaction the chaser and target Tryphon should have with regards to each other, i.e., level of cooperation between chaser and target. Since the global position of each Tryphon is known from MCPTAM navigation during the rendezvous stage and the relative position is measured using camera/ARtag pair (Chapter 5), there are three possible cases for desired inputs for Tryphon docking:

Case 1: global (absolute) reference input for positioning both the chaser and target at the docking pose

Case 2: relative reference input defined for one Tryphon as the other Tryphons' state

Case 3: relative reference input given to chaser and global reference input given to target

Clearly, each case has its advantages and disadvantages. If a disturbance occurs, or one Tryphon has slight error in its desired and current state, then the other Tryphon cannot compensate for this in Case 1, whereas it is possible in Case 2 and Case 3. On the other hand, in Case 1, each Tryphon is controlled independently

of the other, reducing the possibility of undesired and erratic results. These factors can greatly impact the final performance of a docking manoeuvre. The equations of motion for each of the 3 Cases will now be presented, considering only the 1 DOF dynamics in the Z direction in order to simplify the analysis. This is followed by a presentation of simulation results in the Z-axis for the 3 cases.

4.5.1 1 DOF Equations of Motion

For each of the three cases introduced earlier, we model the Tryphons as 1 DOF particles subject to drag and control inputs. Therefore, the equations of motion of the chaser and target Tryphon are given by:

$$m_c\ddot{Z}_c + c_c\dot{Z}_c\|\dot{Z}_c\| = u_c \tag{4.4}$$

$$m_t\ddot{Z}_t + c_t\dot{Z}_t\|\dot{Z}_t\| = u_t \tag{4.5}$$

Subtracting equation (4.5) from (4.4), neglecting drag, and noting that $m_c = m_t = m$, the problem is reduced to:

$$\ddot{\zeta} = \frac{u_c}{m} - \frac{u_t}{m} \tag{4.6}$$

where $\zeta = Z_c - Z_t$. By omitting the integral term for simplicity, the output feedback controller described in section 4.1 can be equivalently stated as a PD controller when applied to the single dimension of Z. Furthermore, the controller used for rendezvous is essentially a PD controller, therefore a PD controller will be used here to represent both control methodologies normally used given either global and/or relative feedback, such as in the three Cases. The control law for each Case will now be presented individually, where the proportional and derivative gains are the same on each Tryphon.

Case 1

In Case 1, the control inputs u_c and u_t are given by:

$$u_c = -K_P(Z_c - Z_{cd}) - K_D(\dot{Z}_c - \dot{Z}_{cd}) \tag{4.7}$$

$$u_t = -K_P(Z_t - Z_{td}) - K_D(\dot{Z}_t - \dot{Z}_{td}) \tag{4.8}$$

where the subscript d corresponds to the desired reference input and we note that the feedback error is computed as the difference of the absolute positions. Substituting the control inputs into equation (4.6) and setting the desired reference inputs for the chaser and target to the same values leads to:

$$\ddot{\zeta} + \frac{K_D}{m}\dot{\zeta} + \frac{K_P}{m}\zeta = 0 \tag{4.9}$$

Case 2

For Case 2, u_c and u_t are given by:

$$u_c = -K_P\zeta - K_D\dot{\zeta} \tag{4.10}$$

$$u_t = K_P\zeta + K_D\dot{\zeta} \tag{4.11}$$

where for each chaser and target, the state of the opposing Tryphon has been defined as the desired state. Substituting these equations into equation (4.6) results in:

$$\ddot{\zeta} + \frac{2K_D}{m}\dot{\zeta} + \frac{2K_P}{m}\zeta = 0 \tag{4.12}$$

Case 3

For Case 3, u_c and u_t are given by:

$$u_c = -K_P\zeta - K_D\dot{\zeta} \tag{4.13}$$

$$u_t = -K_P(Z_t - Z_{td}) - K_D(\dot{Z}_t - \dot{Z}_{td}) \tag{4.14}$$

where no reduction to a single closed-loop dynamics equation is possible and the control laws are substituted into equations (4.4) and (4.5) to obtain closed-loop dynamics.

4.5.2 Simulation Results of Cases 1-3

According to the closed-loop equations for the three cases above, with appropriate choices of gains the system should successfully settle with the chaser and target having the same height. Now Gazebo simulation results are presented for each of the three Cases to observe their performance and effectiveness on the more realistic system. The simulation is done with control in the Z-axis only, using the Kalman filter presented in Chapter 5 and the respective PD controllers of each Case, with K_P and K_D equal to 0.97 and 5.94 respectively. The respective poles for Cases 1, 2 and 3 are $-.1291 \pm 0.1597$,$-.2583 \pm 0.1329$ and twice of $(-.1291 \pm 0.1597)$. The simulation environment and parameters remain the same across all tests. The initial conditions for the chaser and target Tryphons are 3.5 m and 2 m in height respectively.

Figure 4–7 shows the simulation results of the three cases. The top sub-plot is for Case 1, when both Tryphons receive a global reference input located halfway between the starting position of the two, at 2.75 m. The middle sub-plot shows the simulation results for Case 2, when both Tryphons are using relative state feedback. The bottom

sub-plot shows the simulation results for Case 3, when the target Tryphon receives a global reference input located at 2.75 m, and the chaser Tryphon is using relative state feedback. In Case 1 and Case 3, the Tryphons successfully settle to their desired position, whereas in Case 2 the response of the system is rather poor, and the two Tryphons continue to oscillate.

The Gazebo model, as described in Chapter 3, introduces several changes to the ideal scenario represented by the relative equations of motion derived earlier. In particular, the introduction of measurement noise and actuator saturation affect all three Cases negatively, and it has been determined that the time delay in the state estimation output has a significant effect on Case 2 which is the primary reason for its poor performance. In the end, the performance observed for Case 1 and Case 3 is comparable, with Case 1 being slightly better, although the relative localization of Case 3 presents greater advantages since the camera/ARtag system has proven to be more accurate and reliable than MCPTAM. For these reasons, Case 3 will be used to define the docking scenario for the two Tryphons.

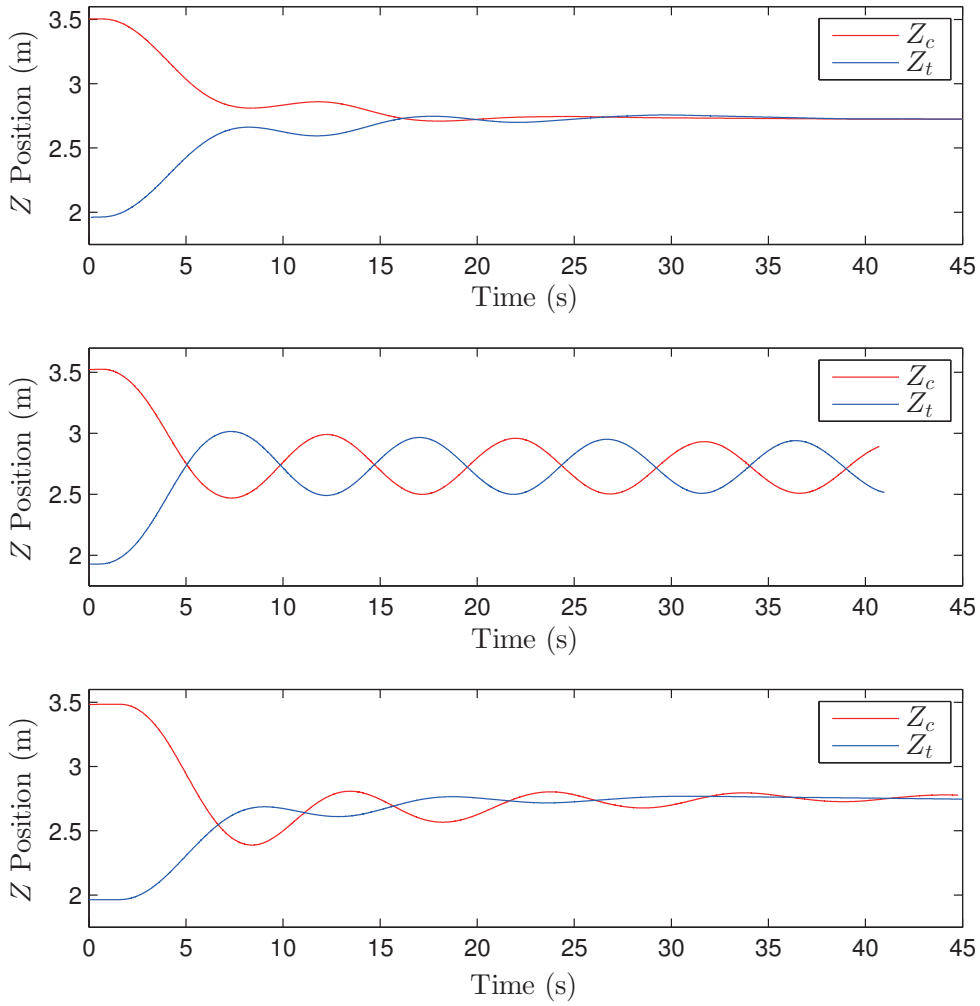

Figure 4–7: Z regulation for three cases, with top sub-plot having both Tryphons given global reference inputs (Case 1), middle sub-plot both Tryphons using relative state feedback (Case 2) and bottom sub-plot having chaser Tryphon using relative state feedback and target Tryphon given a global reference input (Case 3)

CHAPTER 5
Guidance, Navigation and Control for Rendezvous and Docking

As discussed earlier, the full docking scenario of Tryphon blimps has been divided into two stages: rendezvous and docking. The rendezvous stage brings the chaser and target Tryphons close together to a predefined distance and orientation to prepare for the docking stage. Once rendezvous is complete, the docking stage begins, where the GNC systems involved must ensure the required accuracy for successful docking mechanism contacts. This chapter begins by detailing the strategy and approach used for the rendezvous and docking of two Tryphons. The GNC systems are then presented for the rendezvous stage, followed by the docking stage. The chapter ends with the presentation of simulation results for a complete rendezvous and docking manoeuvre.

5.1 Strategy/Approach

The docking of two large, cubic blimps is not a simple endeavour, and therefore an effective docking mechanism alone does not suffice to successfully accomplish such a task; a robust and accurate docking strategy is also required. The goal of rendezvous is to bring the chaser and target close together, given any relative initial pose between them. During the rendezvous stage, each Tryphon acts independently and uses the MCPTAM global localization system and discrete PID controller presented in [1] to manoeuvre to the desired pre-dock position. Future artistic performances may require a specified, visually appealing trajectory during the rendezvous stage,

but for the purposes of this research a simple waypoint-based guidance system is used. The final positions of the chaser and target Tryphon after the rendezvous stage do not need to be precise, and are mainly a guideline to set-up for the docking stage, but with one mandatory requirement: the target's ARTag markers must be within the field of view of the chaser's cameras. Once this condition is met, the navigation system of the chaser is ready to switch from global localization to relative localization, and the docking stage may begin.

Following the results of section 4.5, the strategy used during the docking stage is as follows: the target Tryphon is to remain stationary at its desired pose using the rendezvous (absolute) navigation and control system, while the chaser Tryphon switches to the camera/ARtag (relative) navigation system and output feedback controller. A glideslope guidance algorithm is used, which at the beginning of the docking stage, generates two trajectories which are tracked by the output feedback controller. The docking stage ends upon the successful contact of both electromagnets with their counterpart metallic plates.

5.2 Rendezvous Stage

In this section, the details of the GNC system implemented on Tryphons in [1] and used for the rendezvous stage are presented. As previously stated, the guidance system used for the rendezvous stage consists of a basic waypoint-based guidance method, where either a specific desired state or set of desired states are tracked by the controller. The work in this section is based on the dynamics model presented in [1], where unlike the model presented in Chapter 2, the translational equations of motion are stated in the inertial frame, with origin located in the space where

simulation/experiments are conducted. As a result, both the controller and state estimator of this section use X, Y, and Z coordinates for translation of the chaser Tryphon.

5.2.1 Sensing

The sensors used on Tryphon during the rendezvous stage include the IMU's gyroscope for angular velocities and multi-camera parallel tracking and mapping for full pose. This section will focus on a brief introduction to the vision-based global localization software, MCPTAM, developped by Harmat et al. [34][35] for UAVs.

MCPTAM functions, as its name suggests, by providing the pose of a cluster of multiple rigidly-mounted cameras while simultaneously tracking features of the environment and building a map. The algorithm requires large computation times, and as a result it must be executed off-board for the Tryphon system where the compressed images are streamed through WiFi from the Tryphon to the ground station. Furthermore, two synchronised cameras must be used in order to build a map, but because of the limitations of the Gumstix board, the frame-rate achieved with two synchronised cameras (2 Hz) on the blimp is too low to be used for real-time control. Fortunately, MCPTAM has a feature to build and save a map of the environment, which can then be used to localize and give a pose relative to the origin of the map. To this end, at any given residency, a map of the room is built using two synchronised cameras operated from the ground station, which is then saved and loaded by MCPTAM. A single camera mounted on the Tryphon is then used with MCPTAM for Tryphon tracking only, running at 10 Hz. The noise covariances of the IMU and MCPTAM have been determined experimentally in [1].

5.2.2 State Estimation

The sensing equipment found on Tryphon differs for any given residency; therefore, a state estimator which can be easily modified to incorporate different combinations of sensor measurements in order to obtain the necessary feedback for the controllers is required. Taking advantage of the modularity provided by ROS, a basic kinematics-based Kalman filter has been developed, which is capable of working with numerous sensor combinations normally used with Tryphon. The modular Kalman filter will now be presented in its discrete form, whose formulation is used for both rendezvous and docking, although with different sensors and estimated states. The slight alterations for the docking stage will be presented later in section 5.3.4, where the state estimator is also validated.

Consider the kinematics based linear process model

$$\mathbf{x}_k^i = \mathbf{F}^i \mathbf{x}_{k-1}^i + \mathbf{w}_{k-1}^i \tag{5.1}$$

with measurements also linearly dependant on the state:

$$\mathbf{z}_k^i = \mathbf{H}^i \mathbf{x}_k^i + \mathbf{v}_k^i \tag{5.2}$$

where $\mathbf{w}_{k-1}^i$ and $\mathbf{v}_k^i$ represent the process and measurement noise and have a normal probability distribution with covariance matrices $\mathbf{Q}^i$ and $\mathbf{R}^i$, respectively, for a sensor $i = 1, 2, .., q$, where q is the total number of sensors. Furthermore, let j represent the number of measurements given by the particular sensor i. We define the kinematics

process matrix $\mathbf{F}^i$ and matrix $\mathbf{H}^i$ as:

$$\mathbf{F}^i = \begin{bmatrix} \mathbf{I}_{j\times j} & \mathbf{I}_{j\times j}\Delta t & \mathbf{I}_{j\times j}\frac{\Delta t^2}{2} \\ \mathbf{0}_{j\times j} & \mathbf{I}_{j\times j} & \mathbf{I}_{j\times j}\Delta t \\ \mathbf{0}_{j\times j} & \mathbf{0}_{j\times j} & \mathbf{I}_{j\times j} \end{bmatrix} \tag{5.3}$$

$$\mathbf{H}^i = \begin{bmatrix} \mathbf{I}_{j\times j} & \mathbf{0}_{j\times 2j} \end{bmatrix} \tag{5.4}$$

and the estimator/filter state as including the physical state (corresponding to what is being measured) and its first and second time derivatives. More specifically, each $\mathbf{x}_k^i$, as well as the estimated states presented later, contain the respective sensor's measurements and corresponding time derivatives, i.e., $\mathbf{x}^i = [(\mathbf{z}^i)^T, (\dot{\mathbf{z}}^i)^T, (\ddot{\mathbf{z}}^i)^T]^T$. Clearly, with regard to $\mathbf{H}^i$, all appropriate measurement transformations into the proper frames and locations are done outside of the Kalman filter before use to allow this modular format. This framework essentially treats rotations as vectors, which we assume is acceptable given that the Tryphons undergo only small roll and pitch angles and the update rates used on the Tryphons are reasonably high: the Kalman filter runs at 100Hz, with each sensor updating at its own frequency and Δt being dynamically computed by taking the difference in ROS timestamps for improved accuracy.

The size of $\mathbf{R}^i$ is $j \times j$, the size of the error covariance matrix $\mathbf{P}^i$ is $3j \times 3j$, and $\mathbf{Q}^i$ is given as:

$$\mathbf{Q}^i = \begin{bmatrix} \mathbf{I}_{j\times j}\frac{\Delta t^5}{20} & \mathbf{0}_{j\times j} & \mathbf{0}_{j\times j} \\ \mathbf{0}_{j\times j} & \mathbf{I}_{j\times j}\frac{\Delta t^3}{3} & \mathbf{0}_{j\times j} \\ \mathbf{0}_{j\times j} & \mathbf{0}_{j\times j} & \mathbf{I}_{j\times j}\Delta t \end{bmatrix} \tag{5.5}$$

The implemented discrete Kalman filter algorithm following the prediction/correction scheme, with the superscript i dropped for simplicity, is as follows:

Predict:

$$\hat{\mathbf{x}}_k^- = \mathbf{F}\hat{\mathbf{x}}_{k-1} \tag{5.6}$$

$$\mathbf{P}_k^- = \mathbf{F}\mathbf{P}_{k-1}\mathbf{F}^T + \mathbf{Q} \tag{5.7}$$

Correct:

$$\mathbf{K}_k = \mathbf{P}_k^-\mathbf{H}^T(\mathbf{H}\mathbf{P}_k^-\mathbf{H}^T + \mathbf{R})^{-1} \tag{5.8}$$

$$\hat{\mathbf{x}}_k = \hat{\mathbf{x}}_k^- + \mathbf{K}_k(\mathbf{z}_k - \mathbf{H}\hat{\mathbf{x}}_k^-) \tag{5.9}$$

$$\mathbf{P}_k = (\mathbf{I}_{3j\times 3j} - \mathbf{K}_k\mathbf{H})\mathbf{P}_k^- \tag{5.10}$$

where the superscript $(\ )^-$ represents the predicted values.

In the case of rendezvous, $q = 2$, where the sensors and the relevant values and definitions are found in Table 5–1. Certain estimated values are unused in the final state estimate $\hat{\mathbf{x}}$, and are only used to enhance the estimates needed. To form $\hat{\mathbf{x}}$, selected components of $\hat{\mathbf{x}}_k^i$ can be combined across all sensors, and those selected for $\hat{\mathbf{x}}$ are found in Table 5–1. It is important to note that while translational velocities are included in the state estimate $\hat{\mathbf{x}}$, these are not used with the discrete PID controller which will be presented in the next section, since time derivatives are included within the discrete implementation. Nevertheless these are included since several other controller implementations commonly used with Tryphon require these velocity estimates. While a setup such as this benefits Tryphons in filtering measurements and obtaining the required state feedback, this formulation does not

Table 5–1: Rendezvous Kalman filter sensor parameters

Sensor # (i)	Sensor	j	Measurements ($\mathbf{z}_k^i$)	Selected for $\hat{\mathbf{x}}$	Measurement update frequency (Hz)
1	MCPTAM	6	$[X, Y, Z, \phi, \theta, \psi]^T$	$X, Y, Z, \phi, \theta, \psi, \dot{X}, \dot{Y}, \dot{Z}$	10
2	IMU	3	$[\omega_x, \omega_y, \omega_z]^T$	$\omega_x, \omega_y, \omega_z$	100

allow for sensor fusion, and hence is not capable of fusing state estimates of the same states from different sensors.

5.2.3 Control

For rendezvous, a controller which is capable of regulation control and waypoint tracking is required. As seen from section 4.4, the discrete PID controller used in [1] is fully capable of regulation, and this controller is used for the chaser and target rendezvous manoeuvres, as well as on the target Tryphon when it regulates at a stationary pose during the docking stage.

The PID controller consists of six single input, single output control laws, which computes control forces in the inertial frame, and control moments in the body-fixed frame, using the corresponding error terms between the desired state and state outputs of the Kalman filter presented earlier. From [1], the general discrete formulation of the PID using a sampling rate of T = 10Hz and the Tustin method [36] is:

$$\frac{U(\mathrm{z})}{E(\mathrm{z})} = K_p + K_i \frac{1}{(\frac{2}{\mathrm{T}}\frac{\mathrm{z}-1}{\mathrm{z}-1})} + K_d \frac{(\frac{2}{\mathrm{T}}\frac{\mathrm{z}-1}{\mathrm{z}+1})}{\frac{K_d(\frac{2}{\mathrm{T}}\frac{\mathrm{z}-1}{\mathrm{z}+1})}{N} + 1} \tag{5.11}$$

where $U(\mathrm{z})$ is the control input, $E(\mathrm{z})$ is the error input, N is the first-order derivative filter divisor and $K_p,\ K_i,$ and K_d are the proportional, integral and derivative gains.

The gains of the discrete PID controller for the rendezvous manoeuvre are shown in Table 5–2.

Table 5–2: Discrete PID gains [1]

Input	X	Y	Z	ϕ	θ	ψ
K_p	3.2	3.2	3.2	0.2	0.2	3.0
K_i	0	0	0.1	0	0	0
K_d	20.8	20.8	20.8	1.0	1.0	15.0
N	100	100	100	100	100	100

5.3 Docking

For docking, the output feedback controller presented in section 4.1 is used to track the trajectories generated by a glideslope guidance algorithm, using the estimated output given by a Kalman filter. The docking stage requires greater precision and robustness than the rendezvous stage for a successful manoeuvre, which is why relative control and navigation have been used, based on the dynamics model presented in Chapter 2. The guidance and navigation systems used for the docking stage are now presented.

5.3.1 Glideslope Guidance

A trajectory tracking method which controls the final approach velocity allowing for soft docking is ideal. Furthermore, when considering that the design of the docking receiver's cone is robust to lateral misalignments of up to 4.25 cm and is capable of guiding the electro-magnet, it is desirable to have little overshoot and low speeds when the docking mechanisms come into contact to avoid a rebound effect. A glideslope guidance algorithm has been chosen for these reasons, combined with

the advantage of having a reduction in control effort near the end of the docking stage, which for spacecraft, reduces the plume impingement on the target [37], and for the case of Tryphons, reduces the effects of propwash. According to the glideslope guidance formulation in [10], the algorithm generates a straight line path from the initial location of the chaser to the final docked position with the target. For Tryphon docking, the trajectory is generated in the body-fixed frame of the chaser.

Let $\rho(t)$ be the distance-to-go and $\dot{\rho}(t)$ be the approach velocity of the chaser which decreases linearly with $\rho(t)$. Specified parameters for the algorithm include the glideslope a (< 0), and the final commanded arrival velocity $\dot{\rho}_T < 0$. Combining these specified parameters with the initial distance-to-go ρ_0, determined from the initial position $\boldsymbol{\rho}_0^B$ ($\rho_0 = ||\vec{\boldsymbol{\rho}_0}||$) , results in an initial commanded velocity $\dot{\rho}_0 < 0$ and manoeuvre period T given as:

$$\dot{\rho}_0 = a\rho_0 + \dot{\rho}_T \tag{5.12}$$

$$T = \frac{1}{a} \ln \frac{\dot{\rho}_T}{\dot{\rho}_0} \tag{5.13}$$

The glideslope guidance algorithm is now defined by the differential equation:

$$\dot{\rho}(t) = a\rho(t) + \dot{\rho}_T \tag{5.14}$$

whose solution is:

$$\rho(t) = \rho_0 e^{at} + \frac{\dot{\rho}_T}{a}(e^{at} - 1) \tag{5.15}$$

The vectors corresponding to the trajectory to be tracked [37] are defined as :

$$\begin{aligned} \dot{\boldsymbol{\rho}}^B(t) &= \dot{\rho}(t)\hat{\mathbf{u}}^B \\ \boldsymbol{\rho}^B(t) &= \rho(t)\hat{\mathbf{u}}^B \end{aligned} \tag{5.16}$$

where $\hat{\mathbf{u}}^B = [\cos\beta_1 \ \cos\beta_2 \ \cos\beta_3]^T$, and $\cos\beta_1$, $\cos\beta_2$ and $\cos\beta_3$ are the direction cosines of $\boldsymbol{\rho}_0^B$.

For the case of Tryphon docking, a novel approach is implemented where two glideslope trajectories are generated, one for each of the two docking mechanism parts. These two desired trajectories are tracked by the control simultaneously, which reduces the relative distance and orientation between the chaser and target. Ideally, parameters should be chosen so that the manoeuvre periods for each glideslope trajectory are identical, resulting in both ends docking simultaneously. To do this, the final commanded arrival velocities at the two docks are set equal ($\dot{\rho}_{T1} = \dot{\rho}_{T2}$) to the value desired for soft docking, and the glideslope for the trajectory with the largest initial distance-to-go (ρ_{01}), call this a_1, is chosen to give an appropriate T_1 and $\dot{\rho}_{01}$. Finally, the unknown value of a_2 is determined for which the two manoeuvre periods are equal, by solving for the roots of the following equation, prior to the trajectory generation:

$$T_1 - T_2(a_2) = 0 \tag{5.17}$$

where $T_2(a_2)$ is found by combining equations (5.12) and (5.13):

$$T_2(a_2) = \frac{1}{a_2} \ln \frac{\dot{\rho}_T}{a_2\rho_{02} + \dot{\rho}_T} \tag{5.18}$$

This solution is determined once, at the beginning of the manoeuvre and ideally, ensures the same manoeuvre time for the two glideslope trajectories. The specified parameters for the two glideslope trajectories,which have been used for simulations in section 5.4 and experiments in Chapter 6 can be found in Table 5–3.

Table 5–3: Glideslope specified parameters

a_1	$\dot{\rho}_{T1} = \dot{\rho}_{T2}$ $(\frac{\text{m}}{\text{s}})$
-0.005	-0.02

5.3.2 Sensing

During the docking stage, the chaser Tryphon relies on various sensors to determine its pose relative to the target. As noted earlier, sensing includes the use of two of the chaser's on-board cameras, which measure the relative position of the corresponding ARtag markers to give $\mathbf{r}_1^B$ and $\mathbf{r}_2^B$ as defined in section 2.1.1, the accelerometer (for roll and pitch) and gyroscope measurements of the onboard IMU, and the compass bearing angle. The orientation of the target Tryphon is known through its independent sensing as described in section 5.2.1; therefore, a relative orientation between chaser and target can be determined. An implementation of the Kalman filter from section 5.2.2 is used to obtain the estimates of $\dot{\mathbf{r}}_1^B$ and $\dot{\mathbf{r}}_2^B$, and to filter all measurements for the output feedback used by the controller. The Kalman filter implementation for docking will be discussed in the next section.

The ROS package "ar_track_alvar", based on the open source ARtag tracking libraries, is used to extract the relative position between the camera and ARtag markers, resolved in the camera's frame (chaser's body-fixed frame). Two sets of three differently ID coded ARtag fiducial markers are placed around the target Tryphon's docking mechanism with known, pre-measured positions with respect to each other, as shown in figure 5–1. The three markers are spread apart to ensure at least one

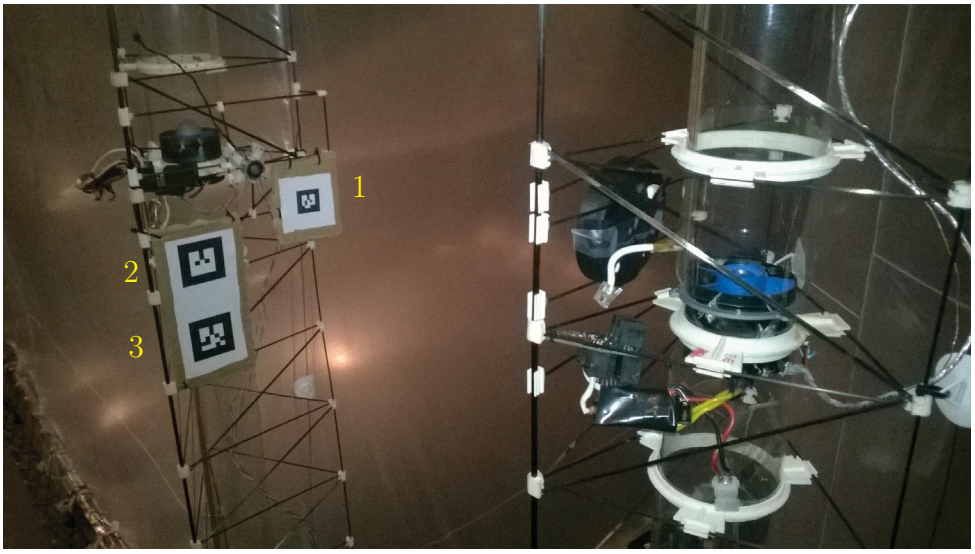

Figure 5–1: ARtag marker set

marker is in camera view if the chaser were to undergo a disturbance or large overshoot was to occur. A priority-based system is implemented, where the highest priority marker ($1 > 2 > 3$) within camera view at any given time, is used to provide the measurements for the Kalman filter. The size of any given marker defines a docking range, where the marker is visible in the camera view and can be tracked. Marker 1 is the smallest marker, and corresponds to the marker which aligns with the chaser's counterpart camera in the docked position, i.e., giving measurements $\mathbf{r}_1^B$ and $\mathbf{r}_2^B$. By making markers 2 and 3 larger, these allow the docking manoeuvre to begin at further distances, when marker 1 would not be visible. The size of marker 1 is specifically chosen to provide relative position measurements near the final docked position, which is when the most accuracy is required. Therefore, the accuracy required for the relative positions between markers, assumed known as noted earlier, is not very high as they are only used to obtain $\mathbf{r}_1^B$ and $\mathbf{r}_2^B$ from the measurements of

markers 2 and 3 during the earlier phase of docking. The "ar_track_alvar" package outputs a relative position and orientation, although the orientation measurements are not sufficiently accurate for docking purposes, and therefore the use of aforementioned independent orientation sensing (with the IMU and compass) is preferred.

5.3.3 Camera/ARtag Measurement Noise Characterization

In order to properly develop the Kalman filter for docking, the measurement noise covariance of each of the individual sensors used had to be properly characterized. As previously mentioned, the measurement noise covariance of the IMU has already been obtained in [1], and the noise variance of the compass has been found to be approximately 0.032 rad, leaving only the characterization of the newly implemented sensing system used for docking: the camera/ARtag marker system. To do so, a separate set of experiments was conducted by mounting the calibrated camera to a Newport positioning system, and measuring the relative position between the stationary camera and ARtag marker using the "ar_track_alvar" ROS package. The experiment was conducted with different distances and orientations between the camera and ARtag marker, as well as under varying lighting conditions. The results of one of the experiments, where the camera is directly facing the ARtag marker (no angle) at a distance of 0.25 m, are presented in figure 5–2. Experiments at multiple different positions (0.10 m to 1.0 m) and orientations (± 0.175 rad) within the range of the docking manoeuvre were also conducted, and an average measurement covariance matrix of selected experiments was calculated between these experimental sets. The resulting covariance values for the coordinates x, y, and z are identical and equal

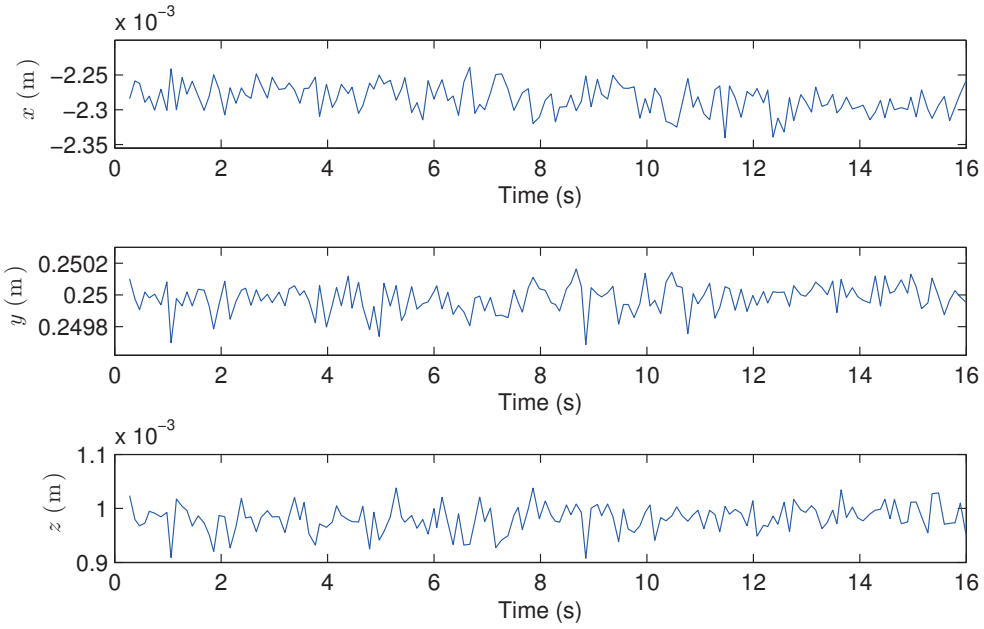

Figure 5–2: Camera/ARtag measurement noise characterization experiment at 25 cm with no angle

to 10^{-8} m, which demonstrate the accuracy of the system and these are used for the Kalman filter.

5.3.4 State Estimation

The discrete Kalman filter presented in section 5.2.2 is also used for the docking stage, which because of its modular design, is easily adapted for the sensing used in this scenario. It is important to note that for docking, the Kalman filter implementation must estimate the output feedback, $\mathbf{y}$, required for the controller, and not the state, $\mathbf{x}$. This is a simple modification, easily accomplished by replacing the state estimates, $\hat{\mathbf{x}}$, with output estimates, $\hat{\mathbf{y}}$, in the presented predict/correct model. For docking, $q = 4$; where the sensors and corresponding values are found in Table 5–4.

Table 5–4: Docking Kalman filter sensor parameters

Sensor # (i)	Sensor	j	Measurements ($\mathbf{z}_k^i$)	Selected for $\hat{\mathbf{y}}$	Frequency (Hz)
1	ARtag 1	3	$[x_1, y_1, z_1]^T$	$x_1, y_1, z_1,$ $\dot{x_1}, \dot{y_1}, \dot{z_1}$	10
2	ARtag 2	3	$[x_2, y_2, z_2]^T$	$x_2, y_2, z_2,$ $\dot{x_2}, \dot{y_2}, \dot{z_2}$	10
3	IMU	5	$[\phi, \theta, \omega_x, \omega_y, \omega_z]^T$	$\phi, \theta, \omega_x, \omega_y, \omega_z$	100
4	Compass	1	$[\psi]$	ψ	10

Next, the Kalman filter is validated using a Monte Carlo simulation to ensure the functionality of the modular design, as well as its proper implementation in C++ and ROS. A docking manoeuvre was generated using the Gazebo simulation, thus giving a set of perfect outputs and measurements. The process then consists of generating 100 corrupted sets of measurements for the given docking manoeuvre, using the noise profile of each sensor. The corrupted measurements are then used with the Kalman filter in real time, to obtain the error covariance values and the estimated outputs. In order to validate the state estimator, the three-sigma (3σ) values are obtained from the error covariance across all 100 sets, and the average at each time step is compared with the corresponding averages of the actual error of the estimates ($\hat{\mathbf{y}} - \mathbf{y}$). Figures 5–3 to 5–6 show the results of the Monte Carlo validation, where each figure presents the individual sensors used for docking, i.e., the first camera/ARtag pair, the second camera/ARtag pair, the IMU and the compass respectively. It is clear from these results that the Kalman filter is correctly estimating the outputs required for the controller.

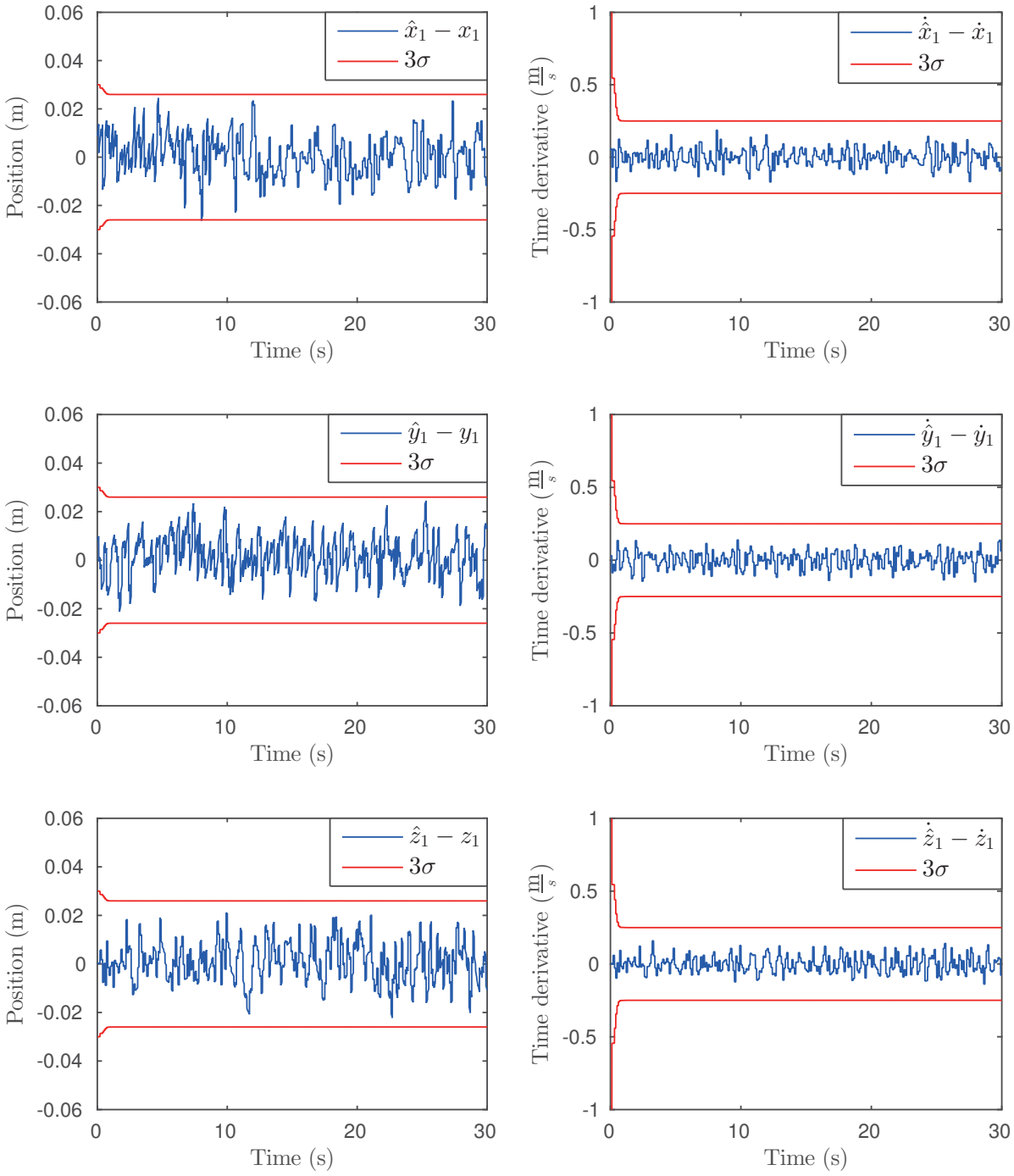

Figure 5–3: Validation of estimates using first camera/ARtag pair ($\mathbf{r}_1^B$, $\dot{\mathbf{r}}_1^B$)

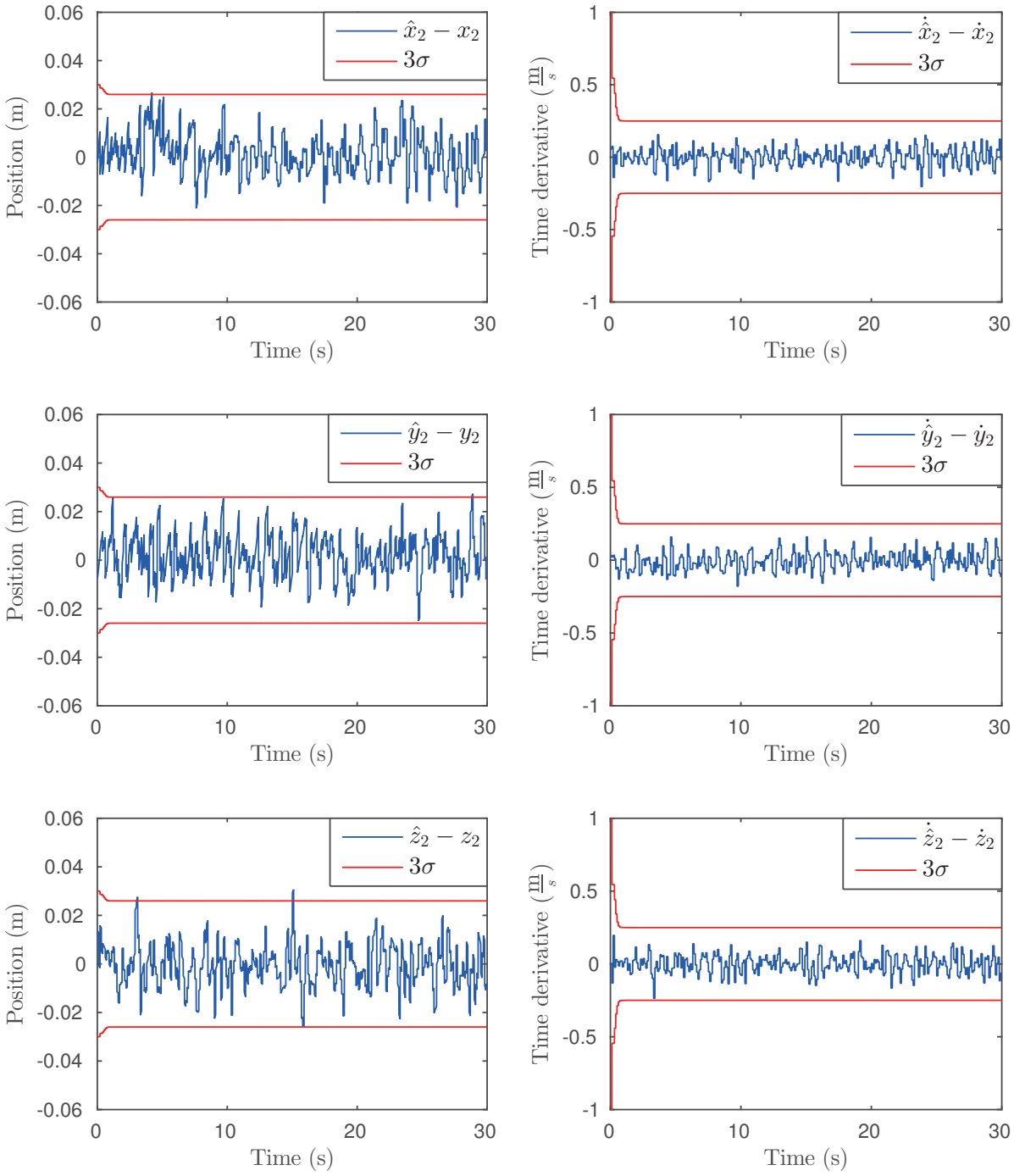

Figure 5–4: Validation of estimates using second camera/ARtag pair ($\mathbf{r}_2^B$, $\dot{\mathbf{r}}_2^B$)

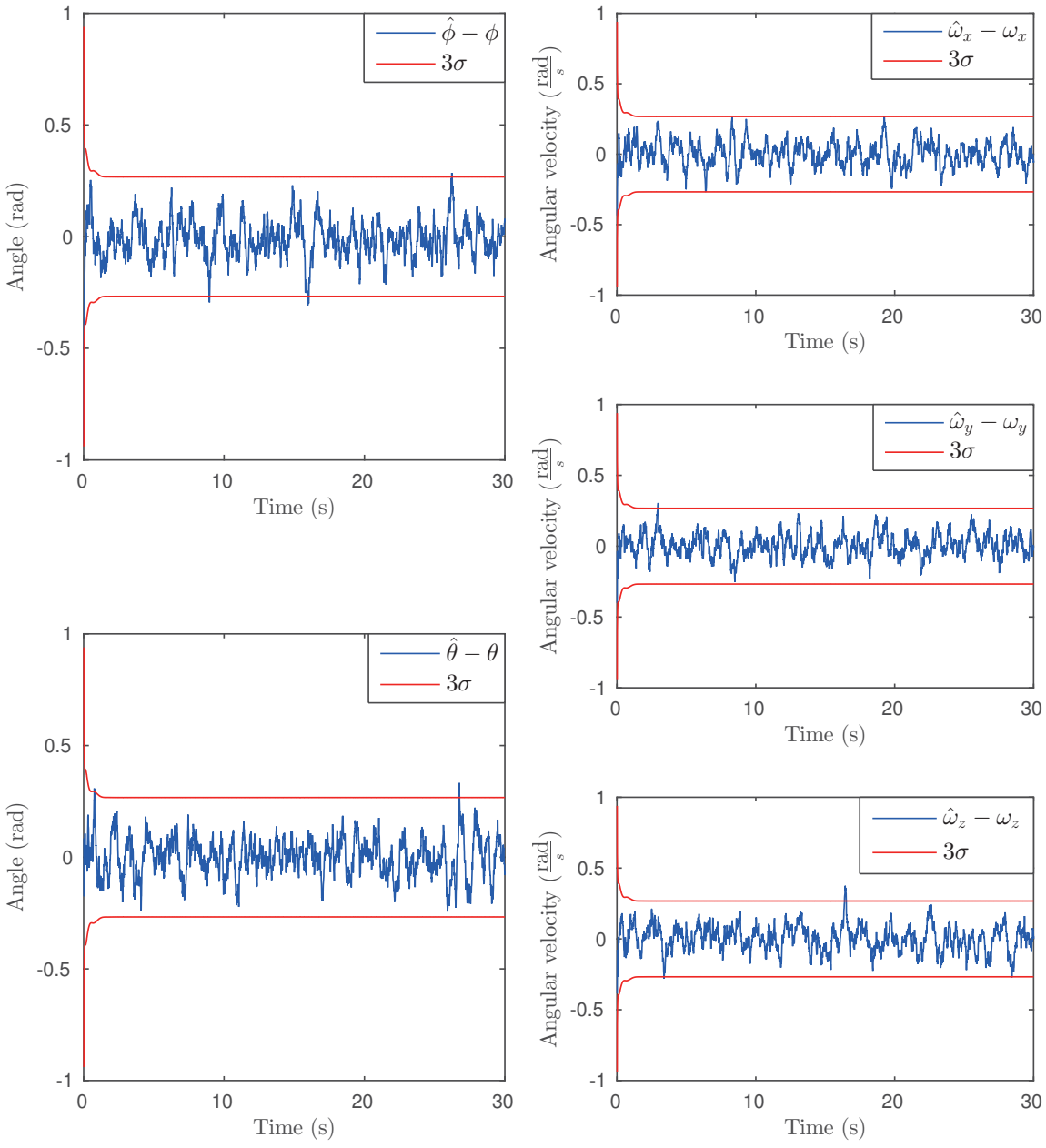

Figure 5–5: Validation of estimates using IMU (ϕ, θ, $\boldsymbol{\omega}$)

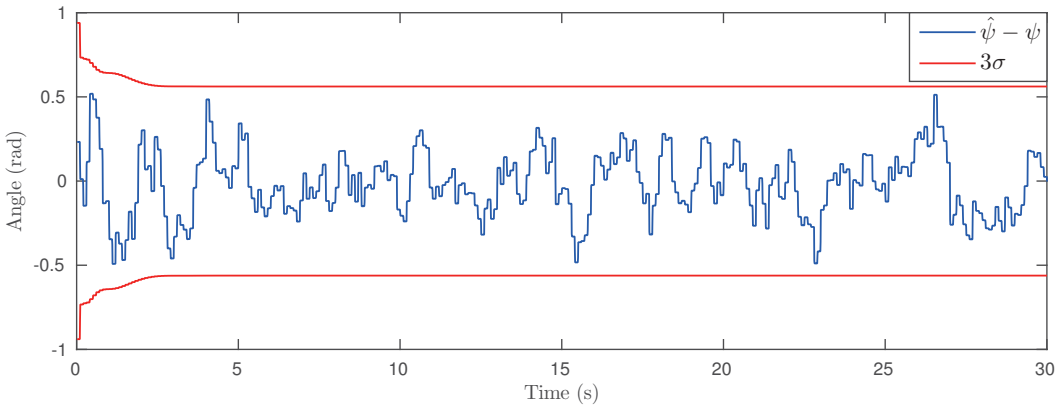

Figure 5–6: Validation of estimate using compass (ψ)

5.4 Rendezvous and Docking Simulation

Using the GNC systems discussed in this Chapter, the entire rendezvous and docking manoeuvre has been simulated using the high fidelity Gazebo model. Figure 5–7 demonstrates three different steps of the manoeuvre to give a visual representation of the simulation. As desired, the rendezvous stage brings the two Tryphons close together to the pre-dock position using the GNC system of section 5.2, and once both airships have stabilized the docking stage begins. During the docking stage, the target remains stationary using the same GNC system as for rendezvous, and the chaser switches to the GNC system of section 5.3. The approximate initial conditions for rendezvous and for docking for both chaser and target are found in Table 5–5, with roll, pitch and velocities approximately at zero. No exact initial conditions can be given considering that at the beginning of both stages the Tryphons are regulating under closed-loop control. Note the yaw values presented in Table 5–5 are given by MCPTAM, and represent the yaw angle with respect to the inertial frame located on the saved map. During docking, since the GNC system changes, the chaser uses the

orientation with respect to the inertial frame with origin at the fixed target's center of mass. The angles which are presented in future figures for the docking stage are those used for relative control of the chaser, and are referred to as relative angles.[1]

Table 5–5: Initial conditions for rendezvous and docking Stage

	Global Position (X, Y, Z)	Relative Position (x_1, y_1, z_1) (x_2, y_2, z_2)	Yaw (MCPTAM)
Rendezvous			
chaser	$(0.71, 0.23, 1.43)$	N/A	$65.6°$
target	$(-3.58, -5.01, 1.51)$	N/A	$-55.9°$
Docking			
chaser	$(0.5, 1.9, 1.75)$	$(0.030, 1.393, 0.038)$ $(0.033, 1.510, 0.040)$	$107.7°$
target	$(3.0, -3.0, 1.75)$	N/A	$-72.3°$

The results of the simulation are presented in figures 5–8 to 5–10. Figure 5–8 shows the relative roll, pitch and yaw angles of the chaser with respect to the target, and figure 5–9 shows the translational positions of the chaser and target in the inertial frame (with MCPTAM origin). The moment of transition between the rendezvous stage and the docking stage is marked by the vertical, black dotted line. The positions of the center of mass of each Tryphon in inertial space do not clearly infer a successful docking, but do provide an illustration of their movements. Figure 5–10 presents the perfect measurements of $\mathbf{r}_1^B$ and $\mathbf{r}_2^B$, and the corresponding glideslope trajectories being tracked. In this figure, the transition clearly occurs when

[1] Due to symmetry in the Gazebo model, a chaser relative yaw of zero corresponds to a π difference in the MCPTAM measurement of the chaser and target yaw

the glideslope trajectory begins. As stated in Chapter 3, the Gazebo model does not simulate the electro-magnet and metallic plate contact, thus nothing noticeable from docking appears in the simulation results. Nevertheless, the lateral errors all fall within the 4.25 cm threshold where the electro-magnet finds itself within the receiver cone, demonstrating a successful dock. Furthermore, the output feedback control is able to track the glideslope trajectory quite well, and docking at both contact points occurs simultaneously as desired.

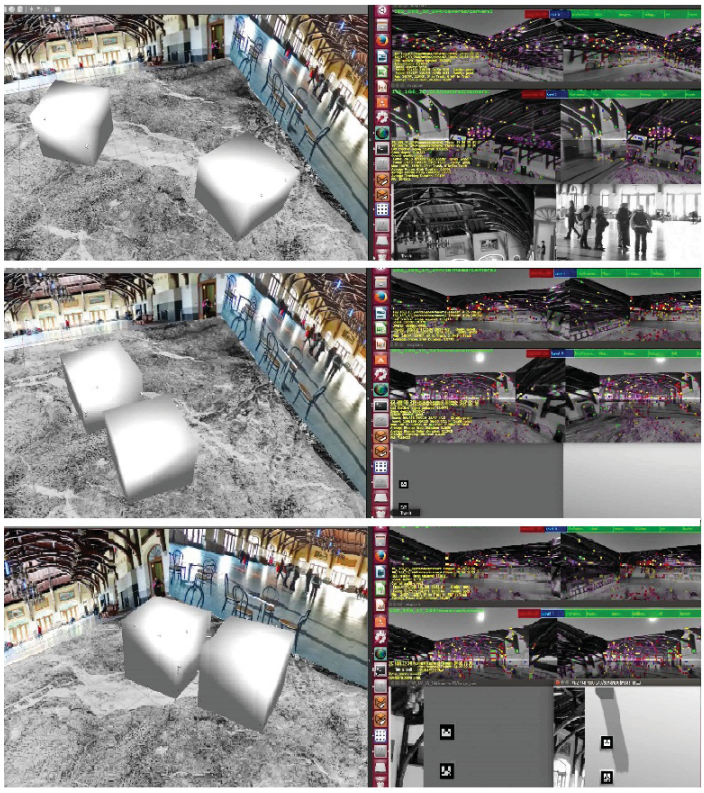

Figure 5–7: Different steps representative of the rendezvous and docking simulation

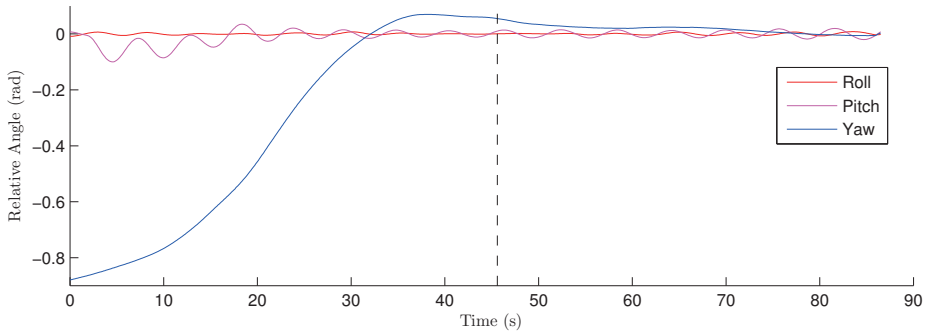

Figure 5–8: Chaser relative angular results of simulation

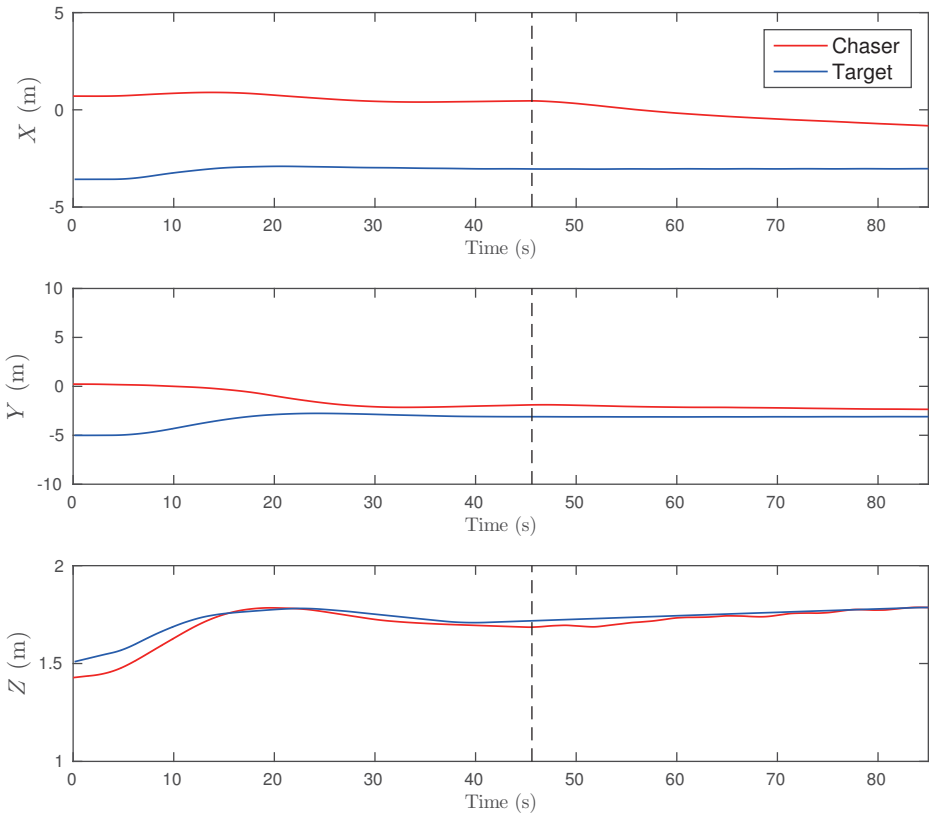

Figure 5–9: Translational results of simulation in inertial frame

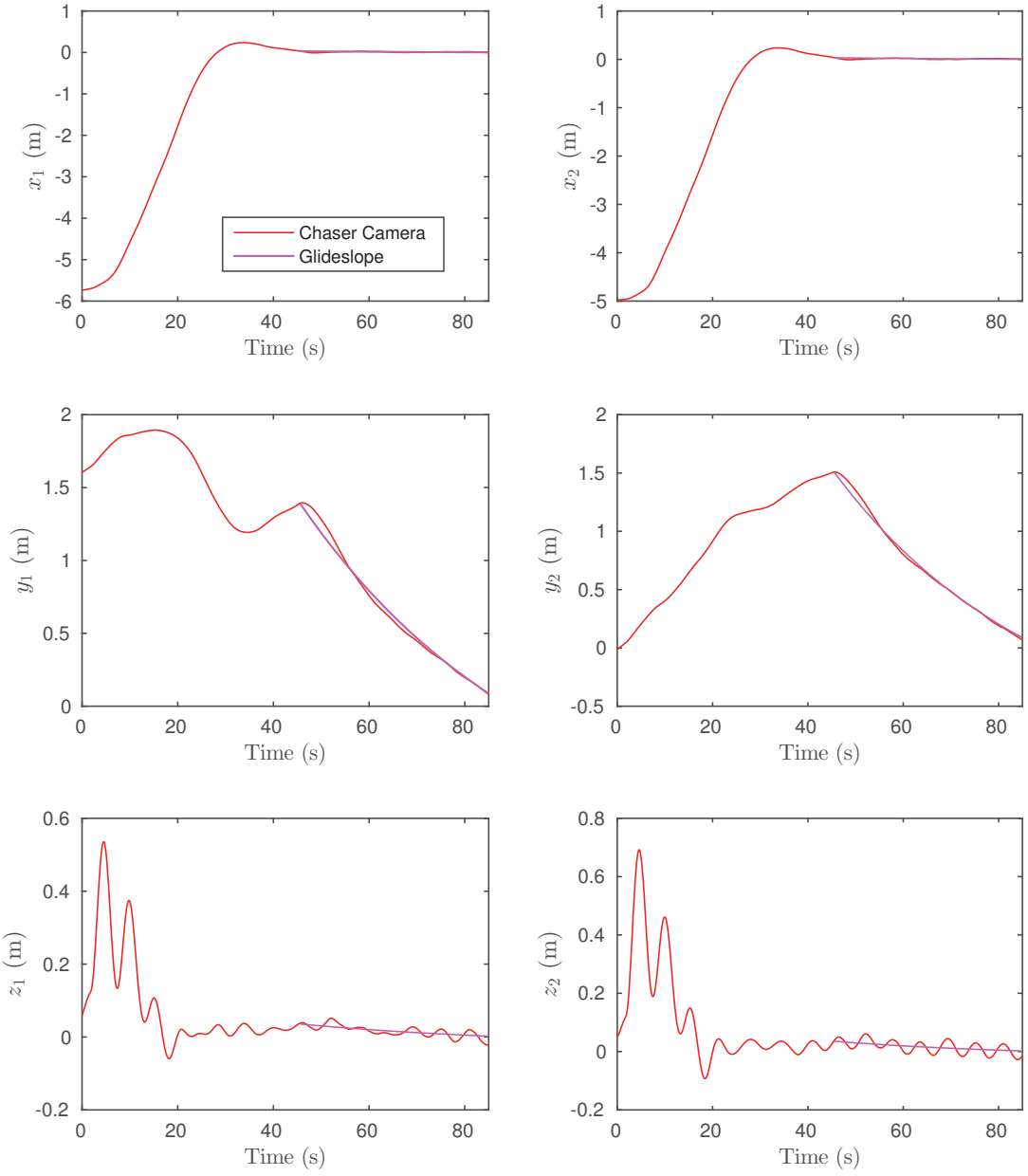

Figure 5–10: Translational results of simulation in chaser body-fixed frame (vectors $\mathbf{r}_1^B$ and $\mathbf{r}_2^B$)

CHAPTER 6
Docking Experiments

The developed guidance, navigation and control systems have been implemented in real time on a chaser Tryphon for docking with a fixed target, i.e., a target fastened on top of a table. Two sets of experiments were carried out at two locations: a first set was conducted at UQAM's Studio-théâtre Alfred Laliberté and a second set of experiments was conducted at UQAM's Coeur des sciences Agora, both of which are located in Montreal. The Tryphon set up in a part of the UQAM Agora can be seen in figure 6–1. These experiments resulted in successful docking with contact of both ends of the docking mechanism, under disturbances corresponding to local drafts present in the corresponding spaces. Figure 6–2 shows a close-up of the two Tryphons in their docked state.

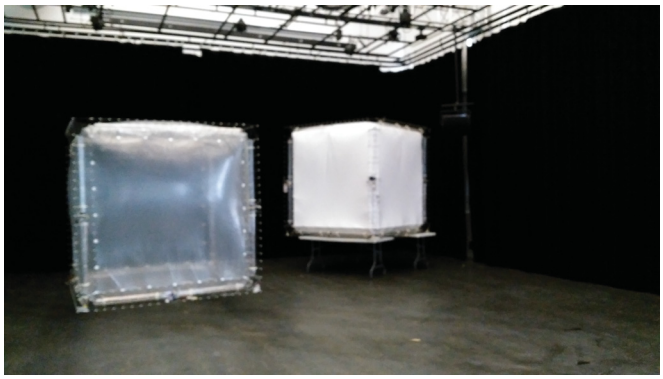

Figure 6–1: Tryphon set-up at UQAM's Coeur des sciences Agora

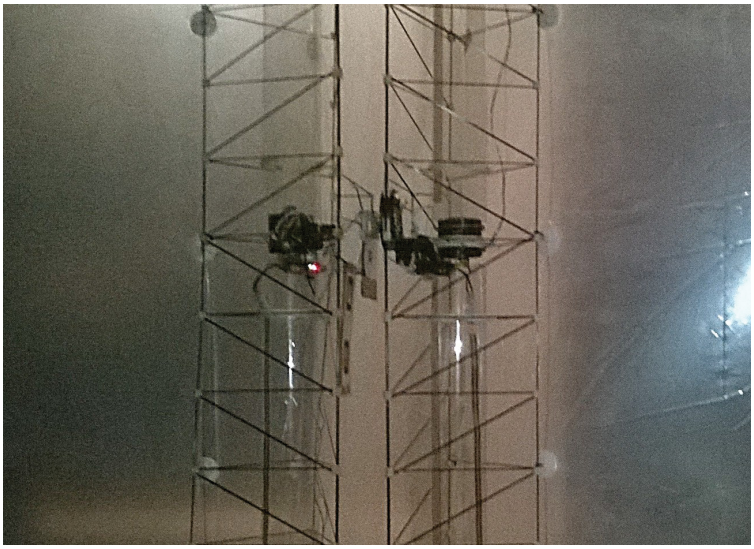

Figure 6–2: Target(left) and chaser(right) Tryphon in docked position with docking mechanism contact at UQAM's Studio-théâtre Alfred Laliberté

6.1 Experimental Setup

For these experiments, the docking mechanisms on the fixed target Tryphon have ARtag sets consisting of three markers, with the same pattern as seen in figure 5–1 of section 5.3.2. Markers 2 and 3 have a horizontal distance from marker 1 of 12.5 cm and a vertical distance of 8 cm and 17 cm respectively. Marker 1 has a side length of 1.5 cm, and markers 2 and 3 are of size 4 cm to ensure at least one ARtag marker is within visible range during the entire docking manoeuvre. This marker size combination can be tracked from distances up to 1.5 meters away, to allow regulation of the chaser in front of the target, and as close as needed for docking (6-8 cm distance between camera and marker when docked). Figure 6–3 shows the camera views at 3 different points of the docking stage for a better understanding of the purpose of multiple, differently sized markers.

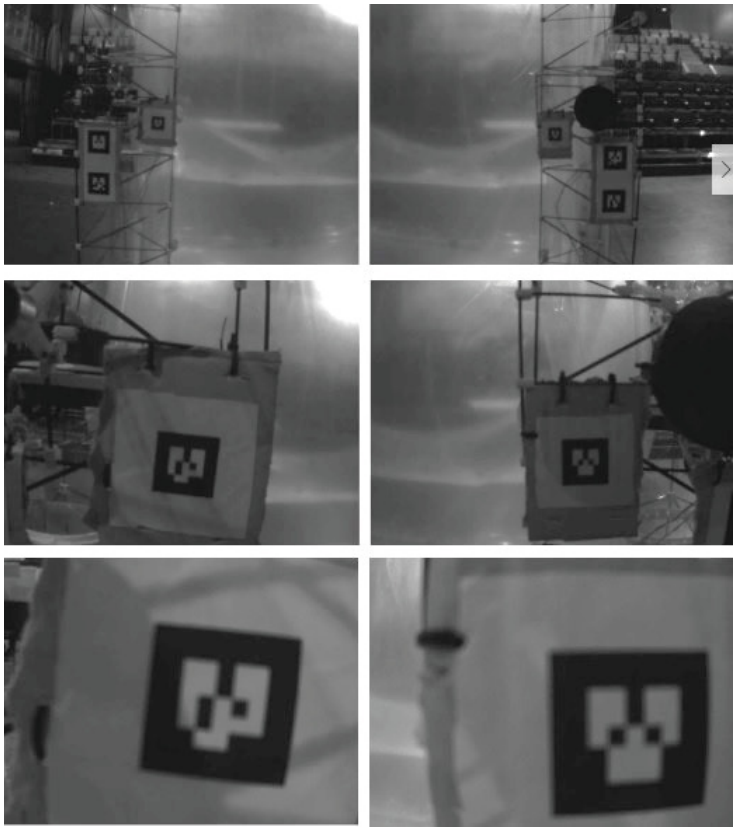

Figure 6–3: Chaser camera views (left and right) at three different steps of the docking approach

On the chaser, the two cameras are placed within each of the docking mechanisms located on the positive y-axis face of the cube (the docking direction), and are plugged into separate Gumstix boards to provide the maximum frame rate possible for each camera (10 fps). One Gumstix is placed in its normal location on one of the lower trusses near a motor (figure 1–3), and another Gumstix board is placed on the upper truss on the opposite side of the cube with a compass, to maintain the weight distribution symmetric and have the sensors (IMU and compass) far away

from any motors for reduced interference and more reliable measurements. Furthermore, weights have been placed on the Tryphon to provide close to neutral buoyancy and ensure the center of mass has a small offset in the negative y-axis of the chaser frame, following the findings of section 4.3. The electro-magnets located in the docking mechanism were employed for actual docking for the first set of experiments; however, due to technical difficulties, they were replaced with permanent magnets for the second set of tests.

6.2 Experiments Set 1: Studio-théâtre Alfred Laliberté

For this residency, several experiments were required to tune the gains of the output feedback controller, which had only been tuned in simulation beforehand, combined with the knowledge gained from regulation experiments presented in Chapter 4. In the end, the gyroscope measurements of the IMU were found to be too noisy and degraded the performance of orientation control; therefore, the gains assigned to angular velocity errors in the gain matrix $\mathbf{K}$ were set to zero, resulting in the gain matrix and closed-loop poles given in Appendix A as equations (A.1) and (A.2).

It is clear that after tuning, the system is no longer critically damped as desired. This is still acceptable due to the robustness of the docking mechanism design which does indeed allow for some overshoot. Furthermore, the local drafts in the room were strong and erratic, and caused a severe impact on the performance of the chaser Tryphon. Integral terms were added in the x and y control, combined with the already included z term, to help alleviate the effects of these disturbances. The final form of the controller (equations (A.3) to (A.6)) and its block diagram (figure A–1) can also be found in Appendix A, along with the closed-loop poles (equation (A.7)).

This set of experiments was a first attempt at the docking of the chaser and target Tryphon using the implemented GNC system, with the purpose of determining the effectiveness, and observing the performance of the system.

6.2.1 Experimental Procedure

Initial testing demonstrated that the expected pre-dock distances from simulations were too ambitious, and had to be reduced. The first set of experiments begins with regulation of the chaser at a specified distance of approximately 0.75 meters from the fixed target. The chaser is then commanded to move to a closer distance in small intervals, ranging between 0.05 and 0.1 meters. Once the chaser is stable with low oscillations after the commands of the previous statement (at distances between 0.4 and 0.5 m), similar to the outcome of completing the rendezvous stage, the docking stage begins where the glideslope algorithm generates the desired trajectory which the output feedback controller tracks directly to the final docked position. It is during this stage that the electromagnet is activated, so contact with the metallic plate results in a successful dock. For this residency, twelve docking experiments were conducted and recorded with the tuned controller and added integral terms.

Out of the twelve experiments conducted at UQAM's Studio-théâtre Alfred Laliberté, the chaser successfully docked to the target 6 times, with a few failures caused by the I2C signal not properly being sent to the electro-magnet relay device, and the others from either loss of vision of the ARTags or docking misses. The estimated position of the two electro-magnets in the xz-plane for the 6 successful docks are presented in figure 6–4, with the black circle representing the outer perimeter of the cone-shaped receiver. The average docking time over the successfully docked

experiments was approximately 21.6 seconds, while that of the glideslope trajectory was close to 17 seconds. The electro-magnets occasionally had difficulty coming into contact with the metallic plate located in the receiver cone, therefore adding several seconds to the docking completion time. If the metallic plates were larger, it would have resulted in quicker contact once the electro-magnet entered the receiver cone.

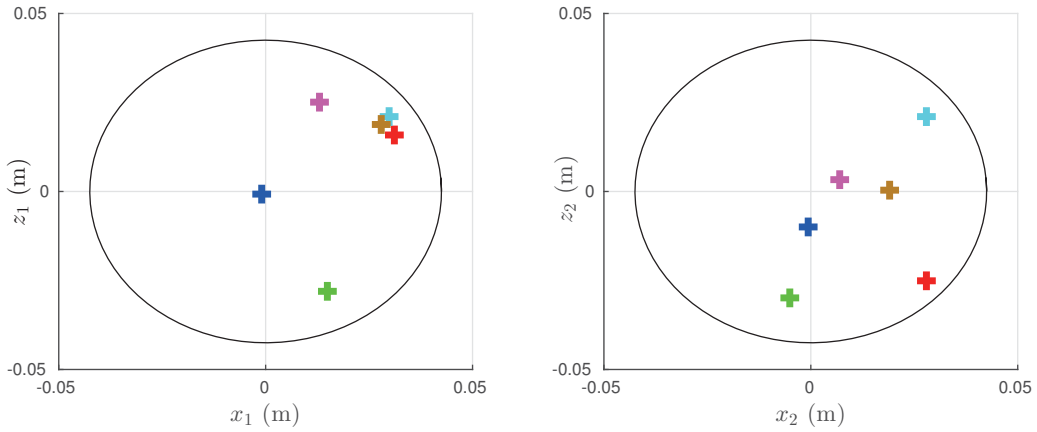

Figure 6–4: xz-plane position of electro-magnets corresponding to measurements $\mathbf{r}_1^B$ and $\mathbf{r}_2^B$, at docked position for first set of experiments

The responses from one successful experiment (blue markers in figure 6–4) are presented in figures 6–5 to 6–7. Figure 6–5 plots the vector components of the outputs $\mathbf{r}_1^B$ and $\mathbf{r}_2^B$ with their desired values given by the glideslope algorithm, along with the error between them. Figure 6–6 shows the magnitudes of the time derivatives $\dot{\mathbf{r}}_1^B$ and $\dot{\mathbf{r}}_2^B$, with the desired magnitudes of $\dot{\boldsymbol{\rho}}_1^B(t)$ and $\dot{\boldsymbol{\rho}}_2^B(t)$, and errors respectively. The orientation of the chaser Tryphon during the docking run is presented in figure 6–7 and the motor commands are presented in figure 6–8, which are labelled based on figure 2–3. The results presented in figure 6–5 clearly demonstrate the ability of the output feedback controller to track the glideslope guidance algorithm and dock,

bringing the electro-magnets within the area of the receiver cone, as demonstrated by all error terms being below 4.25 cm (and blue marker in figure 6–4). The apparent translational oscillations during the experiment are reasonably small, and are not only present due to translational motion of Tryphon, but are consequences of the orientation changes, which affect the camera position and body-fixed frame vector components.

As previously mentioned, a benefit of the glideslope guidance algorithm is its specification on the approach velocity, which provides the choice of a final arrival velocity for soft docking, and for enough momentum for the electro-magnets to slide along the receiver cones. Figure 6–6 shows that the controller can reasonably track the desired velocity given by the glideslope algorithm. Overall, the performance of the guidance, navigation and control system combined with the robustness of the docking mechanism design allows the chaser to successfully dock to a fixed target.

6.3 Experiments Set 2: Coeur des Sciences Agora

Using the knowledge and controller gain tuning from the first set of docking experiments during the Studio-théâtre Alfred Laliberté residency, the output feedback controller was further tuned for the experiments at the Coeur des science Agora, and the final gain matrix can be found in Appendix A, equation (A.8), along with the corresponding closed-loop poles (equation (A.9)). The size of the metallic plates located on the receiver docking mechanism were increased for these experiments, following the conclusions of the previous set. The purpose of this set of experiments was to determine the efficiency and success rate of the implemented GNC system for docking.

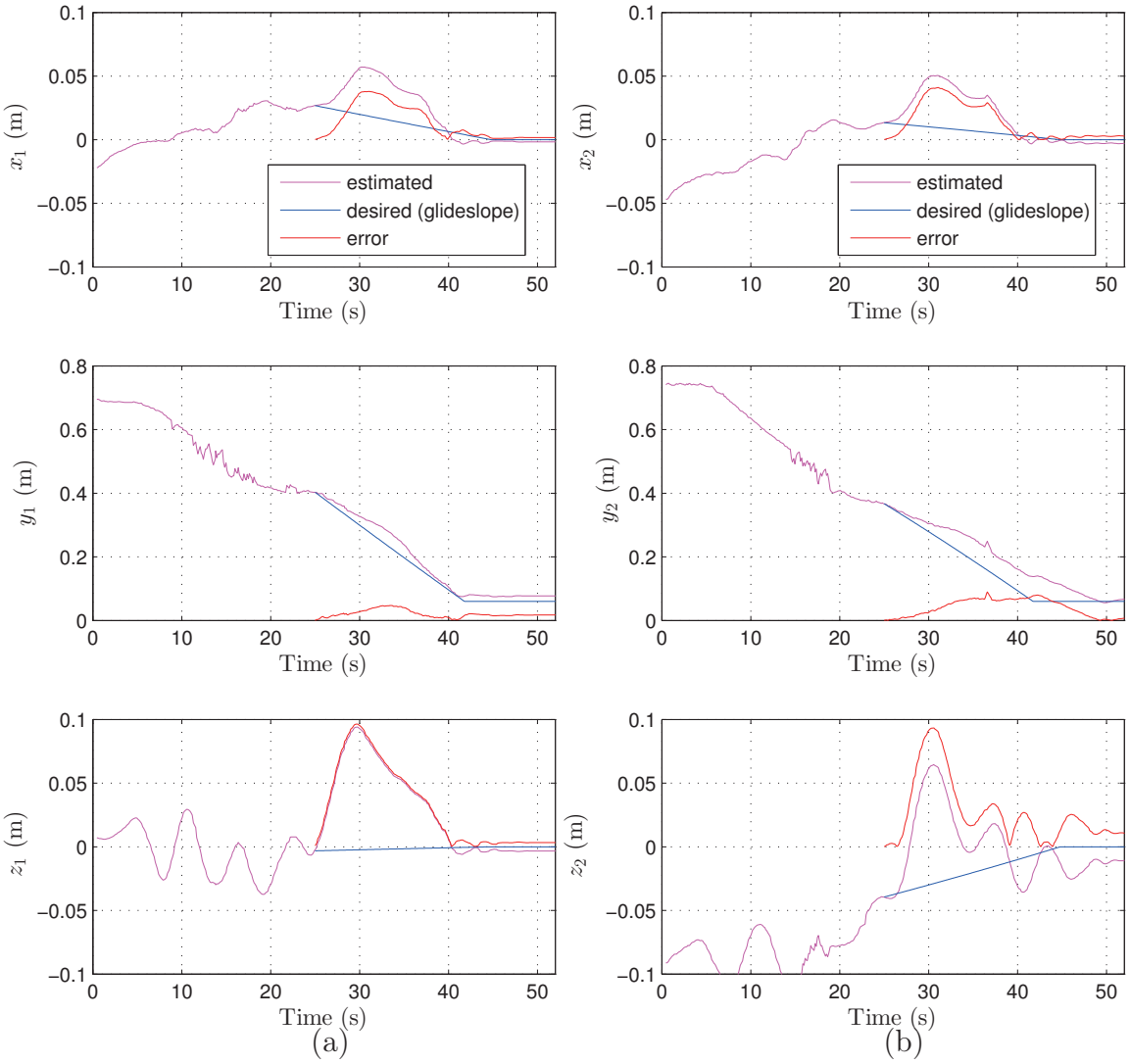

Figure 6–5: Experimental results showing estimated, desired and error vector components of (a) $\mathbf{r}_1^B$ and (b) $\mathbf{r}_2^B$ for first set of experiments

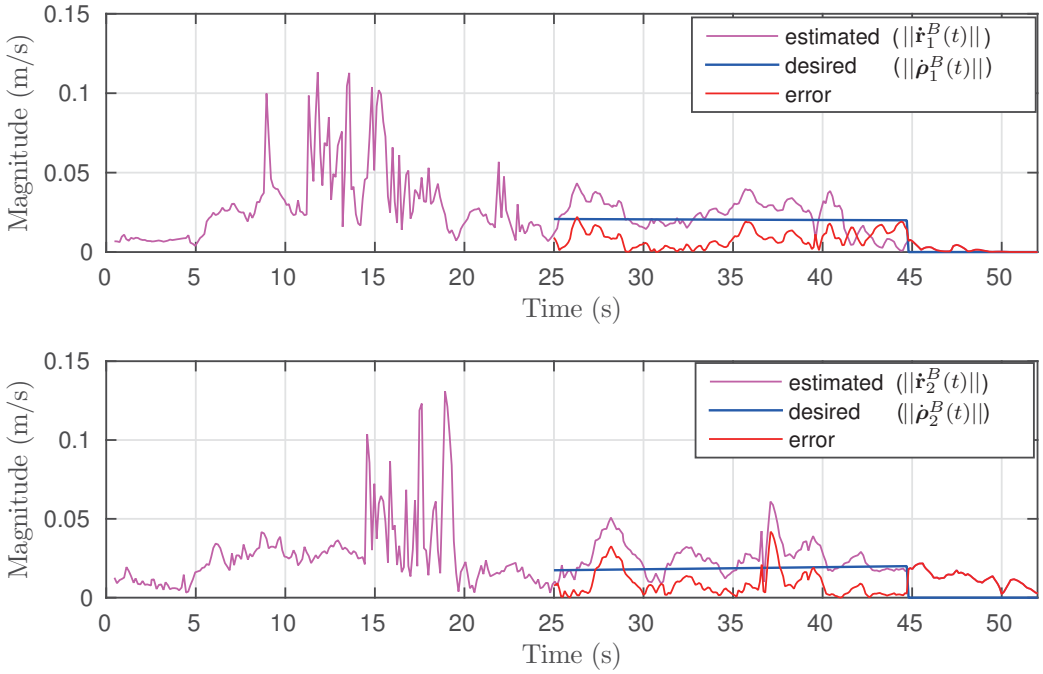

Figure 6–6: Experimental results showing magnitudes of the estimated, desired and error values of $\dot{\mathbf{r}}_1^B$ and $\dot{\mathbf{r}}_2^B$ for first set of experiments

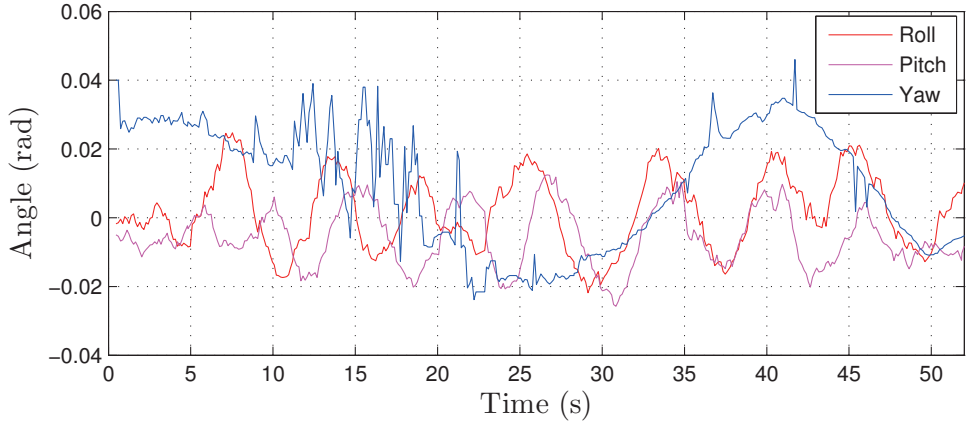

Figure 6–7: Experimental results showing orientation of chaser Tryphon for first set of experiments

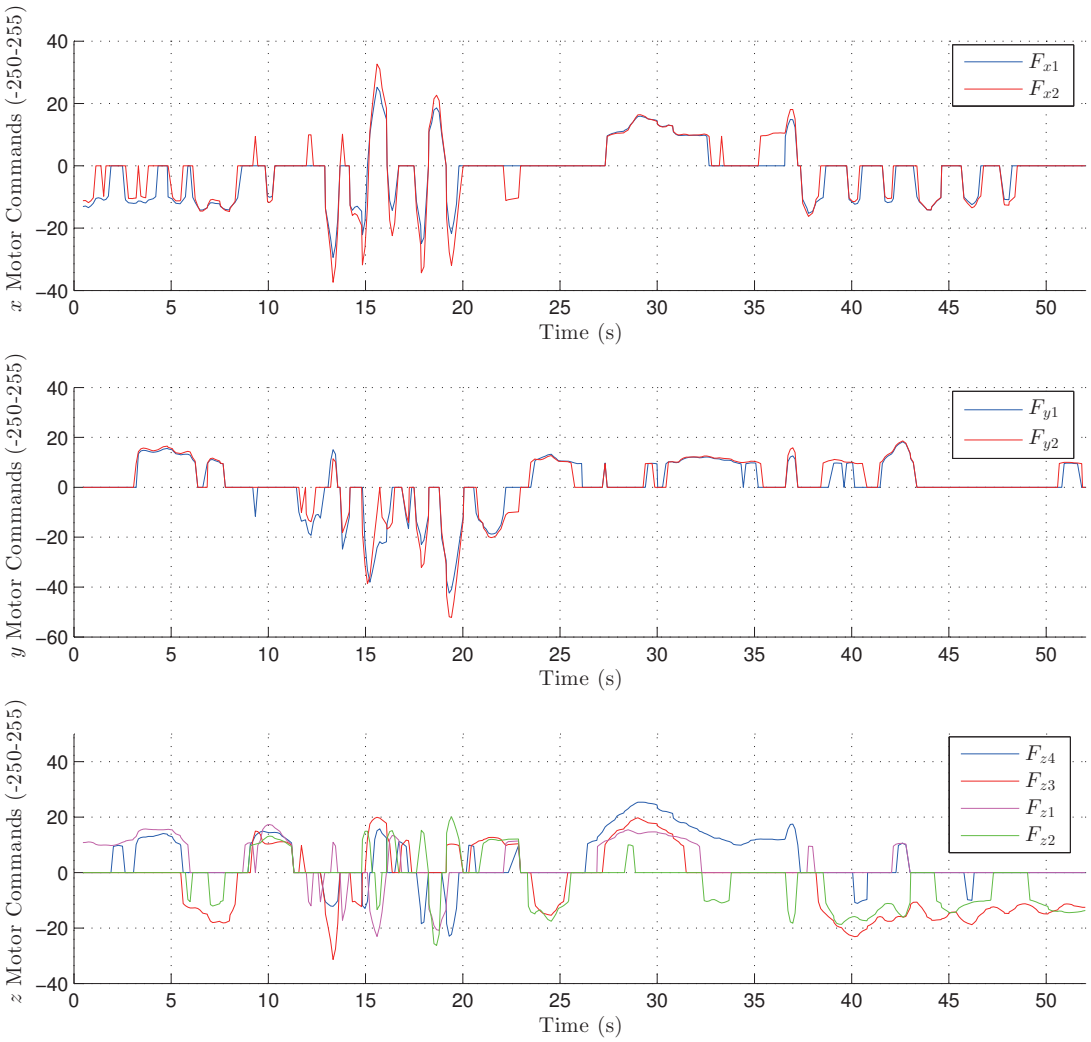

Figure 6–8: Experimental results showing motor commands of chaser Tryphon for first set of experiments

6.3.1 Experimental Procedure

For this set of experiments, the chaser Tryphon begins by regulating at a position approximately 0.475 meters away from the target cube, having similar initial

conditions with the first set of experiments. Once the chaser is reasonably stable, it is commanded to dock to the target using the generated glideslope trajectories. In order to determine the success rate of the implemented GNC system, forty tests were conducted while maintaining approximately the same initial conditions.

The results of the experiments were very promising, with thirty-three successfully completed docks and seven failures. Of these successes, thirty demonstrated full tracking of the ARtag markers during the entire manoeuvre. These include the experiments where one magnet initially misses the metallic plate, but lands within the receiver cone and slowly makes its way to the metallic plate, sometimes adding an extra ten to twenty seconds to the manoeuvre. During three of the successful experiments, there was a loss of vision of the markers resulting in a docking miss, but the chaser recovered after a rebound, seeing the markers once again and managing to dock. These three experiments are considered successful, but are not included in the results presented later. Seven failures occurred; in three of these, it is clear that the GNC system was not successful in docking, and four of the failed experiments were caused by external factors. One of these four failed experiments has a moment where the image feedback of both cameras froze, causing the system to perform poorly, and for the three other experiments, the chaser suddenly drifted away, most likely due to a strong draft.

In the thirty successful experiments with full ARtag tracking during docking, the experimental responses are repeatable and overall performance is similar. The average time for the generated glideslope trajectory was 20.8 seconds, with the average time observed for docking at 26.3 seconds. This average docking time was

greater than the average glideslope time due to the additional time taken for the protruder magnet to reach the metallic plate within the receiver cone, when contact did not occur immediately. The estimated position of the magnets in the xz-plane for the thirty successful docks are found in figure 6–9. The average lateral misalignment distances across the thirty experiments corresponding to $\mathbf{r}_1^B$ and $\mathbf{r}_2^B$ are given in table 6–1. These errors are all below 1.5 cm, demonstrating the accuracy of the GNC system, and its ability to bring the magnets within the 4.25 cm radius of the receiver cone.

Table 6–1: Average lateral misalignments across experiments (m)

x_1	z_1	x_2	z_2
0.0147	0.0093	0.0109	0.0094

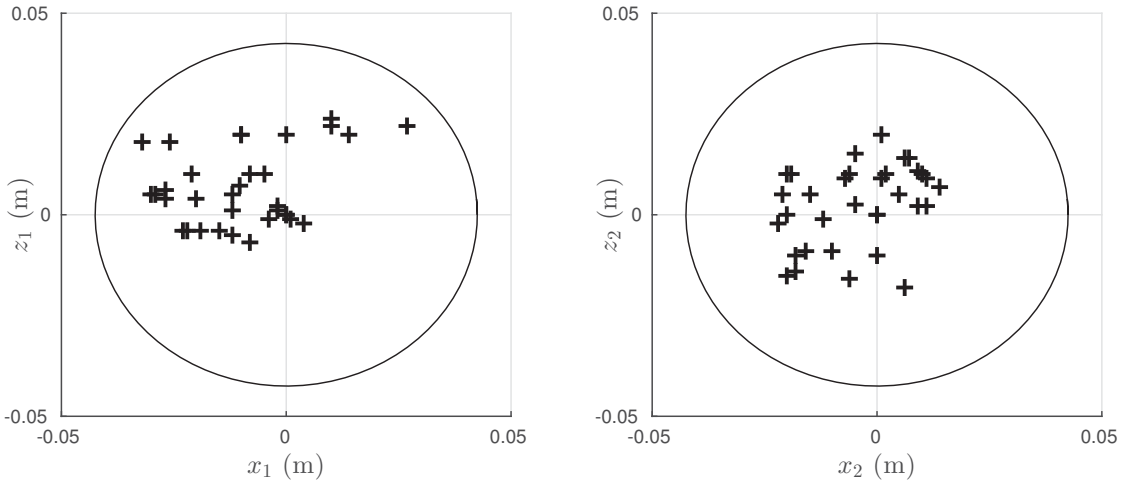

Figure 6–9: xz-plane position of electro-magnets corresponding to measurements $\mathbf{r}_1^B$ and $\mathbf{r}_2^B$, at docked position for second set of experiments

The results of a successful experiment from the second set are presented in figures 6–10 to 6–12. Once again, figure 6–10 plots the vector components of the outputs $\mathbf{r}_1^B$ and $\mathbf{r}_2^B$ with their desired values given by the glideslope algorithm, along with the error between them. Figure 6–11 shows the magnitudes of the time derivatives $\dot{\mathbf{r}}_1^B$ and $\dot{\mathbf{r}}_2^B$, with the desired magnitudes of $\dot{\boldsymbol{\rho}}_1^B(t)$ and $\dot{\boldsymbol{\rho}}_2^B(t)$, and errors respectively. The orientation of the chaser Tryphon during the docking manoeuvre is presented in figure 6–12, and the motor commands are presented in figure 6–13. The axes scales found in figure 6–10 are the same as those in figure 6–5, and the performance is very similar between both sets. The noise found in the early stages of the docking manoeuvre is caused by the camera losing track of marker 1 and switching to marker 2. This was seen in the previous set of experiments as well, but not as prominently, and is believed to be caused by a combination of expected marker misalignments, and less accurate calibration of the cameras in the second set.

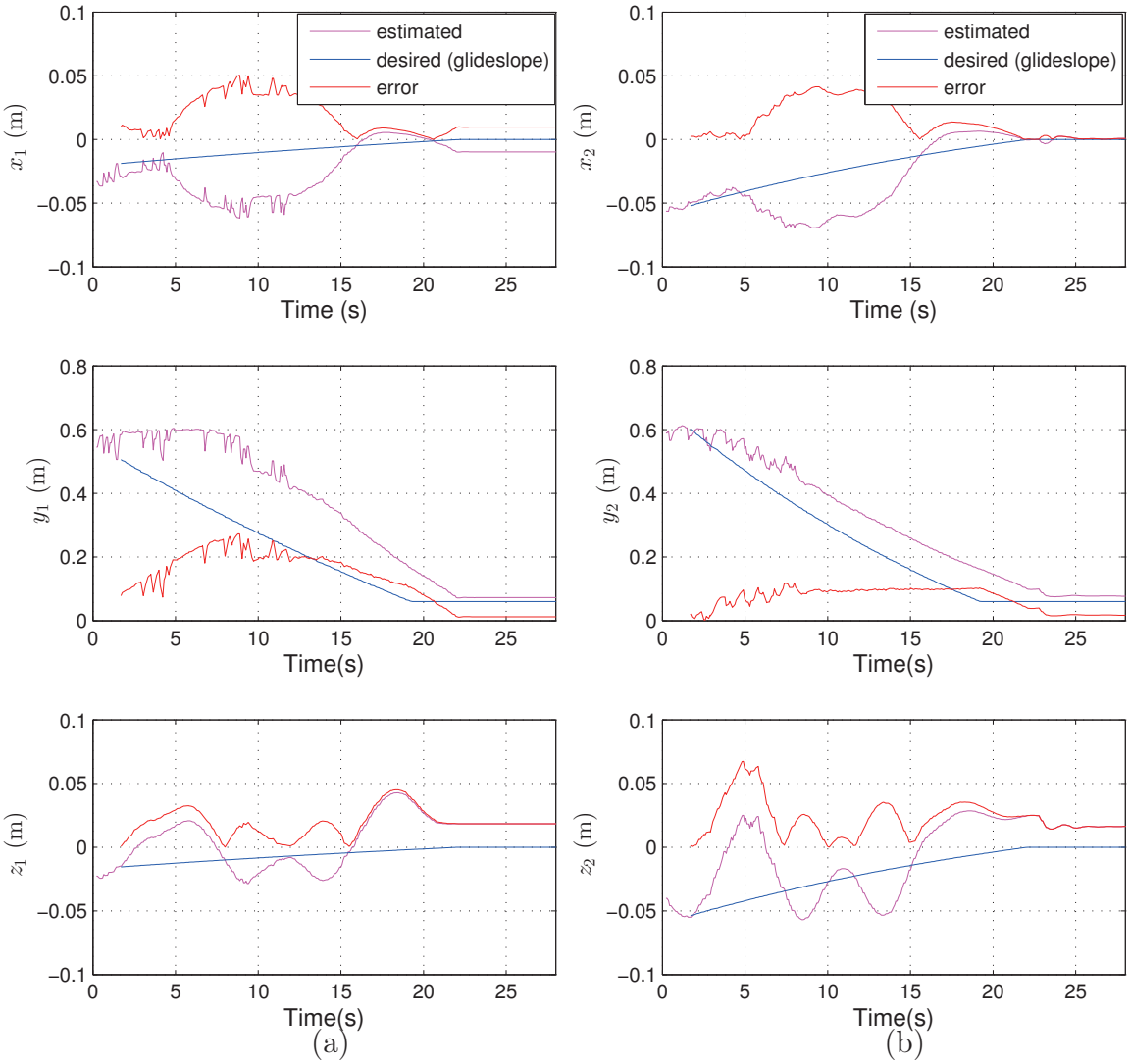

Figure 6–10: Experimental results showing estimated, desired and error vector components of (a) $\mathbf{r}_1^B$ and (b) $\mathbf{r}_2^B$ for second set of experiments

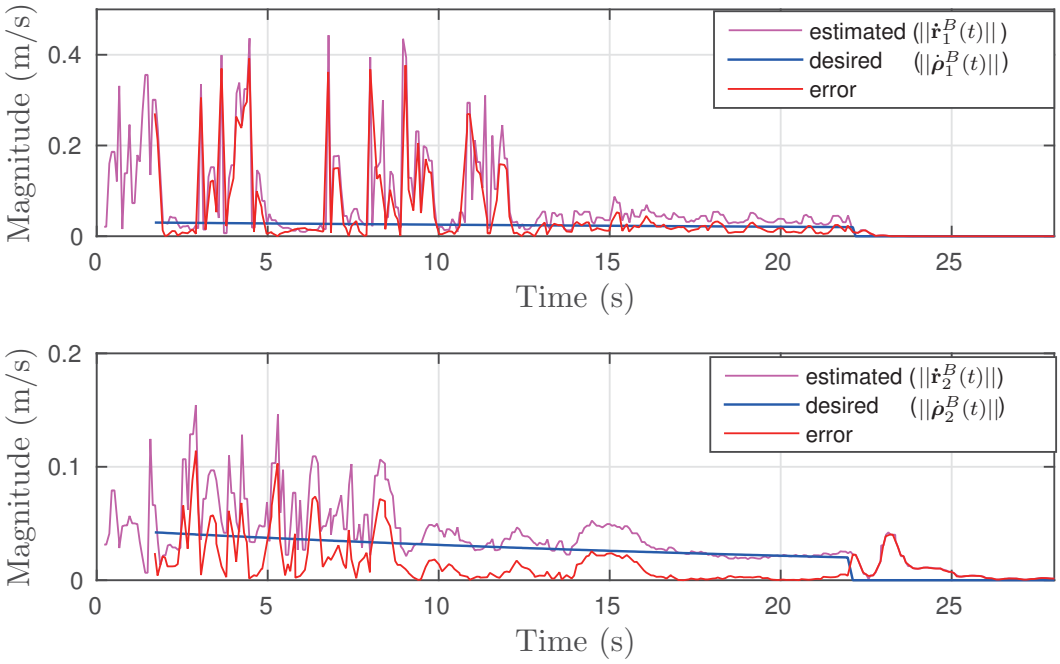

Figure 6–11: Experimental results showing magnitudes of the estimated, desired and error values of $\dot{\mathbf{r}}_1^B$ and $\dot{\mathbf{r}}_2^B$ for second set of experiments

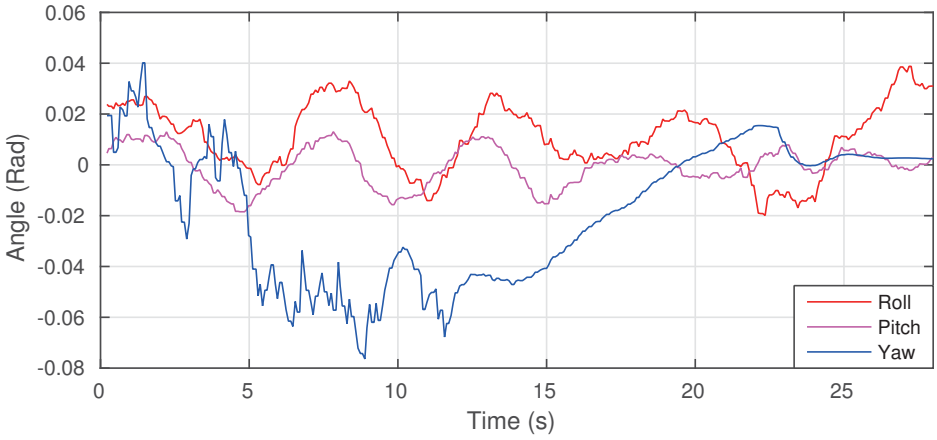

Figure 6–12: Experimental results showing orientation of chaser Tryphon for second set of experiments

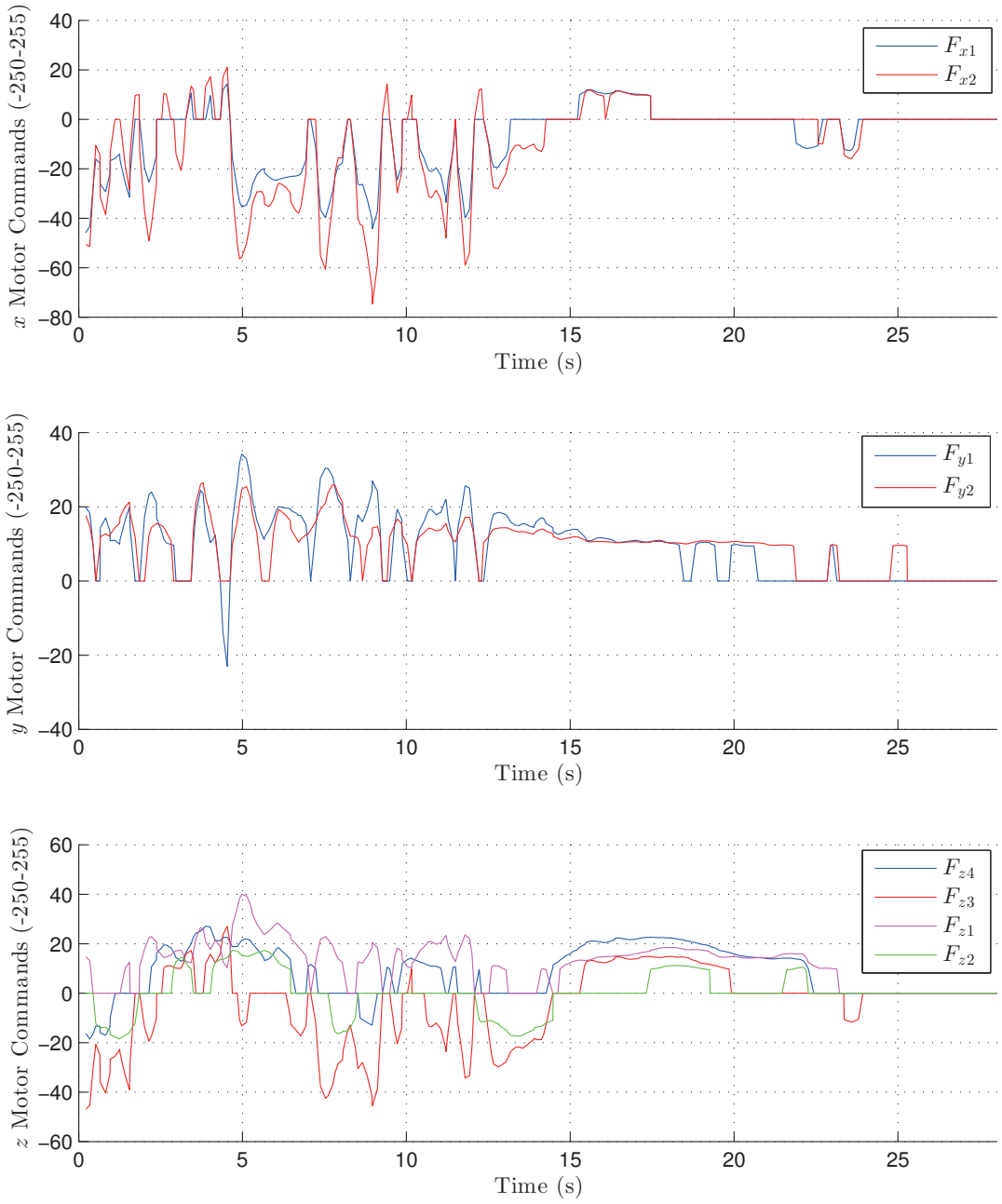

Figure 6–13: Experimental results showing motor commands of chaser Tryphon for second set of experiments

CHAPTER 7
Conclusions

The focus of this thesis was the rendezvous and docking between chaser and target cubic airships, for the ultimate goal of autonomous assembly of floating structures in artistic performances. This chapter summarizes the contributions made towards this goal, followed by possible improvements and recommendations in future work for the Tryphon project.

In order to achieve successful docking, strategies were chosen based on the Tryphon system's characteristics and limitations. The entire manoeuvre was broken down into two stages, the rendezvous stage and the docking stage, each of which involved different approaches and GNC systems. The docking stage requires the most precision and robustness to ensure successful contact occurs at the two ends of the presented docking mechanism. An analysis of the performance of different levels of cooperation between the chaser and target resulted in the decision to control both Tryphons during rendezvous using a global localization system, bringing them to the pre-dock position, and then switching to relative localization on the chaser for docking, where the target then remains stationary at the desired pose.

The Tryphon platform was presented with the docking mechanism and hardware found on the vehicle. A dynamics model of a planar case was developed to determine the feasibility of using an output feedback controller with two relative position measurements. Based on the previous work, a 6 DOF dynamics model of Tryphon

was presented and a state-space model was developed for the docking scenario with a fixed target. Past achievements with Tryphon regulation permitted this assumption, where the performance of a stationary target under closed loop control was considered sufficient. The model has been implemented in both Simulink/SimMechanics and Gazebo simulation software, with the former being simpler and more user-friendly for algorithm development and the latter being a high-fidelity model used to prepare for experimental campaigns during residencies.

Simulation results were presented for the entire docking manoeuvre, using waypoint guidance, a discrete PID controller, vision-based global localization and a kinematics-based Kalman filter for the rendezvous stage, and a glideslope guidance algorithm with an output feedback controller using camera/ARtag pairs for the docking stage. The newly implemented camera/ARtag system performed well, with robustness to occlusion and lighting variation, and a more than sufficient level of accuracy for docking when paired with the Kalman filter. Experiments were carried out using the output feedback controller and ARtag system for regulation in front of a wall, and docking to a fixed target. Initial regulation experiments led to an investigation into the effects of a center of mass offset, which concluded that the weight distribution on the chaser Tryphon should provide a negative y-axis offset, i.e., opposing the side with cameras, for improved stability in roll and z-axis control. The first set of docking experiments demonstrated the ability of the developed GNC system to successfully bring the chaser's docking mechanism ends in contact with the fixed target's corresponding ends, and the second more extensive set demonstrated the effectiveness of the GNC system, with a success rate of over 75 %. The

optimal pre-dock distance was found to be under 0.5 m. Failure of the relay device to successfully turn on the electro-magnet was the leading cause for docking failure during the first set of docking experiments, and the size of the metallic plates were not large enough. The metallic plates of the receiver ends were replaced with larger ones for the second set of experiments, which led to an increased success rate for the completion of the docking manoeuvre.

Several recommendations for the next phase of this work include improving the reliability of the electro-magnet relay. Furthermore, this research demonstrated the docking scenario with a fixed target, and lays the groundwork to perform docking experiments with a self-regulating target Tryphon: docking to such a target is a far more difficult and challenging task. Finally, the experiments involved in this thesis include the docking stage only, with only simulation results presented for the complete assembly manoeuvre. Performing experiments involving the rendezvous and docking stages in sequence is a necessary final step in order to include this amazing manoeuvre in future Tryphon artistic performances.

References

[1] P.-Y. Brèches, "Dynamics Modeling and State Feedback Control of a Lighter-than-air Cubic Blimp," Master's thesis, McGill University, Montreal,Quebec,Canada, Aug. 2015.

[2] P.-Y. Brèches, "Dynamics modeling and state feedback control of a lighter-than-air cubic blimp," McGill University- Masters Seminar, 2015.

[3] ROS.org, "ar_track_alvar-package summary."

[4] D. St-Onge, "Analyse de la structure du mascarillon," *End of studies project report, Ecole Polytechnique de Montréal, Montreal, CA, May*, 2004.

[5] N. Reeves, E. Poncet, J. Nembrini, and A. Martinoli, "[voiles| sails], self-assembling intelligent lighter-than-air structures," in *Proc. of the Eight International Conference on Generative Art*, no. SWIS-CONF-2006-013, pp. 297–311, 2005.

[6] D. St-Onge and N. Reeves, "Human interaction with flying cubic automata," in *Proceedings of 2010 IEEE/ACM Internations Conference on Human Robots Interaction*, 2010.

[7] D. St-Onge, N. Reeves, P. Giguère, I. Sharf, G. Dudek, I. Rekleitis, P.-Y. Brèches, P. Abouzakhm, and P. Babin, "Aerostabiles: A new approach to hri researches," in *Proceedings of the Tenth Annual ACM/IEEE International Conference on Human-Robot Interaction Extended Abstracts*, pp. 277–277, ACM, 2015.

[8] D. St-Onge, C. Gosselin, and N. Reeves, "Dynamic modelling and control of a cubic flying blimp using external motion capture," *Proceedings of the Institution of Mechanical Engineers, Part I: Journal of Systems and Control Engineering*, vol. 229, pp. 970–982, Nov. 2015.

[9] I. Sharf, B. Laumonier, M. Persson, and J. Robert, "Control of a fully-actuated airship for satellite emulation," in *Robotics and Automation, 2008. ICRA 2008. IEEE International Conference on*, pp. 2218–2219, IEEE, 2008.

[10] S. Nolet, E. Kong, and D. W. Miller, "Autonomous docking algorithm development and experimentation using the SPHERES testbed," vol. 5419, pp. 1–15, 2004.

[11] D. Miller, A. Saenz-Otero, J. Wertz, A. Chen, G. Berkowski, C. Brodel, S. Carlson, D. Carpenter, S. Chen, S. Cheng, *et al.*, "Spheres: a testbed for long duration satellite formation flying in micro-gravity conditions," in *Proceedings of the AAS/AIAA Space Flight Mechanics Meeting, Clearwater, FL, Paper No. AAS 00-110*, 2000.

[12] C. Tournes, Y. Shtessel, and D. Forem, "Automatic Space Rendezvous and Docking using Second Order Sliding Mode Control," in *Sliding Mode Control* (A. Bartoszewicz, ed.), pp. 307–330, InTech, Apr. 2011.

[13] P. Singla, K. Subbarao, and J. L. Junkins, "Adaptive Output Feedback Control for Spacecraft Rendezvous and Docking Under Measurement Uncertainty," *Journal of Guidance, Control, and Dynamics*, vol. 29, no. 4, pp. 892–902, 2006.

[14] P. Jantapremjit and P. Wilson, "Guidance-control based path following for homing and docking using an autonomous underwater vehicle," in *OCEANS 2008-MTS/IEEE Kobe Techno-Ocean*, pp. 1–6, IEEE, 2008.

[15] P.-M. Lee, B.-H. Jeon, and C.-M. Lee, "A docking and control system for an autonomous underwater vehicle," vol. 3, pp. 1609–1614, Oct. 2002.

[16] J.-Y. Park, B.-H. Jun, P.-M. Lee, F.-Y. Lee, and J.-h. Oh, "Experiment on underwater docking of an autonomous underwater vehicleisimi'using optical terminal guidance," in *OCEANS 2007-Europe*, pp. 1–6, IEEE, 2007.

[17] J.-Y. Park, B.-h. Jun, P.-m. Lee, and J. Oh, "Experiments on vision guided docking of an autonomous underwater vehicle using one camera," *Ocean Engineering*, vol. 36, pp. 48–61, Jan. 2009.

[18] A. Negre, C. Pradalier, and M. Dunbabin, "Robust vision-based underwater homing using self-similar landmarks," *Journal of Field Robotics*, vol. 25, no. 6-7, pp. 360–377, 2008.

[19] K. Teo, B. Goh, and O. K. Chai, "Fuzzy docking guidance using augmented navigation system on an auv," *Oceanic Engineering, IEEE Journal of*, vol. 40, no. 2, pp. 349–361, 2015.

[20] M. Dunbabin, B. Lang, and B. Wood, "Vision-based docking using an autonomous surface vehicle," in *Robotics and Automation, 2008. ICRA 2008. IEEE International Conference on*, pp. 26–32, IEEE, 2008.

[21] S. Wu, L. Zhang, W. Xu, T. Zhou, and D. Luo, "Docking control of autonomous aerial refueling for UAV based on LQR," in *2013 10th IEEE International Conference on Control and Automation (ICCA)*, pp. 1819–1823, June 2013.

[22] D. B. Wilson, A. H. GÃűktogan, and S. Sukkarieh, "Guidance and Navigation for UAV Airborne Docking," in *Robotics: Science and Systems*, 2015.

[23] S. van der Zwaan, A. Bernardino, and J. Santos-Victor, "Vision based station keeping and docking for an aerial blimp," in *Intelligent Robots and Systems, 2000.(IROS 2000). Proceedings. 2000 IEEE/RSJ International Conference on*, vol. 1, pp. 614–619, IEEE, 2000.

[24] M. Fiala, "Comparing ARTag and ARToolkit Plus fiducial marker systems," in *IEEE International Workshop on Haptic Audio Visual Environments and their Applications, 2005*, pp. 148–153, Oct. 2005.

[25] D. Tsai, "Autonomous Vision-Based Docking of the Tethered Axel Rover for Planetary Exploration," Master's thesis, LuleÃě University of Technology, Aug. 2012.

[26] M. Fiala, "ARTag Fiducial Marker System Applied to Vision Based Spacecraft Docking. Shaw Conference Centre, Edmonton, Alberta, Canada," pp. 35–40, Aug. 2005.

[27] T. Yamada, T. Yairi, S. H. Bener, and K. Machida, "A study on slam for indoor blimp with visual markers," in *ICCAS-SICE, 2009*, pp. 647–652, IEEE, 2009.

[28] D. St-Onge, C. Gosselin, and N. Reeves, "Dynamic modelling of a cubic flying robot," in *ASME 2010 International Design Engineering Technical Conferences and Computers and Information in Engineering Conference*, pp. 1157–1165, American Society of Mechanical Engineers, 2010.

[29] V. L. Syrmos, C. T. Abdallah, P. Dorato, and K. Grigoriadis, "Static output feedbackâĂŤA survey," *Automatica*, vol. 33, pp. 125–137, Feb. 1997.

[30] P. C. Hughes, *Spacecraft attitude dynamics*. Courier Corporation, 2012.

[31] http://gazebosim.org/, "Gazebo."

[32] ogre3d.org, "Ogre-open source 3d graphics engine," 1999.

[33] S. Güney and A. Atasoy, "An approach to pole placement method with output feedback," in *UKACC Control Conference,as accurate January 29th*, 2011.

[34] A. Harmat, M. Trentini, and I. Sharf, "Multi-camera tracking and mapping for unmanned aerial vehicles in unstructured environments," *Journal of Intelligent & Robotic Systems*, vol. 78, no. 2, pp. 291–317, 2015.

[35] A. Harmat, I. Sharf, and M. Trentini, "Parallel tracking and mapping with multiple cameras on an unmanned aerial vehicle," in *Intelligent robotics and applications*, pp. 421–432, Springer, 2012.

[36] G. F. Franklin, J. D. Powell, and M. L. Workman, *Digital control of dynamic systems*, vol. 3. Addison-wesley Menlo Park, 1998.

[37] H. B. Hablani, M. L. Tapper, and D. J. Dana-Bashian, "Guidance and Relative Navigation for Autonomous Rendezvous in a Circular Orbit," *Journal of Guidance, Control, and Dynamics*, vol. 25, no. 3, pp. 553–562, 2002.

APPENDIX A
Gain Matrix, Closed-loop Poles and Controller's Final Form for Docking Experiments

Output feedback controller gain matrix for first set of experiments:

$$\mathbf{K} = 0.17 \begin{bmatrix} -4.86 & -0.91 & 0.00 & -4.86 & 0.91 & 0.00 & 0.00 & 0.00 & 0.81 & -12.67 & 10.34 & -0.00 & -12.66 & -10.34 & 0.00 & \mathbf{0}_{1\times3} \\ 0.00 & -1.54 & 0.17 & 0.00 & -1.54 & 0.16 & -0.26 & 0.01 & 0.00 & 0.00 & -8.26 & 0.57 & 0.00 & -8.26 & 0.53 & \mathbf{0}_{1\times3} \\ 0.00 & 0.17 & -7.89 & 0.00 & 0.17 & -7.88 & -2.02 & -0.01 & 0.00 & 0.00 & 0.58 & -11.31 & 0.00 & 0.58 & -11.36 & \mathbf{0}_{1\times3} \\ 0.00 & 0.00 & -0.14 & 0.00 & 0.00 & -0.15 & -13.62 & 0.00 & 0.00 & 0.00 & -0.01 & -0.48 & 0.00 & -0.01 & -0.50 & \mathbf{0}_{1\times3} \\ 0.00 & -0.01 & -5.91 & 0.00 & 0.00 & 5.91 & 0.02 & -5.25 & 0.00 & 0.00 & -0.02 & 2.51 & 0.00 & -0.02 & -2.53 & \mathbf{0}_{1\times3} \\ -0.07 & -0.11 & 0.00 & -0.07 & 0.11 & 0.00 & 0.00 & 0.00 & 0.54 & -0.24 & -3.23 & 0.00 & -0.24 & 1.23 & 0.00 & \mathbf{0}_{1\times3} \end{bmatrix} \tag{A.1}$$

Corresponding closed-loop poles:

$$- \begin{pmatrix} 0.088 \pm 0.252i \\ 0.029 \pm 0.084i \\ 0.007 \pm 1.046i \\ 0.031 \pm 1.016i \\ 0.061 \pm 0.138i \\ 0.083 \pm 0.331i \end{pmatrix} \tag{A.2}$$

Closed-loop form of output feedback controller with x,y,z integral terms:

$$\begin{bmatrix} \dot{\mathbf{x}}_\delta \\ \dot{\boldsymbol{\xi}} \end{bmatrix} = \begin{bmatrix} \mathbf{A}_0 - \mathbf{B}_0\mathbf{K}\hat{\mathbf{C}}_0 & \mathbf{B}_0\mathbf{k}_1 \\ -\hat{\mathbf{C}}_0 & \mathbf{0}_{18\times18} \end{bmatrix} \begin{bmatrix} \mathbf{x}_\delta \\ \boldsymbol{\xi} \end{bmatrix} + \begin{bmatrix} \mathbf{0}_{18\times1} \\ \mathbf{I}_{18\times1} \end{bmatrix} \mathbf{r}(t) \tag{A.3}$$

$$\mathbf{u}_\delta = -\mathbf{K}\mathbf{y}_\delta + \mathbf{k}_1\boldsymbol{\xi} \tag{A.4}$$

$$\dot{\boldsymbol{\xi}} = \mathbf{r}(t) - \mathbf{y}_\delta \tag{A.5}$$

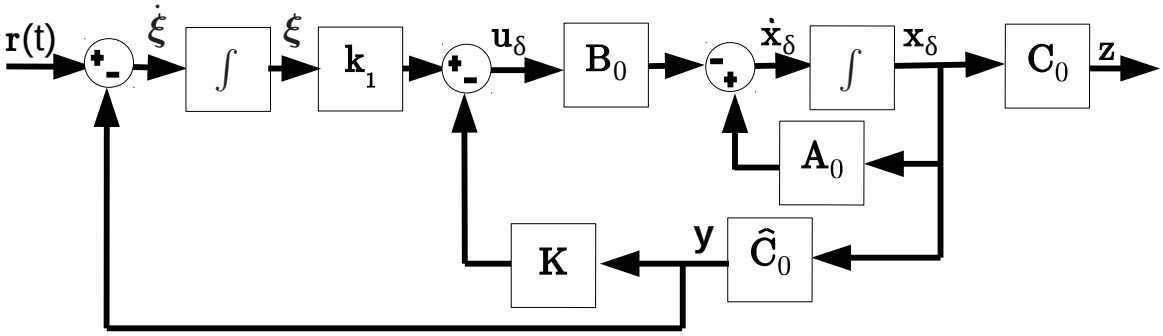

Figure A–1: Block diagram of final closed-loop system

where

$$\mathbf{k}_1 = \begin{bmatrix} \mathbf{k}_A & \mathbf{0}_{3\times12} \\ \mathbf{0}_{3\times6} & \mathbf{0}_{3\times12} \end{bmatrix}, \quad \mathbf{k}_A = \begin{bmatrix} 0.5\xi_x & 0 & 0 & 0.5\xi_x & 0 & 0 \\ 0 & 0.5\xi_y & 0 & 0 & 0.5\xi_y & 0 \\ 0 & 0 & 0.5\xi_z & 0 & 0 & 0.5\xi_z \end{bmatrix} \tag{A.6}$$

and ξ_x, ξ_y, ξ_z are the integral gains and are all set to -0.02.

Corresponding closed-loop poles:

$$-\begin{pmatrix} 0.0^{15} \\ 0.013 \\ 0.045 \\ 0.008 \\ 0.082 \pm 0.250i \\ 0.028 \pm 0.083i \\ 0.007 \pm 1.046i \\ 0.031 \pm 1.016i \\ 0.080 \pm 0.330i \\ 0.038 \pm 0.133 \end{pmatrix} \tag{A.7}$$

where $(\ )^{15}$ represents a multiplicity of 15.

Output feedback controller gain matrix for second set of experiments:

$$\mathbf{K} = 0.15 \begin{bmatrix} -8.86 & -0.41 & 0.00 & -8.86 & 0.41 & 0.00 & 0.00 & 0.00 & 0.81 & -14.67 & 5.34 & -0.00 & -15.66 & -5.34 & 0.00 & \mathbf{0}_{1\times3} \\ 0.00 & -2.54 & 0.17 & 0.00 & -2.54 & 0.16 & -0.26 & 0.01 & 0.00 & 0.00 & -4.86 & 0.57 & 0.00 & -4.86 & 0.53 & \mathbf{0}_{1\times3} \\ 0.00 & 0.17 & -13.09 & 0.00 & 0.17 & -13.09 & -2.02 & -0.01 & 0.00 & 0.00 & 0.58 & -13.31 & 0.00 & 0.58 & -13.31 & \mathbf{0}_{1\times3} \\ 0.00 & 0.00 & -0.14 & 0.00 & 0.00 & -0.15 & -13.62 & 0.00 & 0.00 & 0.00 & -0.01 & -0.48 & 0.00 & -0.01 & -0.50 & \mathbf{0}_{1\times3} \\ 0.00 & -0.01 & -5.91 & 0.00 & 0.00 & 5.91 & 0.02 & -5.25 & 0.00 & 0.00 & -0.02 & 2.51 & 0.00 & -0.02 & -2.53 & \mathbf{0}_{1\times3} \\ -0.07 & -0.17 & 0.00 & -0.07 & 0.11 & 0.00 & 0.00 & 0.00 & 3.76 & -0.84 & -4.83 & 0.00 & -0.84 & 4.83 & 0.00 & \mathbf{0}_{1\times3} \end{bmatrix} \tag{A.8}$$

and with ξ_x, ξ_y, ξ_z set to -0.02, -0.02, and -0.04 respectively.

Corresponding closed-loop poles:

$$-\begin{pmatrix} 0.0^{15} \\ 0.010 \\ 0.0027 \\ 0.008 \\ 0.027 \pm 1.028i \\ 0.006 \pm 1.054i \\ 0.083 \pm 0.331i \\ 0.054 \pm 0.185i \\ 0.081 \pm 0.403i \\ 0.018 \pm 0.178 \end{pmatrix} \tag{A.9}$$

where $(\ )^{15}$ represents a multiplicity of 15.